Metamaterial Based Superdirectivity

Lianbo Li

Wadham College

University of Oxford

A thesis submitted for the degree of

Doctor of Philosophy

Hilary 2017

Abstract

A model-supporting, simple, compact, robust and high efficiency two-element parasitic superdirective array comprising electrically small resonant metamaterial elements, namely singly split resonator rings (SSRRs), is predicted by an analytical model and is verified by CST simulation results. The analytical model is built by combining a method of calculating a two-SSRR array's far field radiated energy density and a well working equivalent circuit for a two-SSRR parasitic array. This model is capable of easily but accurately predicting the far field radiation behaviours of an electrically small parasitic array of two SSRRs (the two SSRRs are not necessarily standard and identical), based on certain information of the array, namely the SSRRs' dimensions, the SSRRs' electrical components (L, C and R), the SSRRs' rotating orientation angles (α_1 and α_2), the two SSRRs's separation (d) and the array's operation frequency. The importance of this analytical model in designing parasitic superdirective arrays is discussed. Simulation results show that the model predicted two-SSRR parasitic superdirective structure (the 'CC' structure) can achieve an end-fire directivity of 4.36, with an elements' separation $d = 4mm$ working at $1.914GHz$, and can maintain an efficiency as high as 98.6%. After a short discussion of the design principle behind the 'CC' structure, improved superdirective structures of are identified and studied based on simulation results. Among these structures, the 'CCLr' structure can achieve the largest directivity value of 5.06 (very close to 5.25, the theoretical limit value of a two-dipole array) with a moderate efficiency of 81.4%. A comparison between these two-SSRR parasitic superdirective structures (the 'CC' and its improved versions) and two commercial two-element Yagi antennas show that these two-SSRR structures achieve better directive performances than the commercial two-element Yagi antennas do. Through performing the study of near field energy flow for magnetic dipole based structures (analytical results) and SSRR based structures (simulation results), with the help of the concept of causal surfaces, the physical reason behind the superdirectivity phenomenon is revealed.

I would like to dedicate this thesis to my dearest parents,

and girlfriend.

Acknowledgements

First, I would like to express my sincere gratitude and appreciation to my supervisors Prof. Eketarina Shamonina and Prof. Chris Stevens for their inspiration, vision, guidance and encouragement during my study.

I am very grateful to Dr. Andrea Vallecchi and Dr. Yue Li for their creative advice, helpful comments and encouragement during my project.

Thanks to my collaborators, Dr. Krystallo Hadjicosti, Dr. Anna Radkovskaya, Prof. Laszlo Solymar, and Prof. David Edwards, for the interesting discussions and sharing ideas in the last few years.

I am also grateful to all previous and current members of the Oxford communication group and the Imperial OSD group for their indispensable support and valuable friendships.

Last but not least, I would like to thank my parents for their spiritual support and encouragement. I am deeply grateful to my girlfriend for her love, understanding and patience over the past two years.

Publications

[1] A. Radkovskaya, L. Li, E. Edwards, D. Edwards, E. Shamonina, and L. Solymar, "Near-field Superdirectivity for Coupled Dimers of Meta-Atoms," *Proc. Metamaterials' 2014*, pp. 271-273, August 2014.

[2] L. Li, E. Shamonina, C. J. Stevens, L. Solymar, "'Poynting Vector Optics' for Superdirective Dimers," *The* 9^{th} *International Congress on Andvanced Electromagnetic Materials in Microwaves and Optics-Metamaterials 2015*, September 2015.

[3] A. Radkovskaya, A. Vallecchi, L. Li, G. Faulkner, C. J. Stevens, and E. Shamonina, "Experimental demonstration of superdirectivity for coupled dimers of meta-atoms," In *Advanced Electromagnetic Materials in Microwaves and Optics (METAMATERIALS), 2016* 10^{th} *International Congress on*, pp. 328-330. IEEE, 2016.

[4] A. Vallecchi, L. Li, C. J. Stevens, E. Shamonina, "Mapping Directivity of Coupled Dimers of Meta-Atoms," submitted to *The* 11^{th} *International Congress on Andvanced Electromagnetic Materials in Microwaves and Optics-Metamaterials 2017*

Contents

List of Figures

List of Tables

Chapter 1

Introduction

This chapter provides an overview of the project I have accomplished during my DPhil study. First, the motivation of performing the research is discussed. Then a summary of the project is presented. In the end, the structure of this thesis is interpreted.

1.1 Motivation

Due to the importance of sensor array signal processing in many diverse application areas, such as sonar, radar, audio engineering and wireless communications, superdirectivity, as a useful tool which can provide a significant potential for sensor arrays to enhance their performance in terms of angular resolution, bearing estimation accuracy, noise suppression ability and reduction of array aperture, has become more and more important [1]. However, most of the current existing superdirective designs are either not practical, due to well known limitations like low efficiency, narrow bandwidth and low tolerances, or not simple and compact enough. Therefore, designing simple, compact, robust and high efficiency superdirective structures is extremely necessary now.

Apart from the industrial demand for superdirective antennas, a deep study of the physical reasons behind the superdirectivity phenomenon is also essential. The advantages of multiple-input-multiple-output (MIMO) systems, in multipath propagation environment, over single antenna systems have been well demonstrated [2] [3]. However, the closely spaced antennas for such a multiantenna system can produce unexpected superdirectivity effects, degrading the system's performance [4]. In order to avoid these unexpected effects, performing a deep study of the physical mechanism behind superdirectivity is crucially worthwhile.

1.2 Project Summary

The objective of my research is to design a simple, compact, robust and high efficiency superdirective antenna structure and explore the physical reason behind superdirectivity. My research focuses on building an analytical model for an electrically small two-element parasitic array of metamatrial elements (which can be used to analyse the array's currents' behaviours and to identify conditions for the array to achieve superdirectivity), studying and improving the model predicted superdirective structure, and visualizing the near field energy flow around superdirective structures. The whore research can be divided into four stages:

1. Understanding existing superdirective designs

   The ideas behind the existing designs and the reasons why some of them can not practically work need to be understood. Especially the most recent advances of electrically small parasitic superdirective arrays comprising resonant elements and metamaterial-inspired superdirectivity need to be well studied.

2. Model building

   It is essential to first build an analytical model, which can identify conditions for a two-element parasitic array comprised of metamaterial elements to achieve superdirectivity. Through combining the design iedeas behind electrically small parasitic superdirective arrays comprising resonant elements and metamaterial-inspired superdirectivity, the model should be capable of predicting the far field radiation behaviours of an electrically small parasitic array of two metamaterial elements, based on certain information of the array.

3. Superdirective performances improving

   Certain modifications of the model predicted superdirective structure (the identified conditions) need to be studied for improving superdirective performances. In order to analyse the improvements, parametric study needs to be performed based on simulation results.

4. Power flow

   The physical reason why superdirectivity can happen needs to be explored through studying the near field energy flow around superdirective structures based on simulation results.

In summary, my superdirective design combines the design principles behind electrically small parasitic superdirective arrays comprising resonant elements and metamaterial-inspired superdirectivity through directly using the simplest metamaterial unit cells as unit elements of superdirective arrays. An easy-to-use analytical model is developed to support the realization of such a design. The analytical model identifies conditions for achieving superdirectivity, leading to an electrically small superdirective structure comprising memtamaterial elements. This structure is then studied and improved based on simulation results. In the end, the physical reason leading to superdirectivity is revealed.

1.3 Dissertation Organization

Chapter 2 reviews the background of superdirectivity. It contains necessary information for better understanding the concept of superdirectivity and its realization, followed by a detailed history note of superdirectivity-related theories, designs and techniques.

Chapter 3 describes electrically small two-element endfire arrays. The energy patterns and directivites for three basic uniform linear two-element arrays are calculated as a reference for following analysis of more practical structures. Analogous to the pattern multiplication rule, an energy pattern multiplication rule is introduced. Also, specifically for the maximum endfire directivity of a parasitic array of two identical magnetic dipoles a relationship between the dipole elements' Q factor and the array's coupling coefficient is described. In the end, a method of calculating the radiated energy for an endfire array of two electrically small slotted CLAs carrying non-uniform currents (NCLAs) is demonstrated.

Chapter 4, starting with the circuit analysis for the simplest metamaterial elements, Singly Split Ring Resonators (SSRRs), presents an equivalent circuit for a two-SSRR parasitic array, along with the method of calculating radiated energy, for a two-NCLA array, demonstrated in Chapter 3, forming a powerful analytical model to analyse the array's currents' behaviours and to identify conditions for the array to achieve superdirectivity. A 'CC' structure, predicted by the model, is capable of achieving endfire superdirectivity.

Chapter 5 shows the simulation results for the model predicted superdirective structure (the 'CC' structure). Improvements are made through applying modifications to this 'CC' structure. The results of parametric studies, based on simulation results, of the improved structures are presented. Based on a comparison with two commercial two-element Yagi antennas, the superiority of my structures is confirmed.

Chapter 6 visualizes the near field time-average and instantaneous energy flow for magnetic dipole based structures (analytical results) and SSRR based structures (simulation results). Through the comparison of the energy flow for all these structures, with the help of the concept of causal surfaces, the physical reason why superdirectivity can happen is revealed.

Chapter 7 summarises the thesis and presents its conclusions. Suggestions and ideas are proposed and discussed for future research.

Chapter 2

Background on Superdirectivity

This chapter begins with a description of the definition of superdirectivity. Then a detailed history of superdirectivity is presented.

2.1 Definition of Superdirectivity

In order to better understand superdirectivity, it is necessary to first clearly introduce the very basic concept, directivity of an antenna. According to the 2013 version of the *IEEE Standard Definitions of Terms for Antennas* [5], it is defined as "the ratio of the radiation intensity in a given direction from the antenna to the radiation intensity averaged over all directions. The average radiation intensity is equal to the total power radiated by the antenna divided by 4π. If the direction is not specified, the direction of maximum radiation intensity is implied." It can expressed as the following formula (Equation 2.1).

$$D(\theta, \varphi) = \frac{P(\theta, \varphi)}{P_{tot}/4\pi} \tag{2.1}$$

where θ and φ are the longitudinal and latitudinal angles respecting a standard spherical coordinate system. Some antenna researchers may prefer to use gain, in stead of directivity, as the figure of merit to measure the directional performance of an antenna [6] [7] [8]. According to the *IEEE Standard Definitions of Terms for Antennas* [5], the gain of an antenna in fact equals to the product of the antenna's directivity and radiation efficiency. This raises a fact, which should be always kept in mind, that an antenna with a large directivity does not necessarily have a high gain. In this thesis, the radiation efficiency is also studied for superdirective structures. The radiation efficiency in this thesis is defined as the ratio of an antenna's radiation resistance to the total resistance of the antenna structure.

The definition of superdirectivity provided by the IEEE [5] is "the condition that occurs when the antenna directivity is significantly higher than that with the array or aperture uniformly excited." For example, for an endfire array of two identical magnetic dipoles with the two dipole elements uniformly excited, the maximum endfire directivity is around 2.66. Therefore in this thesis, an endfire directivity above 4 for an array of two electrically small elements [9] (for example an array of two intermediate (or small) loop elements [10]) is regarded as superdirectivity. The IEEE definition implies that both the size and the directivity of an antenna need to be considered for judging whether the antenna is superdirective or not. Some single element antennas do not produce very large directivity values but still can be treated as superdirective elements due to their reduced sizes. For example, antennas like small loops or short wires can easily maintain a directivity value around 1.5 as their sizes decrease within a certain range [11] [12]. Even though these single element antennas can be superdirective, they are of no interest for this research. Because they are omnidirectional antennas while unidirectional superdirective antennas are more attractive. Usually the unidirectional superdirectivity can be realized by forming a multi-element array [13] [10]. However accomplishing an array superdirectivity through adding more elements within a fixed length can inflict other problems, namely low efficiency, sensitive excitation and low position tolerances [13]. This research focuses on designing electrically small two-element parasitic superdrective arrays comprising metamaterial elements, which can potentially avoid some of the intrinsic problems of classic superdirective structures.

2.2 History of Superdirectivity

2.2.1 Early Stage

Many antenna researchers [14] [15] [16] [17] believe that the idea of superdirectivity first came from *Oseen*. In 1922 [18], *Oseen* discussed the possibility of forming an arbitrarily narrow beam, which could lead to superdirectivity [19]. With a monotonic phase function for an endfire array, *Hansen* and *Woodyard* [20] theoretically achieved limited superdirectivity. *Franz* also published a paper in 1939 [21] and discussed the gain and the absorption surfaces of large directive arrays. Based on a rigorous mathematical analysis, *Schelkunoff* [22] pointed out that theoretically superdirectivity can be obtained from a linear endfire array, with equal spacing of the array polynomial zeros over that portion of the unit circle represented by the array [23]. Superdirectivity became widely popular when *Bouwkamp* and *De Bruijn* [24] pointed out an error made by *La Paz* and *Miller* [25] and concluded that theoretically no limit in the directivity of a linear array exists [26]. The well known important theorem that a fixed aperture size can achieve any desired directivity value had been rediscovered several times while the practical limitations mysteriously existed for superdirective antennas' design [27] [13]. After World War II, in 1946 *Reid* [28] further studied the Hansen-Woodyard endfire superdirectivity and gave the maximum gain for a given length of array and the corresponding value of phase velocity. In the same year, *Uzkov* [29] showed that the endfire directivity of an array of n isotropic radiators can increase up to n^2 when the separation d between any two nearest neighbour elements approaches 0 [30] [31]. Also in 1946, *Dolph* [32] solved the problem of a high sidelobe level for *Schelkunoff*'s method of realizing superdirectivity through inventing the widely used Dolph-Chebyshev array: using the equal-level oscillations of a Chebyshev polynomial, the array can produce an array pattern with the optimum sidelobe level [33] [34]. Then following the development, *Riblet* [35] showed that any desired directivity can be yielded by a Delph-Chebyshev array with element spacing less than $\lambda/2$ [36] [37]. In the computation of Dolph-Chebyshev coefficients and directivity, complementary advances were developed by *DuHamel* [38] [39] and *Stegen* [40] [41]. After the electrically small antennas were defined and studied by *Wheeler* [42] [43], *Chu* [44] immediately developed a limit on Q factor for electrically small antennas and derived the directivity from a consideration of spherical modes. Subsequently *Harrington* [45] extended *Chu*'s theory and finally accomplished the so called Chu-Harringtong limit [46].

2.2.2 Designs versus Limitations

Based on the theories established and experiences obtained by early researchers, a great number of superdirective designs, which were expected to overcome one or more limitations in superdirectivity, had been reported since 1960s.

In 1966, *Lo*, *Lee* and *Lee* [47] proposed a unified formulation for optimizing the signal-to-noise ratio of any arbitrary array and showed, among other conclusions, that in the case of an endfire array the phase of optimum excitation defers only slightly from the antiphase excitation if the element spacing is not larger than $\lambda/2$. In 1973, it was shown by *Lin et al.* [48] that for an array of two loaded short antennas through adjusting the elements' impedance loadings, the current distributions in the elements could be appropriately modified to significantly improve the array's directivity. In 1977, *Walker et al.* concluded that the inefficiency of electrically small superdirective arrays could be overcome through setting the array's small elements in superconducting state. Believing in that designs for optimum directive gain were hardly practical, *Newman*'s design idea very much emphasized the adoption of constraints: in 1978 [49], he described electrically small arrays designed for maximum directive gain subject to a constraint on the sensitivity factor; Then in 1982 [50], he detailedly presented a procedure for designing a wideband electrically small superdirective array with two computer codes useful in the design and analysis of superdirective arrays. *Newman*'s more practical design still left one problem unsolved: when the arrays size decreased, the complexity of the feed network would significantly increase. In 1978, *Dawoud* [37] showed that superdirective arrays with overall lengths of a few wavelengths could be inherently realisable while maintained high radiation efficiency through generating polynomials. For the same research he also took the mutual coupling between different elements into consideration. Later in 1993 [51], he studied the scanning properties of his superdirective antenna arrays. In 1986, *Cox* [52] performed constraint optimum beamforming for several types of background noise and showed that the near optimum performance can be achieved using a simple delay and beamformer. *Veremey* is probably the first researcher who started designing superdirective antennas using passive resonant elements: In 1991 [53], he first described and explained his design idea; Then in 1995 [54] and 1998 [55], he further investigated the properties of his design and showed that the desired phase and amplitude distributions of an aperture or an array to achieve superdirectivity can be generated and controlled through adjusting the mutual coupling between these passive resonant elements. Many later superdirectivity designs and studies had been inspired by *Veremey*'s research work. One apparent example is *Bokhari*'s superdirective antenna array of printed parasitic elements [56]. Before 2000, several other designs related to superdirectivity were also proposed, for example, *Cheng*'s optimization design for Yagi-Uda arrays [57], *Itoh*'s two-element superdirective array of high-T_c superconducting small helical radiators [58] and *Tager*'s new technique (Near Field Superdirectivity) [59].

During this period, another two important papers, which summarized the development status of superdirectivity, were published. The first one was published in 1981 by *Hansen* [46]. In this paper, even though *Hansen* discussed the limitations in electrically small antennas and superdirective antennas separately, due to the increased popularity of the utilization of electrically small elements for superdirective designs, the article provided a fairly good summary of the problems, waiting to be solved by the following superdirectivity researchers. Another one was published in 1995 by *Haviland* [60]. This paper analysed the problems of the existing superdirective designs and highlighted possible routes to practically realize superdirectivity.

2.2.3 New Development

Since 2000, a great number of designs and studies of superdirectivity have been noticed [61] [62] [63] [64] [65] [66] [67]. Here only the important advances of electrically small parasitic superdirective arrays comprising resonant elements, and metamaterial-inspired superdirectivity are reviewed. In this thesis a structure can be regarded as an electrically small structure when it meets the condition where $kr_{rad} < 1$ [9]. Here k is the free space wave number and r_{rad} is the radius of the radian sphere [42].

Yaghjian's group has probably played the most important role in realizing practical electrically small superdirective arrays comprised of resonant elements. They first started with two-element arrays of monopoles, with both of the two elements excited separately, and theoretically and computationally achieved superdirectivity [68] [69]. Due to the significantly reduced radiation efficiency and the substantial impedance mismatch when decreasing the element's spacing, they soon moved to parasitic two-element superdirective arrays of electrically small resonant low Q elements [70] [71] and through frequency optimization they computationally achieved superdirectivity while maintained good bandwidth performance. Another useful point they revealed is that use of the parasitic element as a reflector at an appropriate frequency has yielded a closer match to the optimal phase difference (of the two elements) than when the parasitic element was used as a director at an appropriate frequency. In 2008, they experimentally realized an electrically small parasitic two-element superdirective array using the previously introduced resonant low Q elements, achieving a gain as high as $7dB$ (linear 5.01) [9]. Because their arrays comprise a combination of significant electric and magnetic dipoles and quadrupoles, the corresponding maximum theoretically possible linear directivity should be 8 rather than 5.25 (for an two-element array of dipoles).

Apart from *Yaghjian*'s group, *Ziolkowski*'s group [72] realized supersbackcattering antenna arrays, using electrically small resonant EHDs, in 2015.

Since the experimental demonstration of functioning electromagnetic metamaterials were suggested and reported [73] [74], plenty of research attention has been paid to adopting metamaterial unit cells to improve different performance characteristics of antenna systems. [75] is probably the first article which has discussed the effect of metamaterials on an antenna's directive behaviour. In 2007, two pioneering papers were published, which directed the realization of metamaterial-inspired superdirectivity into two completely different routes. *Buell et al.* [76], in his paper, showed that through applying embedded-circuit metamaterial as insulator to suppress the mutual coupling between the elements of a five-element patch array, superdirectivity could be numerically and experimentally achieved with improved bandwidth performance. In stead of using metamaterials as insulator, *Alù* and *Engheta* [77] directly employed metamaterial resonator subwavelength antennas as the elements of an electrically small nano antenna structure, which could theoretically and numerically provide superdirectivity while also might overcome the standard limitations of the feeding system present in classic superdirective structures. In 2009, *Yaghjian* [78] also proposed theoretical possibilities of incorporating metamaterials into his electrically small two-element parasitic supergain antenna to further increase its gain. In 2012, *Kokkinos et al.* [79] presented a compact electrically small endfire superdirective array, operating in the 2.45GHz band, comprising microstrip-fed low profile folded monopoles, designed using metamaterial-inspired phase shifting lines. *Kokkinos*'s array indeed provided very large directivity but also showed fairly low radiation efficiency. In the same year, *Ludwig et al.* [80] showed that a three-slot metascreen initially for near field subwavelength focusing could also operate as a superdirective antenna in the far field at a different but close by frequency. Even though the metascreen is not much different from an three-element array of metamaterial loops, its lack of fabrication flexibility and the dissipation in the screen can possibly limit the structure's potential popularity. In 2013, *Shamonina* and *Solymar* [17] raised the possibility of achieving superdirectivity in metamaterials by relying on magnetoinductive waves [81] and they also analytically identified, for a dimer of magnetically coupled split rings, conditions for achieving superdirectivity in terms of dimer size, the coupling strength and the quality factor. Later in 2014 [82], they further extended their studies to trimers of split rings coupled both magnetically and electrically and again analytically identified conditions for superdirectivity. In 2013 [83], another design of metamaterial-inspired electrically small superdirective arrays was reported and the article showed the parasitic array achieved a measured directivity of 4.8dB (linear 3.02) but with a very low radiation efficiency. Based on [83], later in 2014, *Haskou et al.* [84] described an ultra-compact design of two- and three-element superdirective linear arrays. The two- and three-element arrays, with a unit dimension of $\lambda/14 \times \lambda/17$ and a inter-element spacing of 0.064λ, respectively achieved maximum directivities of 6.3dB (linear 4.27) and 9dB (linear 7.94) according to simulation results. Then based on [83] and [84], *Haskou et al.* [85], by adopting *Yaghjian*'s method [69] of calculating the excitation coefficients to maximize the directivity in a given direction, presented a design approach for parasitic superdirective arrays and further concluded that the concept of parasitic superdirective arrays was a compromise between the directivity, the efficiency and the antenna size. In 2014, *Dakhli et al.* [86] proposed a metamaterial-inspired superdirective structure by placing a split ring resonator in the vicinity of a monopole antenna while placing both of them on a relatively large substrate ground plane and successfully showed very high directivity. In the same year, *Gupta* and *Saxena* [87], following *Buell*'s design route [76], suggested a new method to improve the directive gain, leading to superdirectivity, of patch antenna arrays for ISM band $2.4GHz$ by using split ring resonator metamaterial as a notch filter between the array elements to suppress the mutual coupling between the elements, which allowed for denser packing and enhanced directivity.

Following the most recent development, this research has successfully combined the design principles behind both electrically small parasitic superdirective arrays comprising resonant elements and metamaterial-inspired superdirectivity by directly using the simplest metamaterial unit cells as elements of a new model-supporting, simple, compact, robust and high efficiency two-element parasitic superdirective array presented later in this thesis. In order to reveal all the details, next chapter will first start with studies of electrically small two-element endfire arrays.

Chapter 3

Electrically Small Two-Element Endfire Antenna Arrays

This chapter begins with a brief explanation of pattern multiplication rule, which provides an effective analytical method of describing the radiation pattern of a uniform two-element array antenna. Next, using the pattern multiplication rule, the radiation patterns and the directivities of an endfire array of two isotropic radiators, an endfire array of two magnetic dipoles and an endfire array of two electrically small circular loop antennas (CLAs) are calculated as a reference for latter superdirective analysis. Also, analogous to the pattern multiplication rule, an energy pattern multiplication rule is introduced. Then, specifically for the maximum endfire directivity of a parasitic array of two identical magnetic dipoles a relationship between the dipole elements' Q factor and the array's coupling coefficient is described. At the end of this chapter, an endfire array consisting two more practical elements, electrically small slotted CLAs carrying non-uniform currents (NCLAs), is studied and a method of calculating the array's radiated energy is demonstrated, with only the excitation coefficients (maximum currents) left unknown. These maximum currents are yet to be determined in next Chapter.

The main new contributions in this Chapter include: 1. The relationship between the element's Q factor and the array's coupling coefficient for the maximum endfire directivity of a parasitic array of two identical magnetic dipoles; 2. A new method of calculating the far field radiation pattern for an array consisting of two elements with non-uniform current distribution.

3.1 Pattern Multiplication Rule

The pattern multiplication rule states that in far field the radiated field of a uniform array of identical elements is equal to the product of the field of a single element, at a selected reference point (usually the origin), and the array factor of that array. For a two-element uniform array of identical elements, the array factor is usually expressed in the form of Equation 3.1 [10].

$$(AF)_2 = \cos\left[\frac{1}{2}(kd_{eff}\sin\theta\cos\varphi + \beta)\right] \tag{3.1}$$

where k is the free space wave number corresponding to the operational frequency, d_{eff} is the effective distance between the two elements (usually centre to centre), θ and φ are the longitudinal and attitudinal angles for a standard spherical coordinate system, and β is the phase difference of the currents carried by the two elements.

3.2 Energy Patterns and Directivity

For an array of two identical isotropic radiators, fully excited by currents with a same magnitude, shown in Figure 3.1, using the pattern multiplication rule and far field approximations, the array's normalized far field average radiated energy density can be expressed as Equation 3.2 [10] [88] [89] [90] [91] [92] [93].

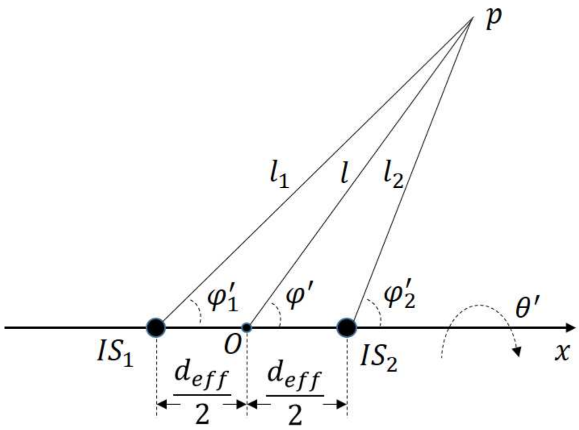

Figure 3.1: The sketch of an array of two isotropic radiators.

$$P_{an_{iso}}(\varphi') = \left\{ \cos\left[\frac{1}{2}(kd_{eff}\cos\varphi' + \beta)\right]\right\}^2 \tag{3.2}$$

where k is the wave number: $k = 2\pi/\lambda$, λ is the free space wavelength, d_{eff} is the effective separation distance between the two isotropic elements, and β is the phase difference of the two elements' currents.

With a relatively small enough separation distance of $d_{eff} = 0.2\lambda$, the far field radiation energy patterns for different phase differences are presented in Figure 3.2.

According to these patterns, through choosing a suitable phase difference β (here 0.86π) subject to a specific small enough separation distance d_{eff} (here 0.2λ), very large directivity can be achieved in endfire direction for such an array in far field. The achievable maximum directivity of this array for different separation distances and the phase difference corresponding to the maximum directivity are plotted and shown in Figure 3.3. Based on this figure, the theoretical limit directivity value of 4 [94] [29] [69] for this two-element isotropic array can be reached, with an extremely small separation distance plus a near π phase difference.

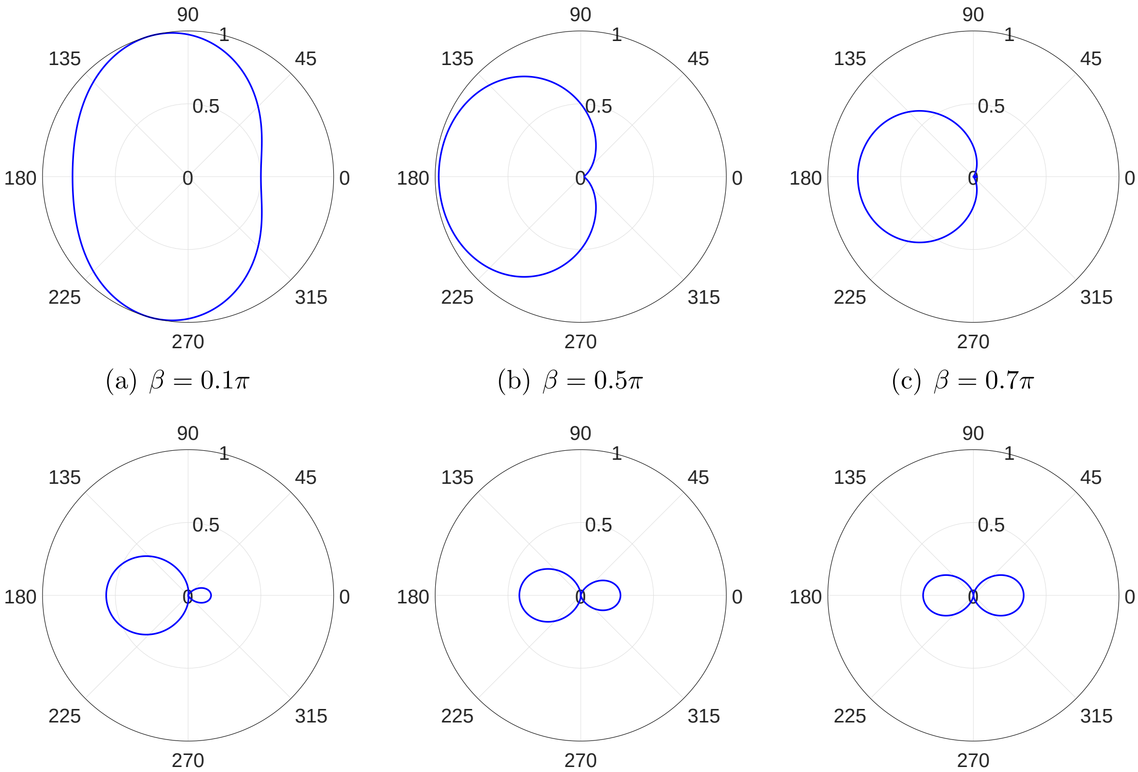

(a) $\beta = 0.1\pi$ (b) $\beta = 0.5\pi$ (c) $\beta = 0.7\pi$

(d) $\beta = 0.86\pi$ (e) $\beta = 0.95\pi$ (f) $\beta = \pi$

Figure 3.2: The far field radiation energy patterns for different phase differences. To produce these patterns, a constant magnitude of the currents carried by the array's elements, a constant observation distance and a constant operation frequency are assumed.

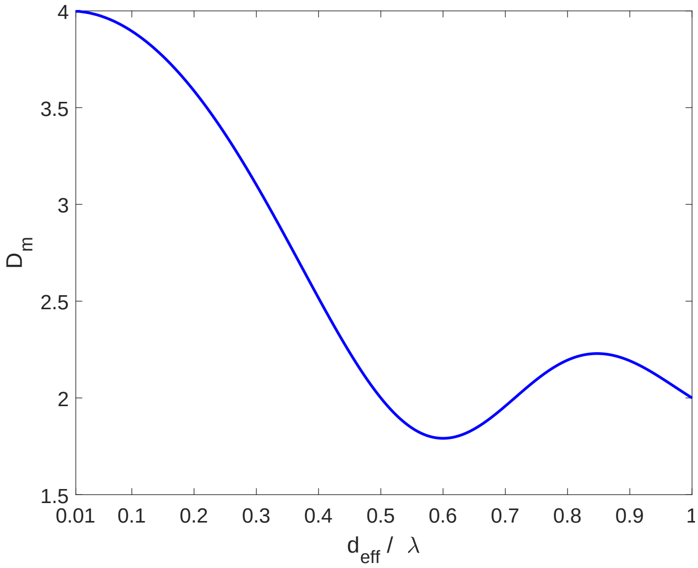

(a) The maximum directivity D_m

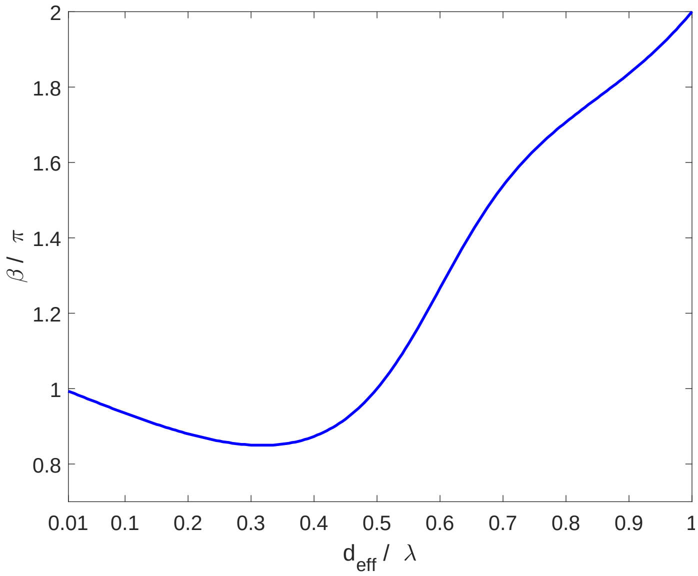

(b) The phase difference β corresponding to D_m

Figure 3.3: (a) The maximum far field directivity D_m (in $\varphi' = \pi$ direction) and (b) the phase difference β corresponding to the maximum directivity D_m.

For an array of two identical magnetic dipoles, fully excited by currents with a same magnitude, shown in Figure 3.4, the array's normalized far field average radiated energy density can be expressed as Equation 3.3 [10].

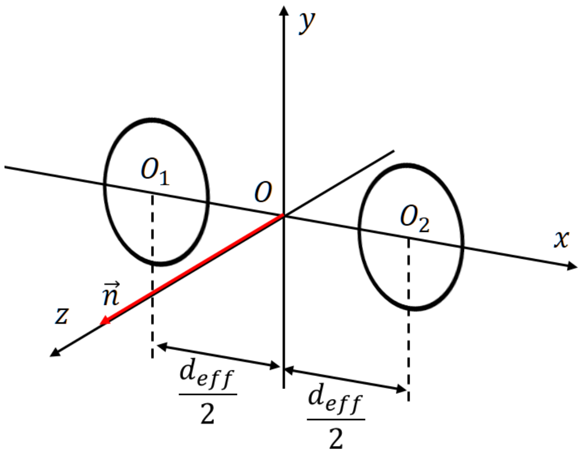

(a)

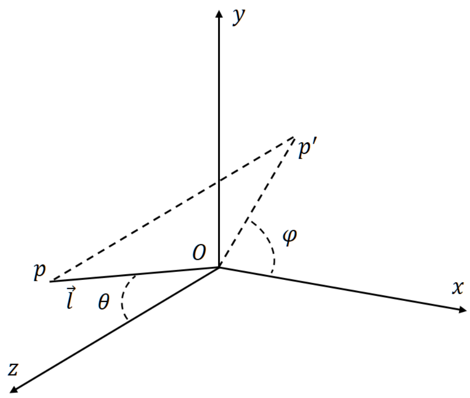

(b)

Figure 3.4: (a) One array of two identical magnetic dipoles and (b) its coordinate system for far field analysis: O_1 and O_2 are the two dipoles' centres, d_{eff} is the distance between O_1 and O_2.

$$P_{an_{dip}}(\theta, \varphi) = \sin^2\theta \cos^2\left[\frac{1}{2}(kd_{eff}\sin\theta\cos\varphi + \beta)\right] \tag{3.3}$$

where the effective separation distance is set to be $d_{eff} = 0.2\lambda$. This array's 3D far field radiation energy patterns for different phase differences are presented in Figure 3.5. Similar with the case for an array of two identical isotropic radiators, when the phase difference is set to be a proper value (here 0.86π), a very large endfire directivity value can be reached in far field. The maximum directivity of this array for different separation distances and the phase difference corresponding to the maximum directivity, along with those for the array of two identical isotropic radiators (Figure 3.3), are plotted and displayed in Figure 3.6. According to these figures, the theoretical limit directivity values of both an endfire array of two identical isotropic radiators (4) and an endfire array of two identical magnetic dipoles (5.25), with an appropriate near π phase difference β (here 0.86π) chosen subject to a near zero separation distance (here 0.2λ), can be achieved.

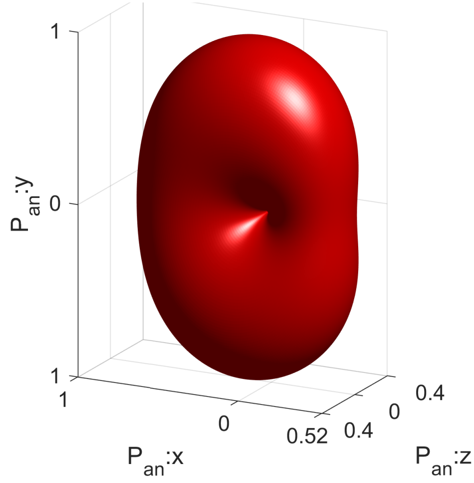

(a) $\beta = 0.1\pi$

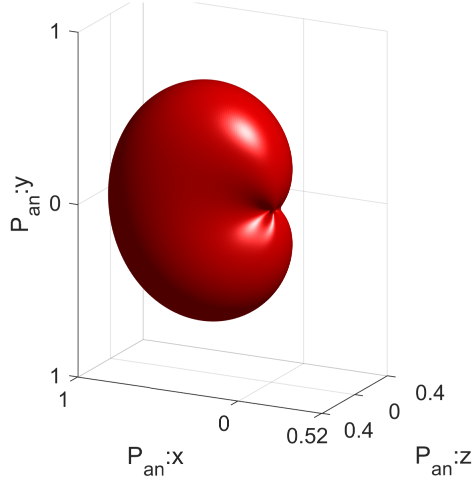

(b) $\beta = 0.5\pi$

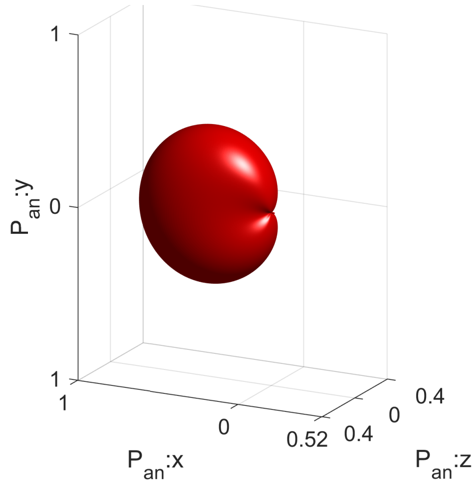

(c) $\beta = 0.7\pi$

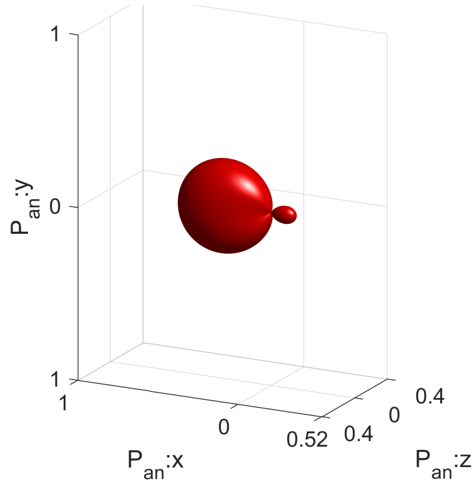

(d) $\beta = 0.86\pi$

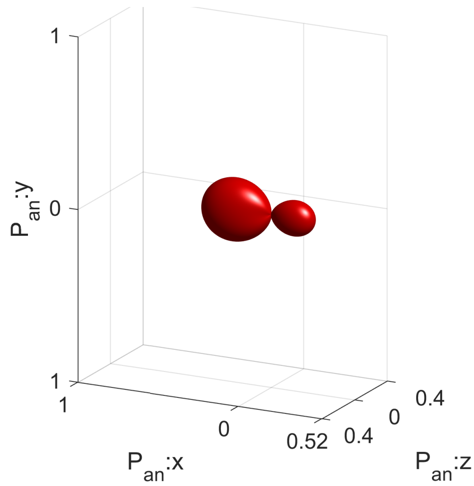

(e) $\beta = 0.95\pi$

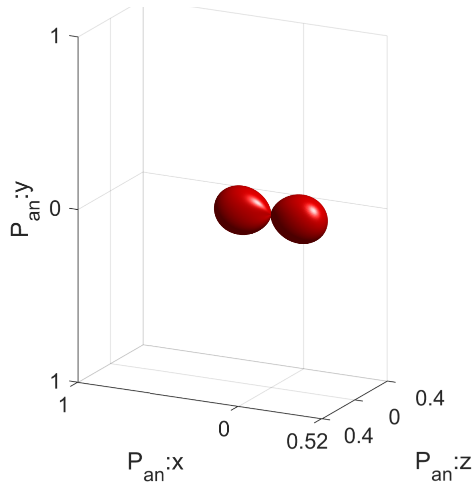

(f) $\beta = \pi$

Figure 3.5: The 3D far field radiation energy patterns for different phase difference β: the axis x, y, z respectively indicate the normalized energy density along x, y and z direction; the energy P_{an} is normalized to the maximum value of ($P_{an_{dip}}$, $\beta = 0.1\pi$).

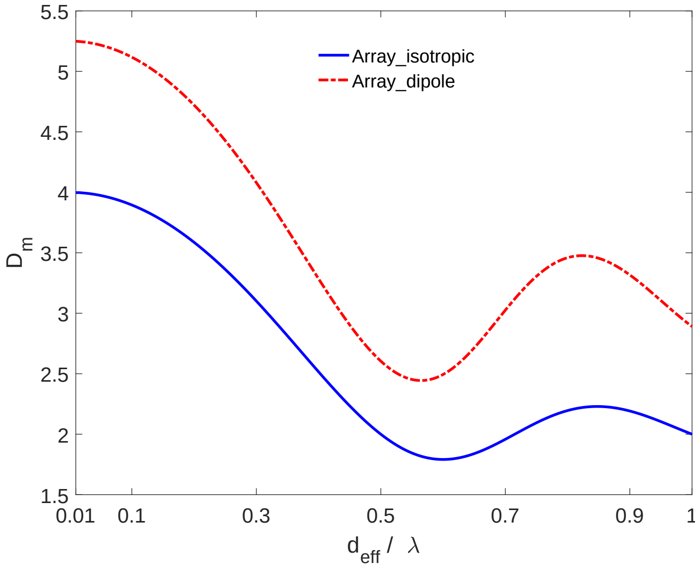

(a) The maximum directivity D_m

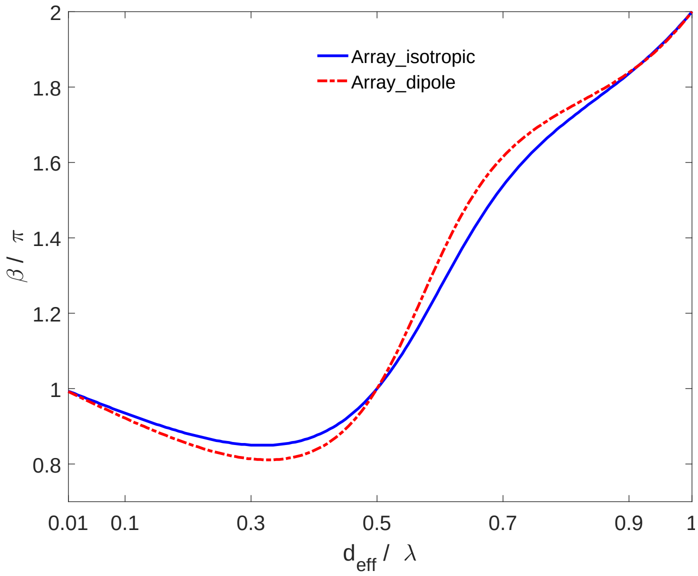

(b) The phase difference β corresponding to D_m

Figure 3.6: (a) The maximum far field directivity D_m and (b) the phase difference β corresponding to the maximum directivity D_m.

Similarly, for an array of two identical circular loop antennas (CLAs), also fully excited by currents with a same magnitude, shown in Figure 3.7, the normalized far field average radiated energy density can be expressed as Equation 3.4 [10] [89] [90] [91] [92] [93]. Here, the array's elements are set to be intermediate CLAs with a uniform current distribution [10] [95] [42]. One particular point worth emphasizing is that all the intermediate elements (CLAs, NCLAs and SSRRs) (according to the *Wheeler*'s strict criterion of an electrically small antenna and the classification method adopted in [10]) mentioned in this thesis are also belonging to the category of electrically small antennas considering the criterion used by *Yaghjian* in [9].

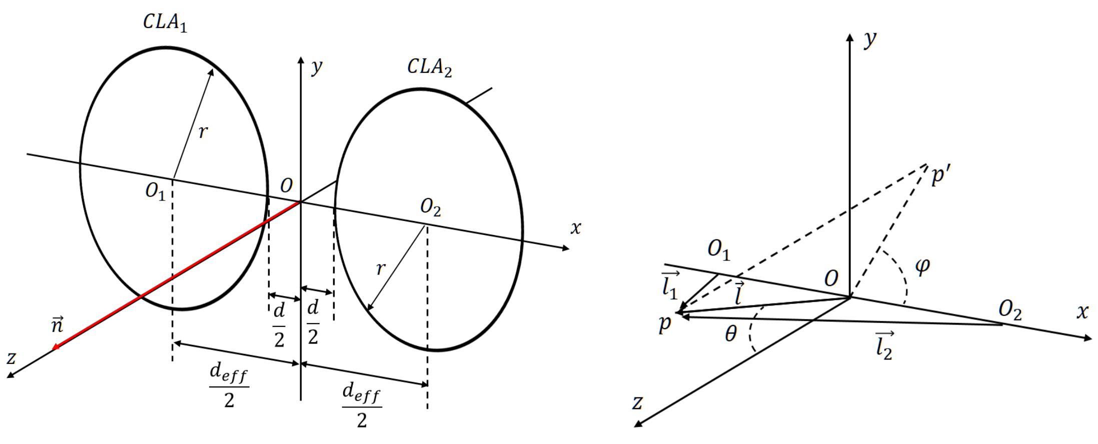

Figure 3.7: (a) One array of two identical circular loop antennas and (b) its coordinate system for far field analysis: O_1 and O_2 are the two CLAs' centres, d_{eff} is the distance between O_1 and O_2, $d = d_{eff} - 2r$.

$$P_{an_{CLA}}(\theta, \varphi) = J_1^2(kr\sin\theta)\cos^2\left[\frac{1}{2}(kd_{eff}\sin\theta\cos\varphi + \beta)\right] \tag{3.4}$$

where $J_1^2(kr\sin\theta)$ is the Bessel function of the first kind of the order 1, k is the wave number for an operation frequency of $1.9GHz$[1], and $r = 10.6mm$ is the radius of the CLAs.

[1]A frequency slightly lower than the resonance frequency of a SSRR; The details of a SSRR is demonstrated in Chapter 4.

For the effective separation distance $d_{eff} = 0.2\lambda$, the 3D far field radiation energy patterns are shown in Figure 3.8 for different phase differences β. With a properly chosen β (here 0.86π), very large far field directivity can be achieved in the endfire direction. For this β, the 2D far field energy patterns are also produced and displayed in Figure 3.9.

The maximum achievable far field directivity for different d_{eff} values and the phase difference corresponding to the maximum directivity, along with those for an array of two identical isotropic radiators and those for an array of two identical magnetic dipoles (Figure 3.6), are plotted and shown in Figure 3.10. These figures can provide a good reference for latter superdirectivity analysis in this project, especially the figures for the array of two CLAs, considering that these CLA elements have the same sizes and electrical sizes as our actual metamaterial elements (SSRRs)[2] do. Even though the array of two CLAs shows almost exactly the same far field radiation behaviours as the array of two identical magnetic dipoles does (Figure 3.5, Figure 3.8 and Figure 3.10), due to the CLA elements' finite sizes ($2r = 21.2mm$, indicated by the dashed black line in Figure 3.10), the practical largest directivity obtained by such a two-CLA array can only be lower than 5. In fact, the largest directivity of any two-element array comprising circular loop elements with the same or similar electrical sizes ($2r = 21.2mm$ corresponding to a operation frequency around $1.9GHz$) can only be lower than 5, for example a two-NCLA array (Section 3.5) and a two-SSRR array (Chapter 4). Any approach towards the theoretical limit value (5.25) of a two-dipole array [69] from 5 requires further modifications of such a two identical loop elements' structure. In this thesis, a maximum directivity larger than 4 achieved by any structures possessing a similar electrical size with the two-CLA array is regarded as superdirectivity.

[2]The details of a SSRR is demonstrated in Chapter 4.

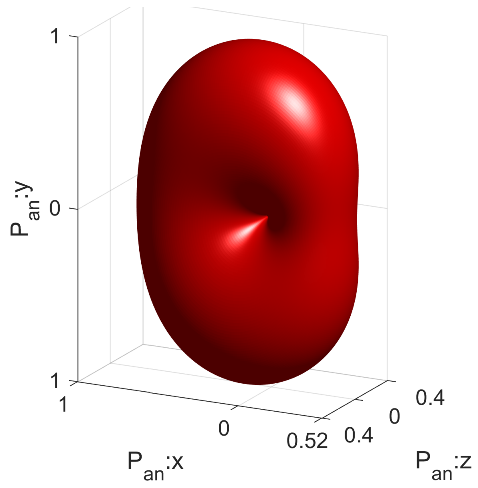

(a) $\beta = 0.1\pi$

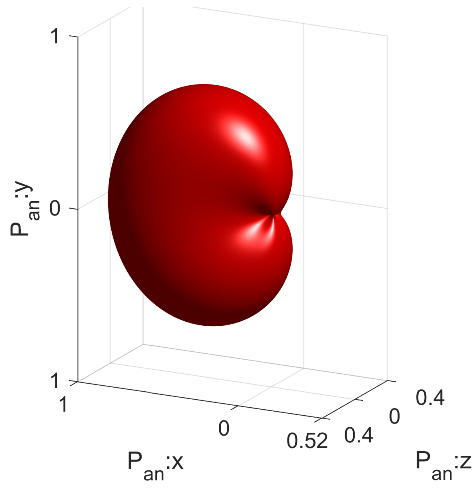

(b) $\beta = 0.5\pi$

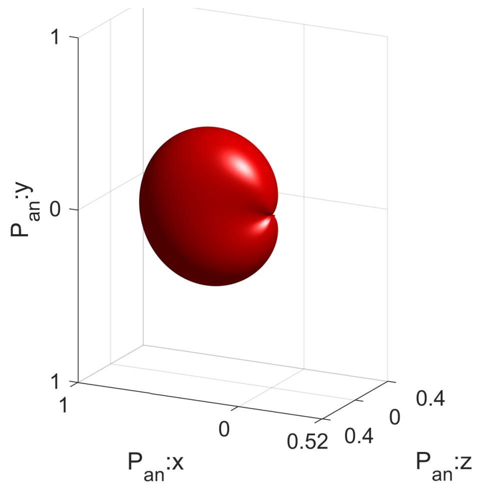

(c) $\beta = 0.7\pi$

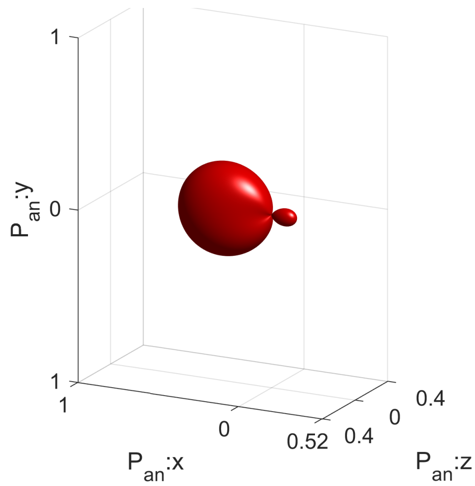

(d) $\beta = 0.86\pi$

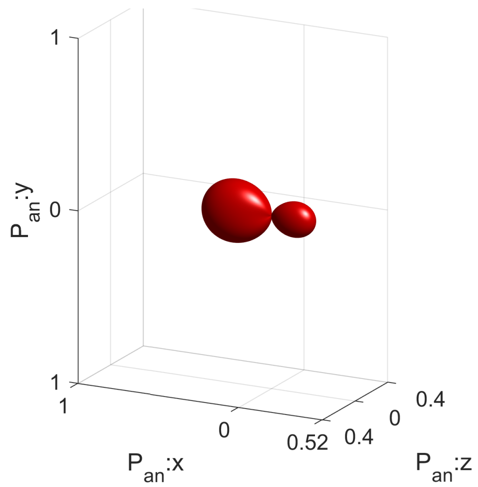

(e) $\beta = 0.95\pi$

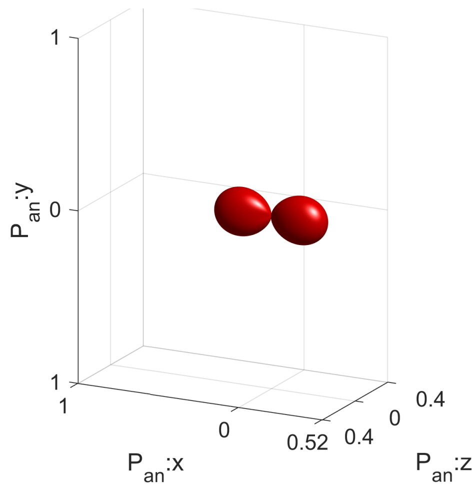

(f) $\beta = \pi$

Figure 3.8: The 3D far field radiation energy patterns for different phase difference β: the axis x, y, z respectively indicate the normalized energy density along x, y and z direction; the energy P_{an} is normalized to the maximum value of ($P_{an_{CLA}}$, $\beta = 0.1\pi$).

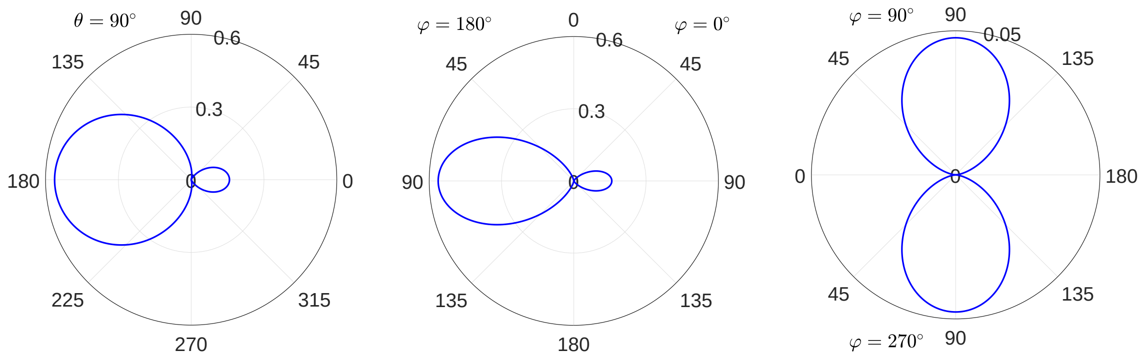

(a) xy plane energy pattern (b) xz plane energy pattern (c) yz plane energy pattern

Figure 3.9: The 2D far field energy patterns for the two-CLA array with a separation distance $d_{eff} = 0.2\lambda$ and a phase difference $\beta = 0.86\pi$; the energy P_{an} is normalized to the maximum value of $(P_{an_{CLA}}, \beta = 0.1\pi)$.

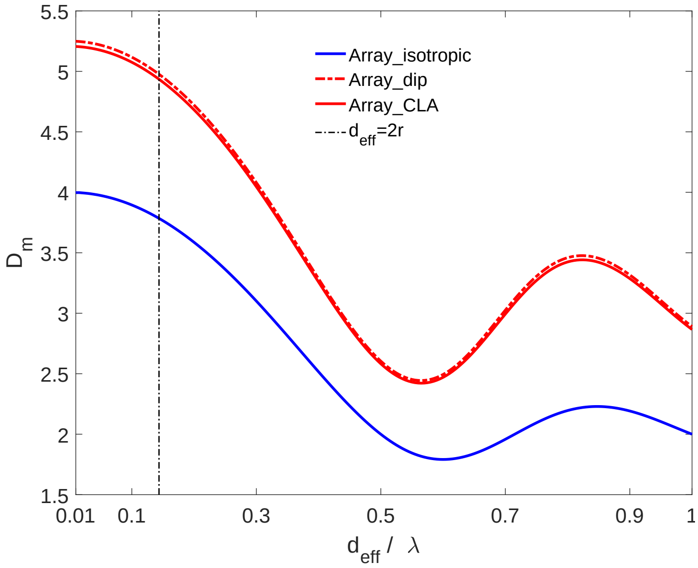

(a) The maximum directivity D_m

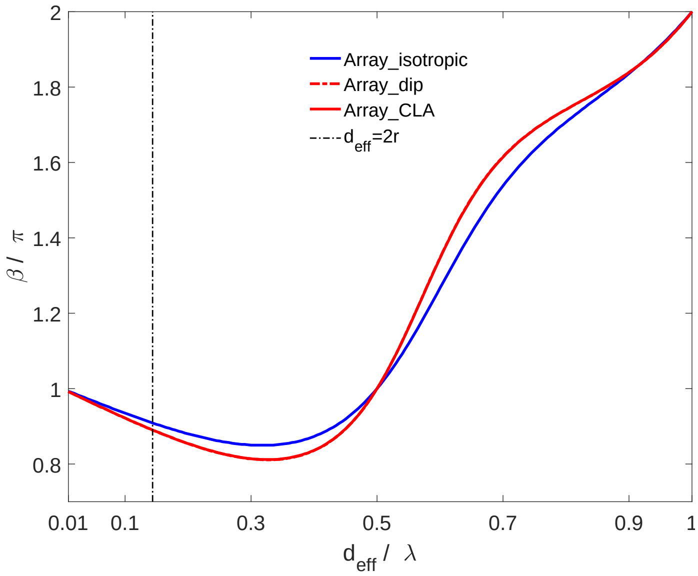

(b) The phase difference β corresponding to D_m

Figure 3.10: (a) The maximum far field directivity D_m (in $\varphi' = \pi$ direction) and (b) the phase difference β corresponding to the maximum directivity D_m.

Another noticeable phenomenon shown in Figure 3.2, Figure 3.5 and Figure 3.8 is that as β increases towards π, the total radiated energy level reduced. This reduction due to increased Q factor for high directivity antennas is inevitable as [5] suggests.

3.3 Energy Pattern Multiplication Rule

By now in this chapter a same magnitude of the currents carried by an array's two elements has been assumed. However, if the elements's currents do not have a common magnitude, then the pattern multiplication rule cannot simply apply even though the phase difference still remains as β.

For an array of two isotropic radiators shown in Figure 3.1, with currents $|I_1| \neq |I_2|$, the total electric field at a far field point p can be expressed as Equation 3.5 [88] [93], with the help of the far field approximations:

$$\begin{aligned} E_{t_{iso}}(l, \varphi', \theta') =& C_{iso}\left(\frac{I_1 e^{-ikl_1}}{l_1} + \frac{I_2 e^{-ikl_2}}{l_2}\right) \\ =& \frac{C_{iso}\,|I_1|\,e^{-ikl}}{l}\left(e^{-i\frac{1}{2}(kd_{eff}\cos\varphi'+\beta)} + \left|\frac{I_2}{I_1}\right| e^{i\frac{1}{2}(kd_{eff}\cos\varphi'+\beta)}\right) \\ =& \frac{C_{iso}\,|I_1|\,e^{-ikl}}{l}\left\{(\left|\frac{I_2}{I_1}\right| + 1)\left[\cos\frac{1}{2}(kd_{eff}\cos\varphi' + \beta)\right]\right. \\ & \left. + i(\left|\frac{I_2}{I_1}\right| - 1)\left[\sin\frac{1}{2}(kd_{eff}\cos\varphi' + \beta)\right]\right\} \end{aligned} \tag{3.5}$$

where C_{iso} is a constant. Then the average radiated energy density in far field can be calculated as [10]:

$$\begin{aligned} P_{a_{iso}}(l, \varphi', \theta') &= \frac{C_{iso}^2\,|I_1|^2}{2Z_0 l^2}\left[\left|\frac{I_2}{I_1}\right|^2 + 1 + 2\left|\frac{I_2}{I_1}\right|\cos(kd_{eff}\cos\varphi' + \beta)\right] \\ &= \frac{\left|E_{1_{iso}(l,\varphi',\theta')}\right|^2}{2Z_0}\left[\left|\frac{I_2}{I_1}\right|^2 + 1 + 2\left|\frac{I_2}{I_1}\right|\cos(kd_{eff}\cos\varphi' + \beta)\right] \\ &= P_{1_{iso}}(l, \varphi', \theta')\left[\left|\frac{I_2}{I_1}\right|^2 + 1 + 2\left|\frac{I_2}{I_1}\right|\cos(kd_{eff}\cos\varphi' + \beta)\right] \end{aligned} \tag{3.6}$$

where Z_0 is the free space impedance.

Similarly, for the array of two CLAs shown in Figure 3.7, with $|I_1| \neq |I_2|$, the array's electric field at a far field point p can be calculated through a vectorial summation [10]:

$$\begin{aligned} E_{a_{CLA}}(l,\theta,\varphi) &= E_1 + E_2 \\ &= Z_0 \frac{rk}{2} J_1(kr\sin\theta) \left(\frac{|I_1|\, e^{-i\frac{\beta}{2}} e^{-ikl_1}}{l_1} + \frac{|I_2|\, e^{i\frac{\beta}{2}} e^{-ikl_2}}{l_2} \right) \end{aligned} \tag{3.7}$$

Here the far field approximations are as following:

$$\varphi_1 \simeq \varphi_2 \simeq \varphi \tag{3.8a}$$

$$\left.\begin{aligned} l_1 &\simeq l + \frac{d_{eff}}{2} \sin\theta\cos\varphi \\ l_2 &\simeq l - \frac{d_{eff}}{2} \sin\theta\cos\varphi \end{aligned}\right\} \text{for phase variations} \tag{3.8b}$$

$$l_1 \simeq l_2 \simeq l \quad \text{for amplitude variations} \tag{3.8c}$$

where l_1 and l_2 are respectively the distances from the far field observation point p to O_1 and to O_2, φ_1 and φ_2 are the angles between the x axis and the objections of l_1 and l_2 on xy plane. Thus the array's far field electric field can be newly expressed as:

$$\begin{aligned} E_{a_{CLA}}(l,\theta,\varphi) =& Z_0 \frac{rk\,|I_1|\, e^{-ikl}}{2l} J_1(kr\sin\theta) \\ & \times \left\{ (\left|\frac{I_2}{I_1}\right| + 1) \left[\cos\frac{1}{2}(kd_{eff}\sin\theta\cos\varphi + \beta)\right] \right. \\ & \quad \left. + i(\left|\frac{I_2}{I_1}\right| - 1) \left[\sin\frac{1}{2}(kd_{eff}\sin\theta\cos\varphi + \beta)\right] \right\} \end{aligned} \tag{3.9}$$

Then the array's far field average radiated energy density will be [10]:

$$\begin{aligned}
P_{a_{CLA}}(l,\theta,\varphi) &= \frac{Z_0 r^2 k^2 |I_1|^2}{8l^2} J_1^2(kr\sin\theta) \\
&\quad \times \left[\left|\frac{I_2}{I_1}\right|^2 + 1 + 2\left|\frac{I_2}{I_1}\right| \cos(kd_{eff}\sin\theta\cos\varphi+\beta) \right] \\
&= \frac{1}{2}\frac{|E_{1_{CLA}}(l,\theta,\varphi)|^2}{Z_0} \\
&\quad \times \left[\left|\frac{I_2}{I_1}\right|^2 + 1 + 2\left|\frac{I_2}{I_1}\right| \cos(kd_{eff}\sin\theta\cos\varphi+\beta) \right] \\
&= P_{1_{CLA}}(l,\theta,\varphi) \left[\left|\frac{I_2}{I_1}\right|^2 + 1 + 2\left|\frac{I_2}{I_1}\right| \cos(kd_{eff}\sin\theta\cos\varphi+\beta) \right]
\end{aligned} \tag{3.10}$$

Comparing Equation 3.10 with Equation 3.6, there is only one difference existing inside the square brackets on the right hand side: at the position of $\sin\theta\cos\varphi$ for Equation 3.10, it is $\cos\varphi'$ for Equation 3.6. However if the array of two isotropic antennas shown in Figure 3.1 is put into a 3D coordinate system shown in Figure 3.7, the term $\cos\varphi'$ will be equivalently converted to $\sin\theta\cos\varphi$. Therefore, even though these two equations are for different arrays, they show a common appearance. Based on these two equations, an energy pattern multiplication rule can be introduced analogous to the field pattern multiplication rule: for a two-element array of two identical elements, the far field radiated energy density equals to the product of the first element's radiated energy density, at a specific reference point, and the energy array factor. The energy array factor is:

$$AF_p = \left[\left|\frac{I_2}{I_1}\right|^2 + 1 + 2\left|\frac{I_2}{I_1}\right| \cos(kd_{eff}\sin\theta\cos\varphi+\beta) \right] \tag{3.11}$$

Although the energy pattern multiplication rule and the energy array factor are extracted only based on the array in Figure 3.1 and the array in Figure 3.7, their validity remains for any other arrays of two identical elements whether the elements are uniformly excited or not.

3.4 $Q|\kappa| = \gamma\lambda/d_{eff}$: Parasitic Endfire Arrays of Two Magnetic Dipoles

For an arbitrary parasitic endfire array of two identical magnetic dipoles (shown in Figure 3.4), with the help of the energy pattern multiplication rule introduced in last section, the far field radiated energy density can be calculated through Equation 3.12. Here a parasitic array means that only the array's first element (left) is driven by a source, with the second element being excited only through inductive coupling.

$$P_{a_{dip}}(l,\theta,\varphi) = P_{1_{dip}}(l,\theta,\varphi)\left[\left|\frac{I_2}{I_1}\right|^2 + 1 + 2\left|\frac{I_2}{I_1}\right|\cos(kd_{eff}\sin\theta\cos\varphi + \beta)\right] \tag{3.12}$$

where $P_{1_{dip}}(l,\theta,\varphi)$ is the far field radiated energy density of the first magnetic dipole, I_1 and I_2 are respectively the currents carried by the first and the second elements, $\beta = \angle(I_2/I_1)$ is the phase difference of these two currents, k is the wave number, and d_{eff} is the effective separation distance between the two dipole elements. Considering the far field expression of $P_{1_{dip}}(l,\theta,\varphi)$, the array's normalized far field average radiated energy density can then be calculated through:

$$P_{an_{dip}}(\theta,\varphi) = \sin^2\theta\left[\left|\frac{I_2}{I_1}\right|^2 + 1 + 2\left|\frac{I_2}{I_1}\right|\cos(kd_{eff}\sin\theta\cos\varphi + \beta)\right] \tag{3.13}$$

The current ratio I_2/I_1 can be expressed as Equation 3.14, based on an equivalent circuit shown in Figure 3.11 [96] [97], assuming only magnetic coupling being present in between the two elements.

$$\frac{I_2}{I_1} = \frac{\dfrac{\kappa}{2}}{\dfrac{i}{Q} + \left(\dfrac{\omega_0}{\omega}\right)^2 - 1} \tag{3.14}$$

where a harmonic time dependence $e^{i\omega t}$ is assumed, ω is the operational angular frequency, ω_0 is the single element's resonant angular frequency, $\kappa = 2L_m/L$ is the magnetic coupling coefficient, and $Q = \omega_0 L/R$ is the single element's Q factor.

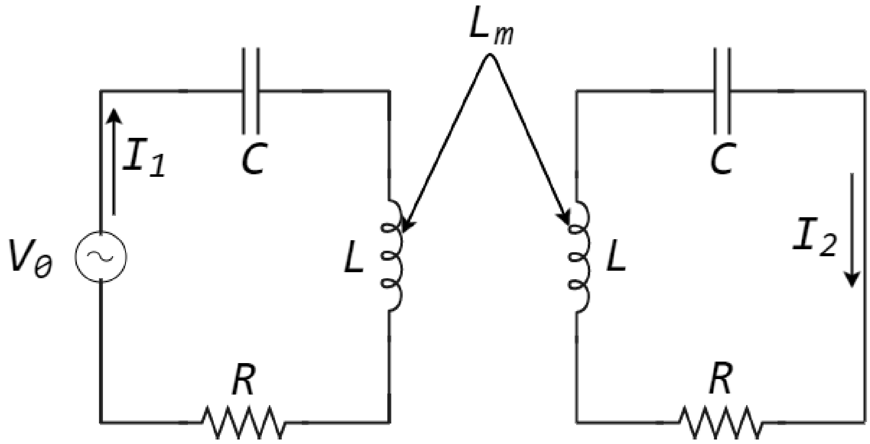

Figure 3.11: The equivalent circuit for an arbitrary parasitic endfire array of two identical magnetic dipoles; Here between the two elements, only magnetic coupling (L_m) is present.

After substituting Equation 3.14 back into Equation 3.13, it can be clearly seen that if the effective separation d_{eff} is set to be a specific fraction of the operational wavelength, the array's far field radiation pattern will be determined by three factors: the Q factor, the coupling coefficient κ and the frequency ratio ω_0/ω. The relationship between these factors is studied when the array's maximum endfire directivity is achieved for $d_{eff} = 0.01\lambda$, $d_{eff} = 0.05\lambda$ and $d_{eff} = 0.1\lambda$. With κ limited within a reasonable range ($-1 \leq \kappa \leq -0.01$) [98], and for each κ value with Q and ω_0/ω chosen for the maximum endfire directivity value, the array's maximum endfire directivity values and the chosen Q values for different κ are calculated and presented in Figure 3.12. According to the figures, as the relative separation d_{eff}/λ increases, the array's maximum achievable endfire directivity is reduced. Corresponding to the maximum endfire directivity, the optimal Q factor also decreases as the relative separation increases (Figure 3.12(b)). It can be seen from Figure 3.12(b) that in order to achieve superdirectivity at a lower κ value, a higher Q factor is required which may be difficult to realize in practice. In addition, the optimal Q factor apparently shows a same declining trend as the term $\lambda/(|\kappa|d_{eff})$ shows. By introducing a constant number γ, the following relationship can be easily obtained:

$$Q|\kappa| = \gamma\frac{\lambda}{d_{eff}} \tag{3.15}$$

where γ is a constant number around 0.75. This relationship is specifically valid when the maximum endfire directivity is achieved for an arbitrary parasitic array of two identical magnetic dipoles regarding the magnetic inductive coupling as the only coupling between the two magnetic dipole elements.

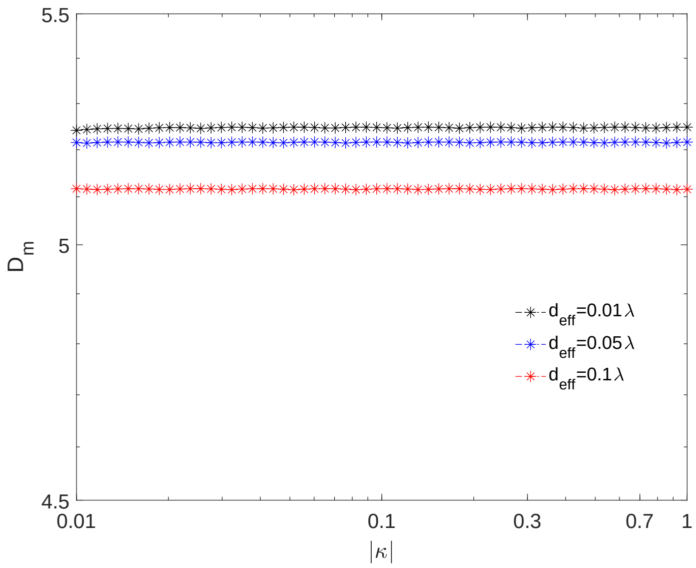

(a) The maximum directivity

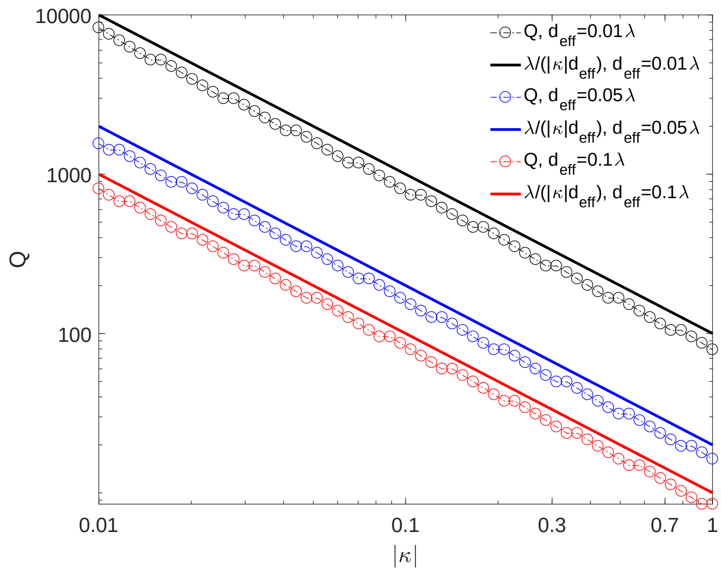

(b) The optimal Q factor

Figure 3.12: (a) The maximum far field directivity and (b) the corresponding optimal Q factor for: $d_{eff} = 0.01\lambda$, $d_{eff} = 0.05\lambda$ and $d_{eff} = 0.1\lambda$; Here the Q factor is a single magnetic dipole element's Q factor and all the curves are plotted in logarithm scale.

3.5 Non-uniform Currents

In this section, a method of calculating the radiated energy of a two-element array of electrically small slotted CLAs carrying non-uniform currents (NCLAs), is introduced. The slots are also called gaps here. Figure 3.13 shows such an array.

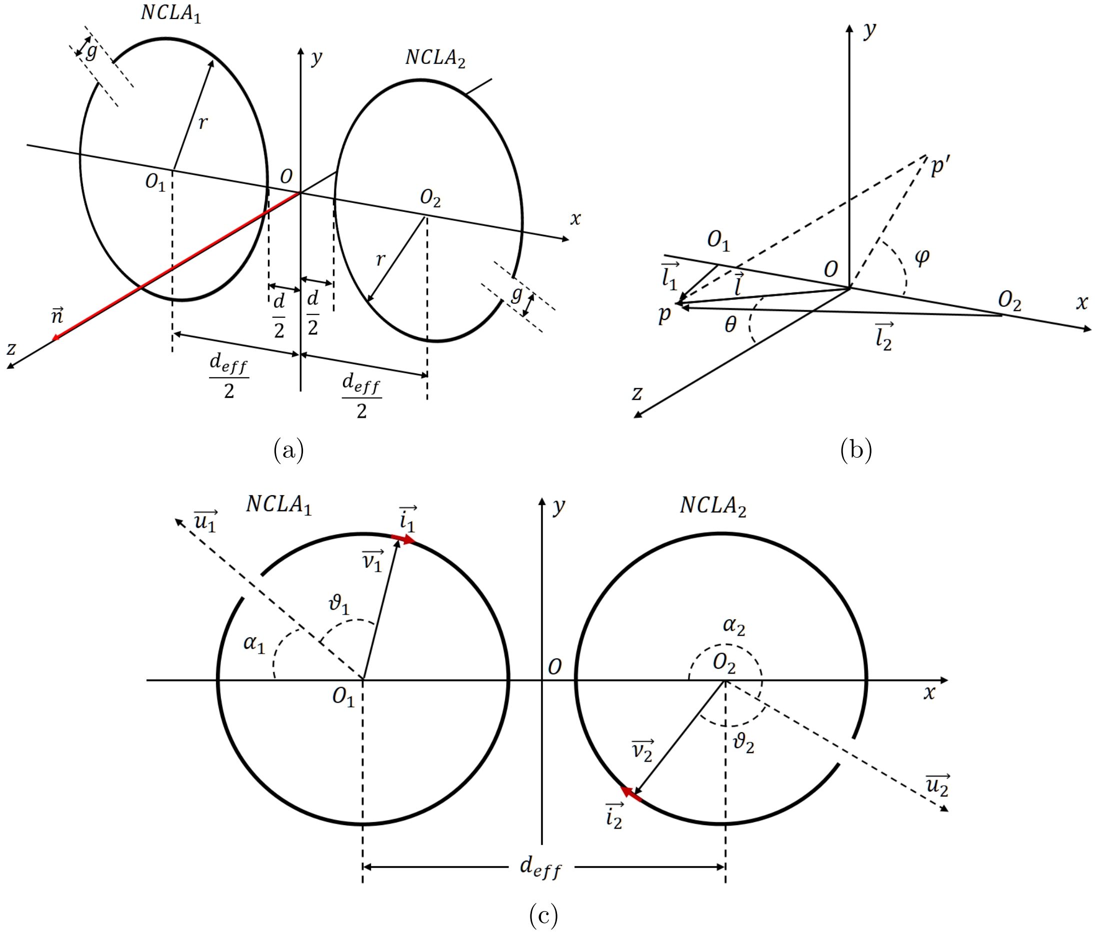

Figure 3.13: (a) One array of two electrically small slotted CLAs carrying non-uniform currents (NCLAs), (b) its coordinate system and (c) its top view: O_1 and O_2 are the two NCLAs' centres, d_{eff} is the distance between O_1 and O_2, $d = d_{eff} - 2r$, g is the same dimension of the two elements' gaps; Vectors $\vec{u_1}$ and $\vec{u_2}$, along with angles α_1 and α_2, are defined to determine the two NCLAs' rotating orientations; While Vectors $\vec{\nu_1}$ and $\vec{\nu_2}$, along with angles ϑ_1 and ϑ_2, are defined to indicate specific locations of currents $\vec{i_1}$ and $\vec{i_2}$ on the two NCLAs.

For any of following derivations and calculations, a harmonic time dependence $e^{i\omega t}$ is always assumed: i is the imaginary unit, ω is the angular frequency. Then the electric field can be expressed as Equation 3.16 using Ampère's circuital law (with

Maxwell's addition) [99] [100].

$$\vec{E} = \frac{1}{i\epsilon_0\mu_0\omega}\left(\nabla \times \vec{B} - \mu_0\vec{J}\right) \tag{3.16}$$

where ϵ_0 is the free space permittivity, μ_0 is the free space permeability, $\vec{B}$ is the magnetic field, and $\vec{J}$ is the electric current density. The magnetic field can also be written as the curl of the magnetic potential: $\nabla \times \vec{A}$. Thus, using the property of cross product, the electric field now becomes [99]:

$$\vec{E} = \frac{1}{i\epsilon_0\mu_0\omega}\left[\nabla\left(\nabla \cdot \vec{A}\right) - \nabla^2\vec{A} - \mu_0\vec{J}\right] \tag{3.17}$$

For a homogeneous medium, using the Lorenz gauge, there is an expression [99] [100]:

$$-\mu_0\vec{J} = \nabla^2\vec{A} + \epsilon_0\mu_0\omega^2\vec{A} \tag{3.18}$$

Substituting Equation 3.18 into Equation 3.17, the electric field can now be expressed only in term of magnetic potential $\vec{A}$ as:

$$\vec{E} = -\frac{i}{\epsilon_0\mu_0\omega}\nabla\left(\nabla \cdot \vec{A}\right) - i\omega\vec{A} \tag{3.19}$$

In far field, the radiation fields of an antenna can be treated as a plane wave. Therefore, the following approximation can be adopted here:

$$\nabla \sim -ik\hat{l} \tag{3.20}$$

where $\hat{l}$ is the unit vector pointing the observation point. Then considering the total far field radiation sphere, the electric field can be further simplified as:

$$\vec{E} = -i\omega\left(\hat{\theta}A_\theta + \hat{\varphi}A_\varphi\right) \tag{3.21}$$

The NCLAs shown in Figure 3.13 are infinitely thin loops, so the filament current approximation can be used here [101]. Thus, the vector magnetic potential for these two NCLA elements can be calculated through:

$$\vec{A}_{1,2} = \frac{\mu_0 r}{4\pi} \int_{\vartheta_0}^{\vartheta'} \vec{i}_{1,2} \left(\vartheta_{1,2} + \alpha_{1,2}\right) \frac{e^{-ikLEN\left(\vec{\nu}_{1,2},\vec{l}_{1,2}\right)}}{LEN\left(\vec{\nu}_{1,2},\vec{l}_{1,2}\right)} d\vartheta_{1,2} \tag{3.22}$$

where $\vartheta_0 = \sin^{-1}(g/2r_{eff})$ and $\vartheta' = 2\pi - \sin^{-1}(g/2r_{eff})$ are the staring and ending points of the integral, corresponding to the two edges of the gap of each of the two elements, and $LEN\left(\vec{\nu}_{1,2},\vec{l}_{1,2}\right) = \left|\vec{l}_{1,2} - \vec{\nu}_{1,2}\right|$ are the distances from the points on the two elements ,corresponding to the angles $\vartheta_{1,2} + \alpha_{1,2}$, to the observation point p, corresponding to the vector $\vec{l}_{1,2}$, respecting to the local origins $O_{1,2}$. Here, using far field approximations shown in Equation 3.23, the magnetic potential is turned into Equation 3.24.

$$LEN\left(\vec{\nu}_{1,2},\vec{l}_{1,2}\right) \simeq l - \vec{\nu}_{1,2} \cdot \hat{l} \quad \text{for phase variations} \tag{3.23a}$$

$$LEN\left(\vec{\nu}_{1,2},\vec{l}_{1,2}\right) \simeq l \qquad \text{for amplitude variations} \tag{3.23b}$$

$$\vec{A}_{1,2} = \frac{\mu_0 r}{4\pi} \frac{e^{-ikl}}{l} \int_{\vartheta_0}^{\vartheta'} \vec{i}_{1,2} \left(\vartheta_{1,2} + \alpha_{1,2}\right) e^{ik\vec{\nu}_{1,2}\cdot\hat{l}} d\vartheta_{1,2} \tag{3.24}$$

Applying the coordinate systems' transformation knowledge, $\vec{\nu}_{1,2} \cdot \hat{l}$ can be calculated as:

$$\vec{\nu}_1 \cdot \hat{l} = -r \sin\theta \cos(\varphi + \vartheta_1 + \alpha_1) - \frac{d_{eff}}{2} \sin\theta \cos\varphi \tag{3.25a}$$

$$\vec{\nu}_2 \cdot \hat{l} = -r \sin\theta \cos(\varphi + \vartheta_2 + \alpha_2) + \frac{d_{eff}}{2} \sin\theta \cos\varphi \tag{3.25b}$$

Borrowing the method of determining the current in [10] for calculating the radiation fields of a small loop antenna, the currents $\vec{i}_{1,2}(\vartheta_{1,2} + \alpha_{1,2})$ can be expressed as:

$$\vec{i}_1(\vartheta_1 + \alpha_1) = \hat{\varphi}\left[-i_{\varphi 1}(\vartheta_1)\cos(\varphi + \vartheta_1 + \alpha_1)\right] \tag{3.26a}$$

$$\vec{i}_2(\vartheta_2 + \alpha_2) = \hat{\varphi}\left[-i_{\varphi 2}(\vartheta_2)\cos(\varphi + \vartheta_2 + \alpha_2)\right] \tag{3.26b}$$

Then substituting Equation 3.25 and Equation 3.26 back into Equation 3.24, the magnetic potential now can be written as:

$$\begin{aligned}\vec{A}_1 =& \hat{\varphi} A_{\varphi 1} \\ =& \hat{\varphi}\frac{\mu_0 r}{4\pi}\frac{e^{-ikl}}{l}e^{-ik\frac{d_{eff}}{2}\sin\theta\cos\varphi} \\ &\times \int_{\vartheta_0}^{\vartheta'} -i_{\varphi 1}\left(\vartheta_1\right)\cos(\varphi + \vartheta_1 + \alpha_1)e^{ikr\sin\theta\cos(\varphi+\vartheta_1+\alpha_1)}d\vartheta_1\end{aligned} \tag{3.27a}$$

$$\begin{aligned}\vec{A}_2 =& \hat{\varphi} A_{\varphi 2} \\ =& \hat{\varphi}\frac{\mu_0 r}{4\pi}\frac{e^{-ikl}}{l}e^{ik\frac{d_{eff}}{2}\sin\theta\cos\varphi} \\ &\times \int_{\vartheta_0}^{\vartheta'} -i_{\varphi 2}\left(\vartheta_2\right)\cos(\varphi + \vartheta_2 + \alpha_2)e^{ikr\sin\theta\cos(\varphi+\vartheta_2+\alpha_2)}d\vartheta_2\end{aligned} \tag{3.27b}$$

Now substituting Equation 3.27 into Equation 3.21, the far field radiation electric field can be calculated as:

$$\begin{aligned}\vec{E}_1 =& \hat{\varphi} E_{\varphi 1} = \hat{\varphi}\left(-i\omega A_{\varphi 1}\right) \\ =& \hat{\varphi}\frac{-i\mu_0 \omega r}{4\pi}\frac{e^{-ikl}}{l}e^{-ik\frac{d_{eff}}{2}\sin\theta\cos\varphi} \\ &\times \int_{\vartheta_0}^{\vartheta'} -i_{\varphi 1}\left(\vartheta_1\right)\cos(\varphi + \vartheta_1 + \alpha_1)e^{ikr\sin\theta\cos(\varphi+\vartheta_1+\alpha_1)}d\vartheta_1\end{aligned} \tag{3.28a}$$

$$
\begin{aligned}
\vec{E}_2 =& \hat{\varphi} E_{\varphi 2} = \hat{\varphi}\left(-i\omega A_{\varphi 2}\right) \\
=& \hat{\varphi}\frac{-i\mu_0 \omega r}{4\pi}\frac{e^{-ikl}}{l} e^{ik\frac{d_{eff}}{2}\sin\theta\cos\varphi} \\
& \times \int_{\vartheta_0}^{\vartheta'} -i_{\varphi 2}\left(\vartheta_2\right)\cos(\varphi+\vartheta_2+\alpha_2) e^{ikr\sin\theta\cos(\varphi+\vartheta_2+\alpha_2)} d\vartheta_2
\end{aligned}
\tag{3.28b}
$$

The average radiation energy density in far field is then can be computed through:

$$
P_a(l,\theta,\varphi) = \frac{\left|E_{\varphi 1} + E_{\varphi 2}\right|^2}{2Z_0}
\tag{3.29}
$$

Once the elements' dimensions, the operation frequency and the observation point are fixed, the term $-i\mu_0 r e^{-ikl}/(4\pi l)$ can be treated as a constant. Thus, the normalized far field average radiation energy density can be expressed as:

$$
\begin{aligned}
P_{an}(\theta,\varphi) =& \frac{P_a(l,\theta,\varphi) 2Z_0}{\left|\dfrac{-i\mu_0 r e^{-ikl}}{4\pi l}\right|^2} \\
=& \omega^2 \left| \sum_{m=1}^{2} e^{(-1)^m ik\frac{d_{eff}}{2}\sin\theta\cos\varphi} \right. \\
& \left. \times \int_{\vartheta_0}^{\vartheta'} -i_{\varphi m}\left(\vartheta\right)\cos(\varphi+\vartheta+\alpha_m) e^{ikr\sin\theta\cos(\varphi+\vartheta+\alpha_m)} d\vartheta \right|^2
\end{aligned}
\tag{3.30}
$$

The normalized current distribution $i_{\varphi nm}(\vartheta)$ $(m = 1,2)$ can be known from [102] [103] [104] as (Details are further explained in Chapter 4.):

$$
\begin{aligned}
i_{\varphi nm}(\vartheta) =& \frac{i_{\varphi m}(\vartheta)}{I_m} \\
=& \frac{i_{\varphi m}(\vartheta)}{i_{\varphi m}(\pi)} \qquad\qquad (m = 1,2) \\
=& \left| \frac{\ln\left\{\sin\left[\frac{1}{2}\sin^{-1}\left(\frac{g}{2r}\right)\right]\right\} - \ln\left[\sin\left(\frac{\vartheta}{2}\right)\right]}{\ln\left\{\sin\left[\frac{1}{2}\sin^{-1}\left(\frac{g}{2r}\right)\right]\right\}} \right|
\end{aligned}
\tag{3.31}
$$

So now the normalized far field average radiation energy density becomes:

$$\begin{aligned} P_{an}(\theta,\varphi) =& \omega^2 \Bigg| \sum_{m=1}^{2} I_m e^{(-1)^m ik\frac{d_{eff}}{2}\sin\theta\cos\varphi} \\ & \times \int_{\vartheta_0}^{\vartheta'} -i_{\varphi nm}(\vartheta)\cos(\varphi+\vartheta+\alpha_m) e^{ikr\sin\theta\cos(\varphi+\vartheta+\alpha_m)} d\vartheta \Bigg|^2 \end{aligned} \tag{3.32}$$

where $I_{1,2} = i_{\varphi 1,2}(\pi)$ are respectively the currents, with maximum magnitudes, on the first and second NCLA element, which can also be regarded as the excitation coefficients. Their values will be determined in next chapter.

3.6 Conclusion

In conclusion, even though for an array of two isotropic radiators, an array of two magnetic dipoles and an array of two CLAs, the theoretical limit directivity values (4, 5.25 and 5.25) can be achieved with appropriate combinations of small separation distance d_{eff} and near-π phase difference β, the largest directivity of an array of two electrically small CLAs which have a similar electrical size, with what $r = 10.6mm$ working at $f = 1.9GHz$ indicates, can only be lower than 5.

Analogous to the pattern multiplication rule, the far field radiated energy density of an array of two identical elements, with different excitation currents (even only one element excited), can be calculated through calculating the product of the first element's far field radiated energy density and an energy array factor.

Specifically for an arbitrary parasitic array of two identical magnetic dipoles, when its maximum endfire directivity is achieved, there exists a following relationship: $Q|\kappa| = \gamma\lambda/d_{eff}$ (γ is a constant value around 0.75).

Through a detailed derivation, the far field radiation energy pattern of an array of two NCLAs only depends on the operational frequency f, the elements' separation distance d_{eff} and the rotating orientation angles α_1 and α_2, if the two elements' maximum currents, I_1 and I_2, are known. To determine these maximum currents will be one key topic in next chapter.

Chapter 4

Metamaterial Electrically Small Two-Element Parasitic Arrays and Superdirectivity

A two-element parasitic array comprised of identical electrically small metamaterial elements is studied in this chapter based on two main approximations: 1. In order to analyse the array's current behaviours (mainly the maximum currents carried by the two elements), one single metamaterial element, a standard singly split ring resonator (SSRR), is treated as a resonant LCR circuit; 2. For calculating the array's radiated energy, the array is regarded as an array of two NCLAs (introduced in Chapter 3).

First, the concept of metamaterials is briefly explained. Then an equivalent LCR circuit of a single standard SSRR is illustrated, and the relevant circuit' electrical components' values (inductance L, capacitance C and resistance R) are identified through a numerical regression subject to simulation results. Next, based on the single SSRR's equivalent circuit, a new equivalent circuit for a two-SSRR parasitic array is introduced, which leads to the recognition of the two coupled SSRRs' maximum currents, key required values to calculate the array's radiated energy. Then combining this equivalent circuit and the method of calculating a two-NCLA array's radiated energy (introduced in Section 3.5) forms an analytical model, which allows to easily but accurately predict the far field radiation behaviours of an electrically small parasitic array of two SSRRs (the two SSRRs are not necessarily standard and identical), based on certain information of the array. Then a directivity map for such a two-SSRR parasitic array is produced and the right conditions, with which the highest directivity can be reached, is identified for the design of a superdirective array. In the end, the importance of the forementioned analytical model is discussed.

The main new contributions in this Chapter include: 1. The new equivalent circuits for a single SSRR and for a two-SSRR parasitic array; 2. A new method of calculating the mutual capacitance between two SSRRs; 3. A new compact analytical model for predicting the far field radiation behaviours of a two-SSRR parasitic array; 4. An endfire directivity map for a two-SSRR parasitic array and a 'CC' superdirective structure predicted by the analytical model.

4.1 Metamaterials

One commonly accepted definition of metamaterials is that a metamaterial is an artificial material in which the electromagnetic properties, as presented by the permittivity and permeability, can be controlled. Metamaterials are made up of periodic arrays of metallic resonant elements. Both the size of the element and the unit cell are small relative to the free space wavelength [98].

Metamaterials can be epsilon negative materials (ENG), mu negative materials (MNG), or double negative materials (DNG) [105]. The metamaterial elements used in this thesis, namely SSRR (the simplest realization of an LC circuit as a metamaterial element), is a type of MNG.

4.2 Singly Split Ring Resonator

The equivalent LCR circuit for an electrically small standard SSRR (see Figure 4.1(a)), considering the similarity between this SSRR and a loop antenna [106] [10] [107], is introduced and displayed in Figure 4.1(b). The SSRR's dimension is: $r = 0.011m$, $g = 0.002m$, $h = 0.005m$, $w = 0.0008m$ and $r_{eff} = r - w/2 = 0.0106m$, while the electrical components (inductance L, capacitance C and resistance R) of the equivalent circuit are yet to be determined.

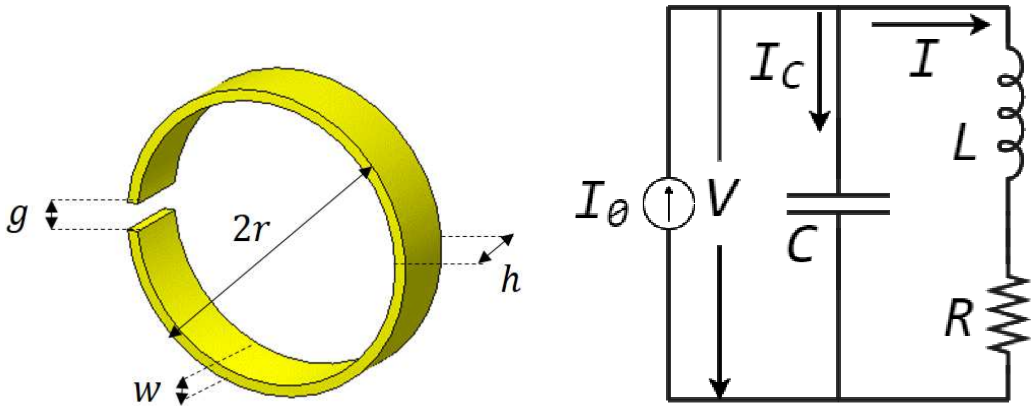

(a) (b)

Figure 4.1: (a) A standard SSRR and (b) its equivalent circuit.

Conventionally a SSRR is treated as a one turn circular coil of rectangular section, and its self-inductance L can be calculated through [108] [109]:

$$L = \mu_0 r_{eff} \left\{ \left[1 + \frac{0.6711(h+w)^2}{16 r_{eff}^2} \right] \ln \frac{8 r_{eff}}{0.2237(h+w)} - \left[2 + \frac{0.2237(h+w)^2}{16 r_{eff}^2} \right] \right\} \tag{4.1}$$

where μ_0 is the free space permeability. Because the ring's height h and thickness w are both fairly small compared with its effective radius r_{eff}, Equation 4.1 can be simplified and rewritten as Equation 4.2 [97], which is easier to use. The value of this

SSRR's inductance is then $2.907 \times 10^{-8}H$.

$$L = \mu_0 r_{eff} \left[\ln \frac{8r_{eff}}{(h+w)} - \frac{1}{2} \right] \tag{4.2}$$

For calculating the self-capacitance, a SSRR can be modelled as a one turn circular coil with a long enough circumference, a small enough gap and a high enough conductivity [102]. Via analysing the electric field and the surface charges, the self-capacitance C can be obtained through [97] [103]:

$$C = \varepsilon_0 \left[\frac{(h+g)(w+g)}{g} + \frac{2(h+w)}{\pi} \ln \frac{4r_{eff}}{g} \right] \tag{4.3}$$

where ε_0 is the free space permittivity. The capacitance value is $1.866 \times 10^{-13}F$.

The input impedance of the SSRR can be expressed in terms of the L, C and R as:

$$Z_{in} = \frac{1}{\dfrac{1}{R + i\omega L} + i\omega C} \tag{4.4}$$

where a time dependence factor $e^{i\omega t}$ is adopted. Letting the imaginary part of the Z_{in} equal to zero, the circuit's angular resonance frequency can be calculated using Equation 4.5. According to the impedance curve (Figure 4.2) produced by a simulation using the CST MW Studio, the SSRR's resonance frequency is $1.957GHz$. Substituting this frequency value, along with the values of L and C, into Equation 4.5, the circuit's resistance R can be computed and its value is 167.383Ω.

$$\omega_0 = 2\pi f_0 = \sqrt{\frac{1}{LC} - \left(\frac{R}{L}\right)^2} \tag{4.5}$$

Knowing the values of L, C and R, the analytical input impedance can be calculated. This analytically calculated impedance is plotted against frequency f and displayed in Figure 4.3, with the simulation data of Figure 4.2 as a reference. Apparently the analytical result shows a failure of describing the SSRR's impedance be-

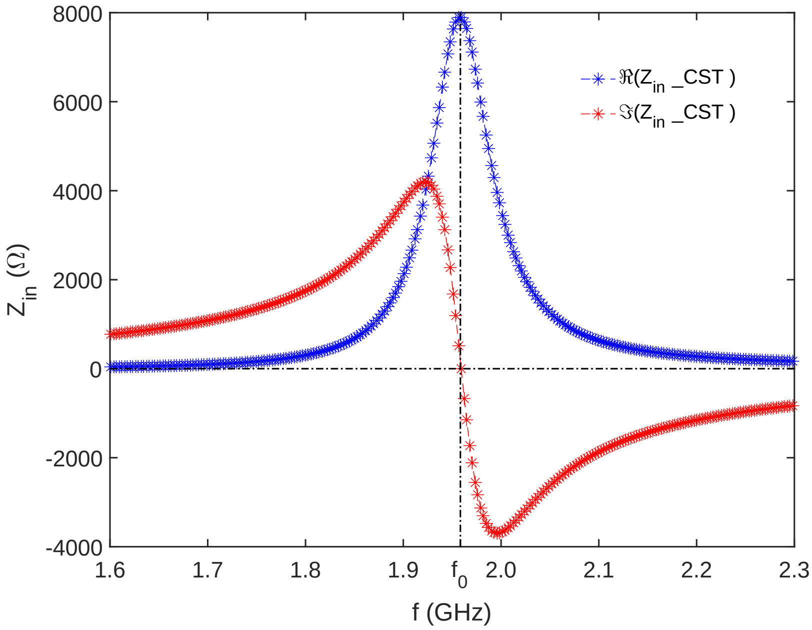

Figure 4.2: The input impedance of the SSRR, where $\Re(Z_{in}\_CST)$ and $\Im(Z_{in}\_CST)$ are respectively the real and imaginary parts; $\Im(Z_{in}) = 0$, for $f_0 = 1.957GHz$: from CST simulations.

haviour. Because the value of R is calculated using the resonance frequency provided by simulations, it can be easily concluded that both Equation 4.2 and Equation 4.3 are suitable for the equivalent circuit of a small loop antenna [10] rather than this equivalent circuit shown in Figure 4.1 for a SSRR.

In order to settle the significant disagreement problem shown in Figure 4.3, a new purely numerical method of determining L, C and R is introduced. Since the CST simulations' data is commonly accepted to be reliable, it is reasonable to directly use the CST data of input impedance and current as the reference for a curve fitting operation of Equation 4.4 and Equation 4.6. The MATLAB function $lsqcurvefit$ [110] allows such a non-linear fitting to be implemented and meanwhile provides the corresponding values of L, C and R for the fitted curves. Equation 4.6, with Kirchhoff's Current Law used [111] and the source current (I_0) set to be $1A$, provides the maximum current carried by the excited SSRR. The fitted curves are plotted and presented in Figure 4.4 and Figure 4.5, with the simulation results as references. The finally

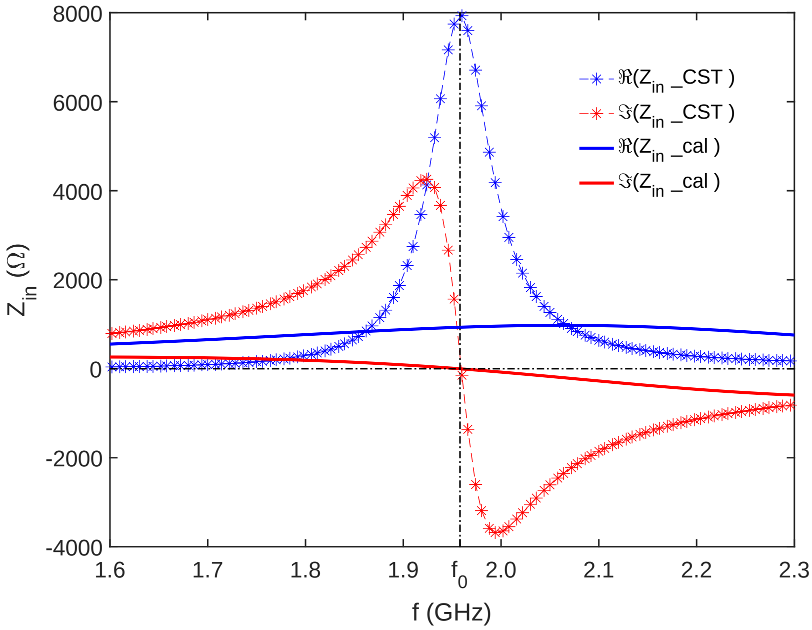

Figure 4.3: The numerically simulated result and the analytically calculated result of the SSRR's impedance, where $\Re(Z_{in}\_cal)$ and $\Im(Z_{in}\_cal)$ are respectively the real and imaginary parts of the analytically calculated input impedance.

determined values of L, C and R for the fitted curves are respectively $2.402 \times 10^{-8} H$, $2.751 \times 10^{-13} F$ and 10.065Ω.

$$\begin{aligned} I &= \frac{I}{I_0} \\ &= \frac{\frac{1}{i\omega L}}{\frac{1}{i\omega L} + i\omega C + \frac{1}{R}} \end{aligned} \tag{4.6}$$

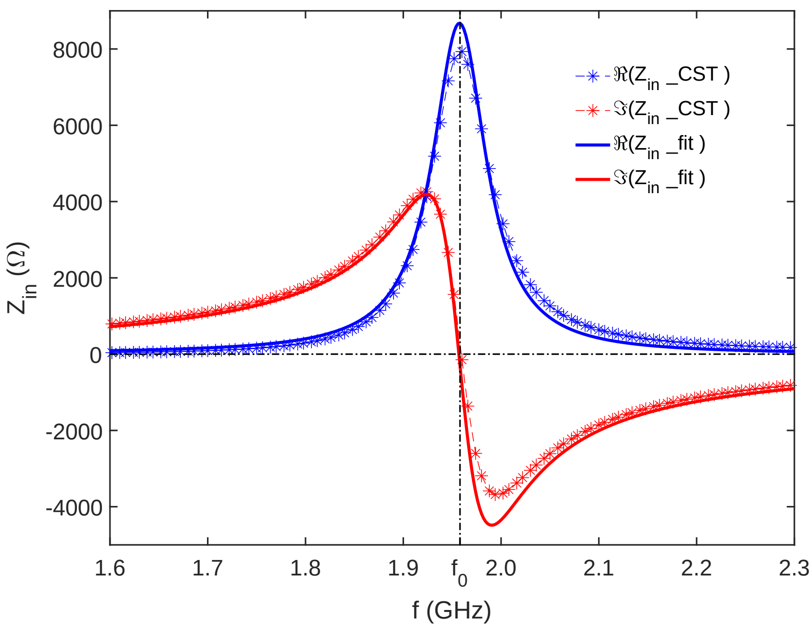

Figure 4.4: The best fitted curves of the SSRR's impedance, where $\Re(Z_{in}\_fit)$ and $\Im(Z_{in}\_fit)$ are respectively the real and imaginary parts of the best fitted input impedance.

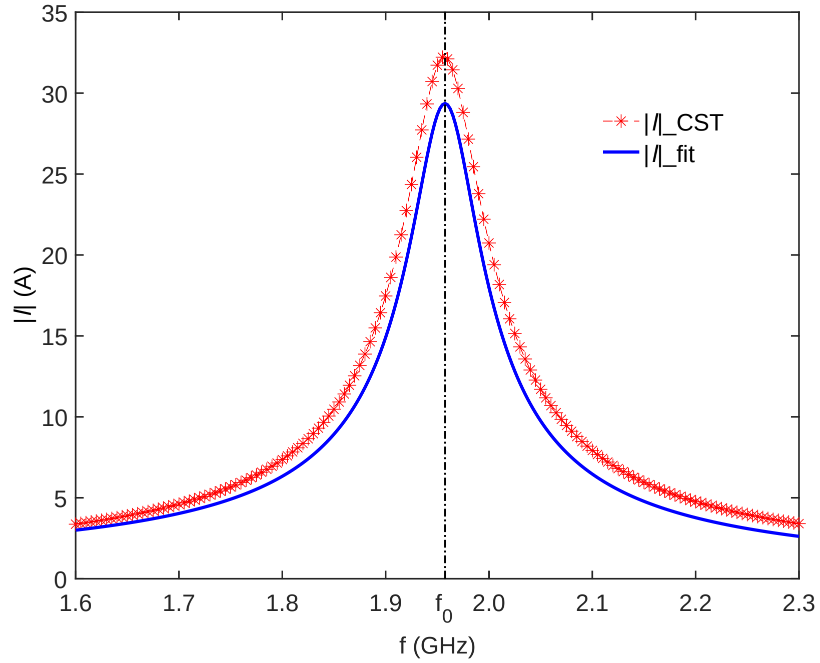

(a)

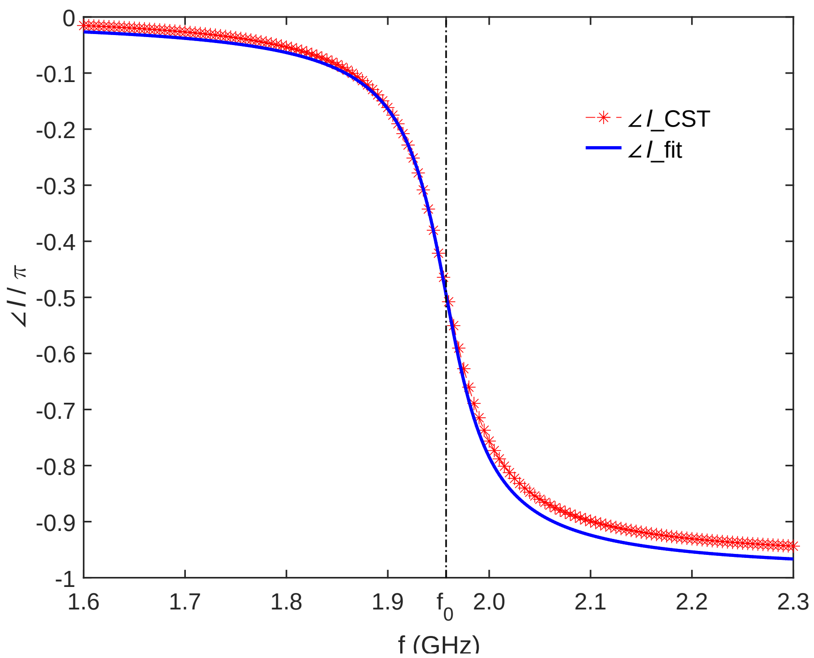

(b)

Figure 4.5: (a) The amplitude and (b) the phase of the circuit current I.

The simulation model for obtaining the CST current data is shown in Figure 4.6, where an ideal current port, which supplies a current of $I_0 = 1A$, is applied to the SSRR. With the CST Frequency Domain Solver used and a rectangular curve Υ ($5.6mm \times 1.4mm$) defined, CST can efficiently figure out the current threading the surface enclosed by Υ through implementing the Ampere's Law [112] [113] [114]. In reality, the SSRR surely has a non-uniform current distribution, and Υ's position implies that the simulated current data obtained is the maximum current [115] [104]. For the purpose of this project, the equivalent circuit introduced here is only to describe a SSRR element's maximum current behaviours.

Based on the very good agreement shown in Figure 4.4 and Figure 4.5, it is very easy to conclude that the equivalent circuit proposed in Figure 4.1, along with its numerically determined components' values, is well working for describing a standard SSRR element's impedance and current behaviours.

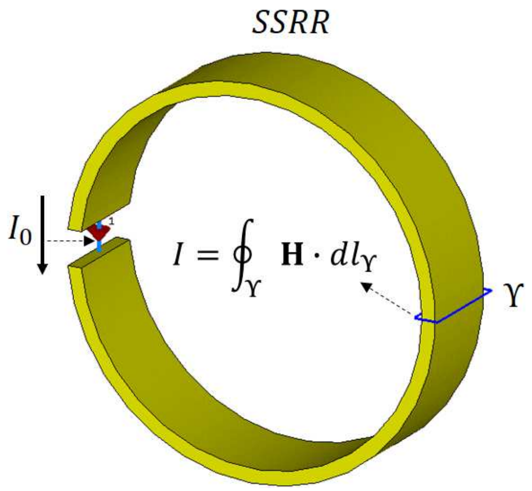

Figure 4.6: The CST simulation model for a standard SSRR to acquire the current-frequency curve, where I_0 is the source current generated by an ideal current port, Υ is a rectangular curve defined at the opposite-to-the-gap position on the ring to perform the Ampere's Law.

There are two main reasons why the simulation data of the CST MW Studio can be regarded as being reliable and accurate. First, sufficient research [116–125] which involve comparisons between measured results and the studio's simulation results have supported the studio's reliability and accuracy. Second, the simulation of the CST STUDIO SUITE is based on the Finite Integration Technique (FIT). The technique mainly applies the integral form of Maxwell's equations to a specific domain which is split into many small elements through creating a suitable mesh system [126] [127]. Therefore if both the calculation domain (here a Perfectly Matched Layer-PML boundary) and the mesh system are properly defined, the simulation result would be very accurate. The important settings of the CST MW Studio for all simulations in this thesis are listed in Table 4.1 and the mesh views for a single SSRR and the bounding box in the studio are shown in Figure 4.7.

Background material	Vacuum (normal)
Boundary condition	Open (add space)
PML boundary: Estimated reflection level	0.0001
PML boundary: Automatic minimum distance to structure	2λ at $1GHz$
Frequency	$1 \sim 3GHz$
Frequency domain solver: Broadband sweep	General purpose
Frequency domain solver: Mesh type	Tetrahedral
Adaptive mesh refinement: Passes	$8 \sim 18$
Adaptive mesh refinement: S-parameter criterion	Threshold 0.002, Checks 2

Table 4.1: The important settings of the CST MW Studio for all simulations in this thesis.

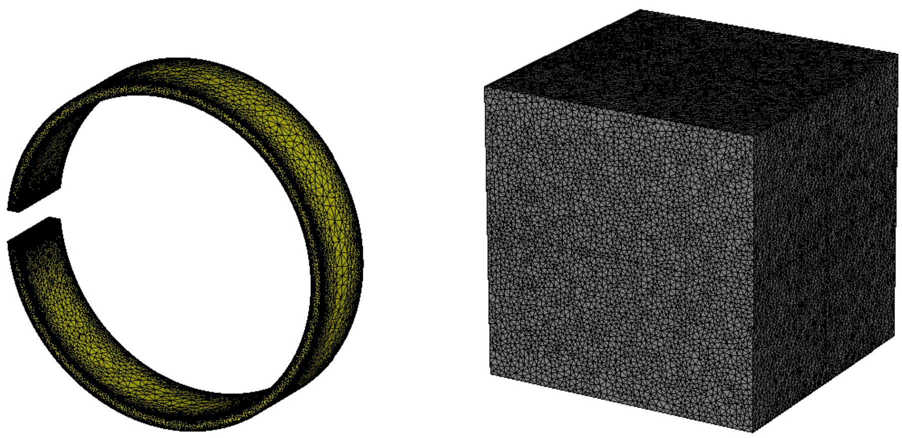

(a) (b)

Figure 4.7: The mesh views of (a) a single SSRR element and (b) the bounding box (PML boundary).

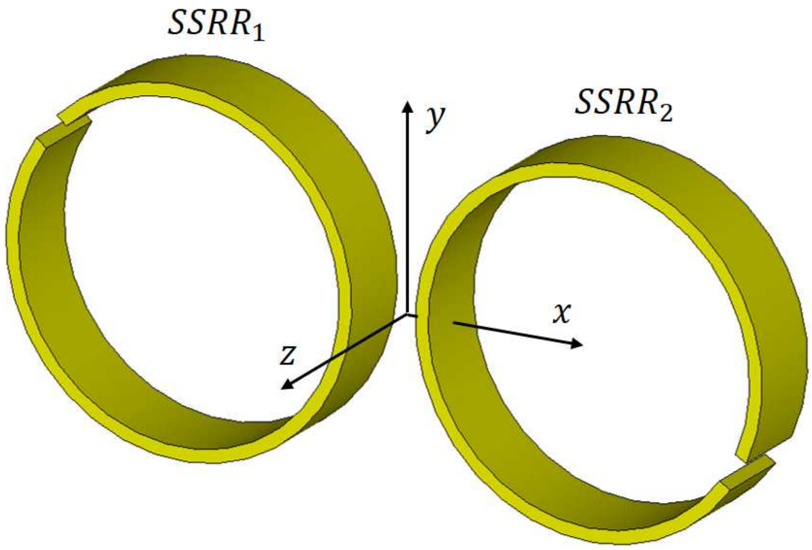

(a)

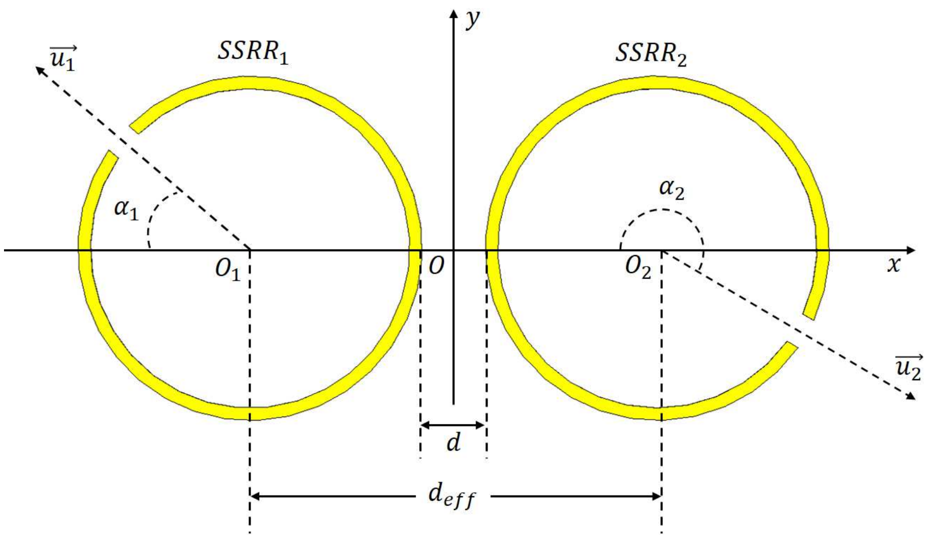

(b)

Figure 4.8: (a) The perspective view and (b) the top view of a two-SSRR array, where virtual vectors $\vec{u_1}$ and $\vec{u_2}$ are defined to control the two elements' orientations through changing the angles α_1 and α_2; α_1 and α_2 can be arbitrary values in between 0 and 2π.

4.3 Two-SSRR Parasitic Array: Circuit and Currents

Based on the single SSRR's equivalent circuit, it is convenient to analytically model a two-SSRR parasitic array, shown in Figure 4.8, as a lumped circuit presented in Figure 4.9 [97] [128] [129]. L_m and C_m together represent the mutual coupling between the two SSRR elements, and their expressions can be directly derived from the calculation of mutual energy [115] [130].

In this Section, in order to obtain the two SSRRs' maximum currents (I_1 and I_2) for calculating the two-SSRR array's radiated energy: Firstly a circuit analysis is performed according to Figure 4.9, leading to the expressions of the two maximum currents; Then the mutual coupling (L_m and C_m) is thoroughly investigated, which makes the currents' expressions practically usable.

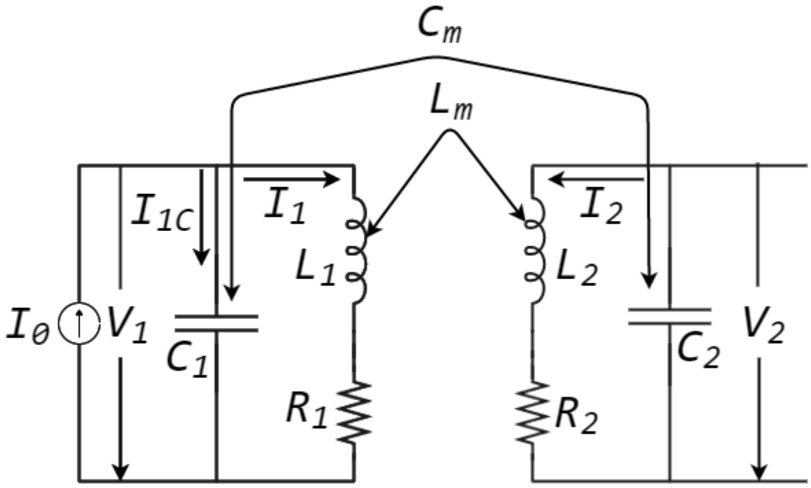

Figure 4.9: The equivalent circuit for a two-SSRR parasitic array, where only the first element is excite by an ideal current source, L_m is the mutual inductance and C_m is the mutual capacitance, these two terms together present the mutual coupling between the two SSRRs.

4.3.1 Circuit Analysis

For Figure 4.9, using both Kirchhoff's Voltage Law and Current Law [111], the following four equations can be written:

$$V_1 = i\omega(L_1 I_1 + L_m I_2) + I_1 R_1 \tag{4.7a}$$

$$V_2 = i\omega(L_m I_1 + L_2 I_2) + I_2 R_2 \tag{4.7b}$$

$$I_{1C} = i\omega(C_1 V_1 + C_m V_2) \tag{4.7c}$$

$$-I_2 = i\omega(C_m V_1 + C_2 V_2) \tag{4.7d}$$

where a time dependence of $e^{i\omega t}$ is assumed. Dividing Equation 4.7a and Equation 4.7b by V_1 on both sides, two new equations can be obtained as:

$$1 = (i\omega L_1 + R_1)\frac{I_1}{V_1} + i\omega L_m \frac{I_2}{V_1} \tag{4.8a}$$

$$\frac{V_2}{V_1} = i\omega L_m \frac{I_1}{V_1} + (i\omega L_2 + R_2)\frac{I_2}{V_1} \tag{4.8b}$$

Considering Equation 4.7d, the term I_2/V_1 can be easily got as:

$$\frac{I_2}{V_1} = -i\omega C_m - i\omega C_2 \frac{V_2}{V_1} \tag{4.9}$$

Then applying Equation 4.9 to Equation 4.8 and eliminating the term V_2/V_1, the normalized current I_1/V_1 is now:

$$\frac{I_1}{V_1} = \frac{\dfrac{\omega^2 L_m C_m - 1}{\omega^2 L_m C_2} - \dfrac{\omega^2 L_2 C_m - i\omega C_m R_2}{\omega^2 L_2 C_2 - i\omega C_2 R_2 - 1}}{\dfrac{i\omega L_m}{\omega^2 L_2 C_2 - i\omega C_2 R_2 - 1} - \dfrac{i\omega L_1 + R_1}{\omega^2 L_m C_2}} \tag{4.10}$$

Then the term V_2/V_1 can be expressed in term of I_1/V_1 as:

$$\frac{V_2}{V_1} = \frac{1 - \omega^2 L_m C_m - (i\omega L_1 + R_1)\dfrac{I_1}{V_1}}{\omega^2 L_m C_2} \tag{4.11}$$

Substituting Equation 4.11 back into Equation 4.9 and Equation 4.7c, the normalized I_2/V_1 and I_{1C}/V_1 can be calculated. Therefore, the required currents I_1 and I_2 can be calculated through Equation 4.12 given that the source current I_0 is set to be $1A$, once the normalized I_1/V_1 can be computed. On the right-hand side of Equation 4.10, only L_m and C_m are unknown. The mutual inductance L_m and the mutual capacitance C_m, derived from the mutual magnetic and electric energy of the two SSRRs, are about to be determined in next Subsection.

$$\frac{I_0}{V_1} = \frac{I_1}{V_1} + \frac{I_{1C}}{V_1} \tag{4.12a}$$

$$I_1 = \frac{I_1}{I_0} = \frac{I_1/V_1}{I_0/V_1} \tag{4.12b}$$

$$I_2 = \frac{I_2}{I_0} = \frac{I_2/V_1}{I_0/V_1} \tag{4.12c}$$

4.3.2 Mutual Coupling

In order to calculate the mutual inductance L_m and the mutual capacitance C_m, new vectors, scalars and angles are defined and shown in the following sketch. Where the two SSRRs are treated as two infinite thin red open circular strings.

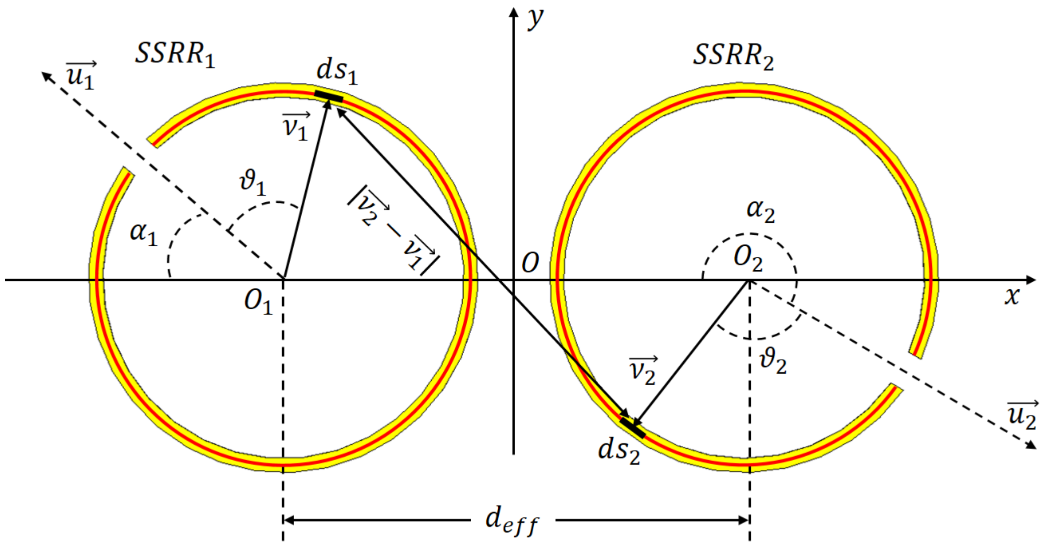

Figure 4.10: A sketch of the two-SSRR array for calculating the mutual inductance and the mutual capacitance, where the two elements are treated as two infinite thin red open circular strings, ds_1 and ds_2 are two arbitrary infinitesimal lengths of the two strings; Vectors $\vec{\nu_1}$ and $\vec{\nu_2}$, along with angles ϑ_1 and ϑ_2, are defined to indicate the positions of ds_1 and ds_2.

4.3.2.1 Mutual Inductance

From the perspective of circuit theory, it is not difficult to realize that the mutual magnetic energy of the array in Figure 4.10 can be expressed in term of mutual inductance and currents as [131]:

$$W_{m,mut} = L_m I_1 I_2 \tag{4.13}$$

where I_1 and I_2 are the maximum currents flowing along the two rings, according to Section 4.2, and also the currents flowing through the circuit's two self-inductors, corresponding to the circuit in Figure 4.9.

While from the field perspective, the mutual magnetic energy can also be calculated through the following equation [97] [131]:

$$W_{m,mut} = \frac{1}{2} \int_V \left(\vec{A_1} \cdot \vec{J_2} + \vec{A_2} \cdot \vec{J_1} \right) dV \tag{4.14}$$

where $\vec{J_1}$ and $\vec{J_2}$ are the two SSRRs' current densities, $\vec{A_1}$ and $\vec{A_2}$ are respectively the vector potentials generated by the first SSRR's current and the second SSRR's current. The retarded vector potential at position $\vec{\nu}$ created by a current located at $\vec{\nu'}$ can be expressed as [97] [99]:

$$\vec{A}\left(\vec{\nu}\right) = \frac{\mu_0}{4\pi} \int_V \frac{\vec{J}\left(\vec{\nu'}\right) e^{-ik|\vec{\nu}-\vec{\nu'}|}}{|\vec{\nu} - \vec{\nu'}|} dV' \tag{4.15}$$

Combining Equation 4.15 with Equation 4.14 and then applying the symmetry: $\int_V \vec{A_1} \cdot \vec{J_2} dV = \int_V \vec{A_2} \cdot \vec{J_1} dV$, the mutual magnetic energy for the system of Figure 4.10 is now:

$$W_{m,mut} = \frac{\mu_0}{4\pi} \int_V \int_V \frac{\vec{J_1}\left(\vec{\nu_1}\right) \cdot \vec{J_2}\left(\vec{\nu_2}\right) e^{-ik|\vec{\nu_2}-\vec{\nu_1}|}}{|\vec{\nu_2} - \vec{\nu_1}|} dV_1 dV_2 \tag{4.16}$$

where dV_1 and dV_2 are the infinitesimal volumes of the elements: SSRR_1 and SSRR_2.

For our SSRRs, it is sufficient to neglect the rings' cross-sectional areas. Thus by introducing the filament approximation [132], the current densities at $\vec{\nu_1}$ and $\vec{\nu_2}$ can be replaced by two filament currents $\vec{i_1}\left(\vec{\nu_1}\right)$ and $\vec{i_2}\left(\vec{\nu_2}\right)$, and the double volume integral can be transformed into a double length integral, displayed as Equation 4.17.

$$W_{m,mut} = \frac{\mu_0}{4\pi} \int \int \frac{\vec{i_1}\left(\vec{\nu_1}\right) \cdot \vec{i_2}\left(\vec{\nu_2}\right) e^{-ik|\vec{\nu_2}-\vec{\nu_1}|}}{|\vec{\nu_2} - \vec{\nu_1}|} ds_1 ds_2 \tag{4.17}$$

Treating the two SSRRs as filaments, the position vectors $\vec{\nu_1}$ and $\vec{\nu_2}$ can be replaced by angles $\vartheta_1 + \alpha_1$ and $\vartheta_2 + \alpha_2$, and then the length $|\vec{\nu_2} - \vec{\nu_1}|$ can be expressed as:

$$|\vec{\nu_2} - \vec{\nu_1}| = \delta\nu = \sqrt{\delta x^2 + \delta y^2} \tag{4.18a}$$

$$\delta x = d_{eff} - r_{eff} \cos(\vartheta_2 + \alpha_2) + r_{eff} \cos(\vartheta_1 + \alpha_1) \tag{4.18b}$$

$$\delta y = r_{eff} \sin(\vartheta_2 + \alpha_2) - r_{eff} \sin(\vartheta_1 + \alpha_1) \tag{4.18c}$$

where d_{eff} is the effective separation distance between the two SSRRs and r_{eff} is the SSRRs' effective radius. So in terms of angles, Equation 4.17 can further be transformed into:

$$W_{m,mut} = \frac{\mu_0 r_{eff}^2}{4\pi} \int_{\vartheta_0}^{\vartheta'} \int_{\vartheta_0}^{\vartheta'} \frac{\left|\vec{i_1}\left(\vartheta_1 + \alpha_1\right)\right| \left|\vec{i_2}\left(\vartheta_2 + \alpha_2\right)\right|}{\delta\nu} \times \cos(\vartheta_2 + \alpha_2 - \vartheta_1 - \alpha_1) e^{-ik\delta\nu} d\vartheta_1 d\vartheta_2 \tag{4.19}$$

where ϑ_0 and ϑ' are the angles between the vector $\vec{\nu}_{1,2}$ and the vector $\vec{u}_{1,2}$ when the position vector $\vec{\nu}_{1,2}$ is indicating the gap edges of $\text{SSRR}_{1,2}$. Their values can be calculated through:

$$\vartheta_0 = \sin^{-1}\left(\frac{g}{2r_{eff}}\right) \tag{4.20a}$$

$$\vartheta' = 2\pi - \sin^{-1}\left(\frac{g}{2r_{eff}}\right) \tag{4.20b}$$

Comparing Equation 4.19 with Equation 4.13, the mutual inductance L_m can be computed through:

$$L_m = \frac{\mu_0 r_{eff}^2}{4\pi} \int_{\vartheta_0}^{\vartheta'} \int_{\vartheta_0}^{\vartheta'} \frac{\left|\vec{i}_{1n}\left(\vartheta_1 + \alpha_1\right)\right| \left|\vec{i}_{2n}\left(\vartheta_2 + \alpha_2\right)\right|}{\delta\nu} \times \cos(\vartheta_2 + \alpha_2 - \vartheta_1 - \alpha_1) e^{-ik\delta\nu} d\vartheta_1 d\vartheta_2 \tag{4.21}$$

where $\vec{i}_{1n}\left(\vartheta_1 + \alpha_1\right) = \vec{i_1}\left(\vartheta_1 + \alpha_1\right)/I_1$ and $\vec{i}_{2n}\left(\vartheta_2 + \alpha_2\right) = \vec{i_2}\left(\vartheta_2 + \alpha_2\right)/I_2$ are the normalized values of the currents flowing along the two SSRRs, and I_1 and I_2 are respectively the maximum values of $\left|\vec{i_1}\left(\vartheta_1 + \alpha_1\right)\right|$ and $\left|\vec{i_2}\left(\vartheta_2 + \alpha_2\right)\right|$.

Based on the analytical expression of the electric field of a single-turn conducting coil with an infinitesimal gap [102], the charge density of our SSRRs for any angle $\vartheta_{1,2} + \alpha_{1,2}$ can be obtained as [103] [104]:

$$\rho_{1,2}(\vartheta_{1,2} + \alpha_{1,2}) = (h + w)\frac{\epsilon_0 V_{1,2}}{\pi r_{eff}} \cot\left(\frac{\vartheta_{1,2}}{2}\right) \tag{4.22}$$

where $V_{1,2}$ are the voltages over the gaps of $\mathrm{SSRR}_{1,2}$. With the help of the continuity equation, the magnitude of the filament current can be derived as [97] [104]:

$$\begin{aligned}\left|\vec{i}_{1,2}(\vartheta_{1,2}+\alpha_{1,2})\right| =& i_{\varphi 1,2}(\vartheta_{1,2}) \\ =& \left|2\omega(h+w)\frac{\epsilon_0 V_{1,2}}{\pi}\ln\left\{\frac{\sin\left[\frac{1}{2}\sin^{-1}\left(\frac{g}{2r_{eff}}\right)\right]}{\sin\left(\frac{\vartheta_{1,2}}{2}\right)}\right\}\right|\end{aligned} \tag{4.23}$$

Then after the normalization, the terms $\left|\vec{i_{1n}}\left(\vartheta_1+\alpha_1\right)\right|$ and $\left|\vec{i_{2n}}\left(\vartheta_2+\alpha_2\right)\right|$ in Equation 4.21 are finally acquired as:

$$\begin{aligned}\left|\vec{i}_{1n}\left(\vartheta_1+\alpha_1\right)\right| &= \frac{\left|\vec{i_1}\left(\vartheta_1+\alpha_1\right)\right|}{I_1} \\ &= \frac{i_{\varphi 1}\left(\vartheta_1\right)}{i_{\varphi 1}\left(\pi\right)} \\ &= \left|\frac{\ln\left\{\sin\left[\frac{1}{2}\sin^{-1}\left(\frac{g}{2r_{eff}}\right)\right]\right\}-\ln\left[\sin\left(\frac{\vartheta_1}{2}\right)\right]}{\ln\left\{\sin\left[\frac{1}{2}\sin^{-1}\left(\frac{g}{2r_{eff}}\right)\right]\right\}}\right|\end{aligned} \tag{4.24a}$$

$$\begin{aligned}\left|\vec{i}_{2n}\left(\vartheta_2+\alpha_2\right)\right| &= \frac{\left|\vec{i_2}\left(\vartheta_2+\alpha_2\right)\right|}{I_2} \\ &= \frac{i_{\varphi 2}\left(\vartheta_2\right)}{i_{\varphi 2}\left(\pi\right)} \\ &= \left|\frac{\ln\left\{\sin\left[\frac{1}{2}\sin^{-1}\left(\frac{g}{2r_{eff}}\right)\right]\right\}-\ln\left[\sin\left(\frac{\vartheta_2}{2}\right)\right]}{\ln\left\{\sin\left[\frac{1}{2}\sin^{-1}\left(\frac{g}{2r_{eff}}\right)\right]\right\}}\right|\end{aligned} \tag{4.24b}$$

4.3.2.2 Mutual Capacitance

Following an analogous derivation procedure to that for the mutual inductance, with the vector potentials replaced by scalar potentials and with the current densities replaced by charge densities, the mutual electric energy can be obtained as:

$$W_{e,mut} = \frac{r_{eff}^2}{4\pi\epsilon_0}\int_{\vartheta_0}^{\vartheta'}\int_{\vartheta_0}^{\vartheta'}\frac{\rho_1\left(\vartheta_1+\alpha_1\right)\rho_2\left(\vartheta_2+\alpha_2\right)e^{-ik\delta\nu}}{\delta\nu}d\vartheta_1 d\vartheta_2 \tag{4.25}$$

where ϑ_0 and ϑ' can be calculated through Equation 4.20, $\delta\nu$ is given by Equation 4.18, and $\rho_{1,2}(\vartheta_{1,2}+\alpha_{1,2})$ is computed using Equation 4.22.

The calculation of the mutual capacitance is not as straightforward as that of the mutual inductance, because different from the mutual magnetic energy, the mutual electric energy is certainly not equal to the product of the mutual capacitance and the SSRRs' charges. The following algebraic derivation can explain why and can provide a final expression of the mutual capacitance.

From the circuit perspective, the total electric energy of the coupled two-SSRR system can be calculated through [133]:

$$W_e = \frac{q_1 V_1}{2} + \frac{q_2 V_2}{2} \tag{4.26}$$

where V_1 and V_2 are the voltages over the two SSRRs' self-capacitors C_1 and C_2, and q_1 and q_2 are the charges of the these two self-capacitors. q_1 and q_2 can be calculated through [133]:

$$q_1 = C_1 V_1 + C_m V_2 \tag{4.27a}$$

$$q_2 = C_m V_1 + C_2 V_2 \tag{4.27b}$$

Reorganizing these two equations, V_1 and V_2 can be expressed in terms of q_1 and q_2 as:

$$V_1 = \frac{C_2 q_1 - C_m q_2}{C_1 C_2 - C_m^2} \tag{4.28a}$$

$$V_2 = \frac{C_1 q_2 - C_m q_1}{C_1 C_2 - C_m^2} \tag{4.28b}$$

Substituting these two equations back into Equation 4.26, the total electric energy can be expressed purely in terms of charges as:

$$W_e = \frac{1}{2}\frac{C_2}{C_1C_2 - C_m^2}q_1^2 + \frac{1}{2}\frac{C_1}{C_1C_2 - C_m^2}q_2^2 - \frac{C_m}{C_1C_2 - C_m^2}q_1q_2 \tag{4.29}$$

In Equation 4.29, only the last term contains the charges of both the two self-capacitors, which simply implies:

$$W_{e,mut} = -\frac{C_m}{C_1C_2 - C_m^2}q_1q_2 \tag{4.30}$$

Comparing Equation 4.30 with Equation 4.25, the following relationship can be established:

$$\begin{aligned}\frac{C_m}{C_1C_2 - C_m^2} &= W_n = -\frac{W_{e,mut}}{q_1q_2} \\ &= -\frac{r_{eff}^2}{4\pi\epsilon_0}\int_{\vartheta_0}^{\vartheta'}\int_{\vartheta_0}^{\vartheta'}\frac{\rho_{1n}\left(\vartheta_1+\alpha_1\right)\rho_{2n}\left(\vartheta_2+\alpha_2\right)e^{-ik\delta\nu}}{\delta\nu}d\vartheta_1 d\vartheta_2\end{aligned} \tag{4.31}$$

where $\rho_{1n}\left(\vartheta_1+\alpha_1\right) = \rho_1\left(\vartheta_1+\alpha_1\right)/q_1$ and $\rho_{2n}\left(\vartheta_1+\alpha_1\right) = \rho_2\left(\vartheta_1+\alpha_1\right)/q_2$ are the normalized charge densities, and $\rho_1\left(\vartheta_1+\alpha_1\right)$ and $\rho_2\left(\vartheta_1+\alpha_1\right)$ can be calculated through Equation 4.22. For the SSRRs, the self-capacitors' charges q_1 and q_2 can be computed through:

$$\begin{aligned}q_1 &= \int_{\vartheta_0}^{\pi}\rho_1(\vartheta_1+\alpha_1)r_{eff}d\vartheta_1 \\ &= -(h+w)\frac{2\epsilon_0V_1}{\pi}\ln\left\{\sin\left[\frac{1}{2}\sin^{-1}\left(\frac{g}{2r_{eff}}\right)\right]\right\}\end{aligned} \tag{4.32a}$$

$$\begin{aligned}q_2 &= \int_{\vartheta_0}^{\pi}\rho_2(\vartheta_2+\alpha_2)r_{eff}d\vartheta_2 \\ &= -(h+w)\frac{2\epsilon_0V_2}{\pi}\ln\left\{\sin\left[\frac{1}{2}\sin^{-1}\left(\frac{g}{2r_{eff}}\right)\right]\right\}\end{aligned} \tag{4.32b}$$

So the expressions of $\rho_{1n}(\vartheta_1+\alpha_1)$ and $\rho_{2n}(\vartheta_1+\alpha_1)$ are:

$$\begin{aligned}\rho_{1n}(\vartheta_1+\alpha_1) &= \frac{\rho_1(\vartheta_1+\alpha_1)}{q_1} \\ &= -\frac{\cot\left(\frac{\vartheta_1}{2}\right)}{2r_{eff}}\ln\left\{\sin\left[\frac{1}{2}\sin^{-1}\left(\frac{g}{2r_{eff}}\right)\right]\right\}\end{aligned} \tag{4.33a}$$

$$\begin{aligned}\rho_{2n}(\vartheta_2+\alpha_2) &= \frac{\rho_2(\vartheta_2+\alpha_2)}{q_2} \\ &= -\frac{\cot\left(\frac{\vartheta_2}{2}\right)}{2r_{eff}}\ln\left\{\sin\left[\frac{1}{2}\sin^{-1}\left(\frac{g}{2r_{eff}}\right)\right]\right\}\end{aligned} \tag{4.33b}$$

With a known W_n, via solving the quadratic equation $C_m/(C_1C_2-C_m^2)=W_n$, the mutual capacitance is finally obtained as:

$$C_m = \frac{1-\sqrt{1+4C_1C_2W_n^2}}{-2W_n} \tag{4.34}$$

Another root of the quadratic equation is abandoned because it does not meet the limit condition ($C_m=0$, if $W_{e,mut}\to 0$).

4.3.3 The Circuit's Validity

Bringing the obtained L_m and C_m back into Subsection 4.3.1, now the currents, I_1 and I_2, of the two-SSRR parasitic array's equivalent circuit can be calculated. However before these values provided by the equivalent circuit are finally applied to analysing the two-SSRR array's radiation, it is definitely a good idea to first verify that the circuit is truly reliable for describing the array's current behaviors. The verification is implemented through examining the maximum currents on the coupled system's two SSRRs (I_1 and I_2), with the CST simulation data as references, for two randomly selected rotating configurations ($\alpha_1=15°$, $\alpha_2=185°$ and $\alpha_1=265°$, $\alpha_2=5°$) for two different separation distances ($d=4mm$ and $d=8mm$). I_1 and I_2 can be computed using Equation 4.12 with the source current I_0 set to be $1A$. The structures for the CST simulations are shown in Figure 4.11. The currents' magnitude and phase calculated based on the circuit analysis, along with the corresponding CST simulation data, are plotted in Figure 4.12$\sim$ 4.15. According to the good agreements shown in these figures, especially when the frequency is close to the single element's resonance frequency ($1.957GHz$), it can be naturally concluded that the equivalent circuit (Figure 4.9) is capable of describing the two SSRRs' maximum currents' behaviours for different configurations.

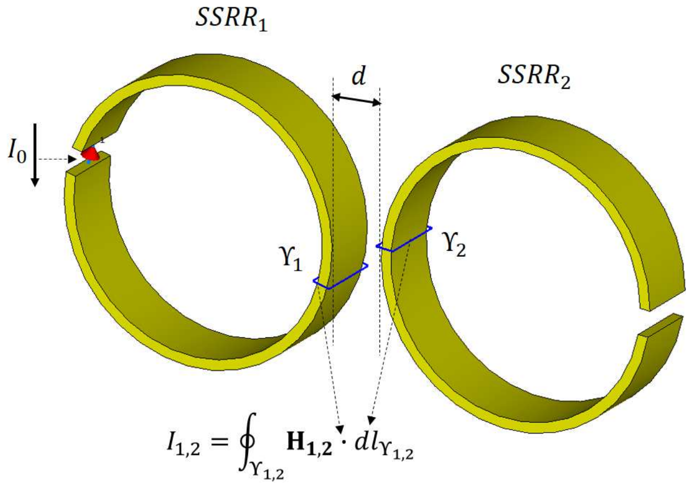

(a)

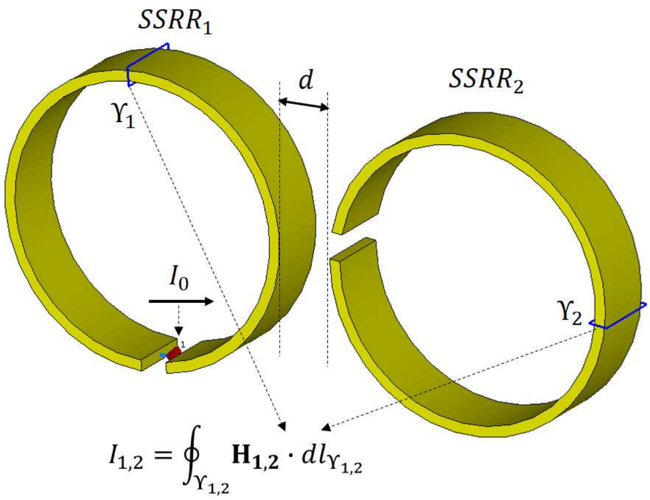

(b)

Figure 4.11: The perspective view of the structures of CST simulations to extract the maximum currents' data for: (a) $\alpha_1 = 15°$, $\alpha_2 = 185°$ and (b) $\alpha_1 = 265°$, $\alpha_2 = 5°$; Rectangular curves $\Upsilon_{1,2}$ are defined at each SSRR's maximum-current position, which allows the CST to automatically implement the Ampere's Law; d is the separation distance and it is set to be $4mm$ and $8mm$.

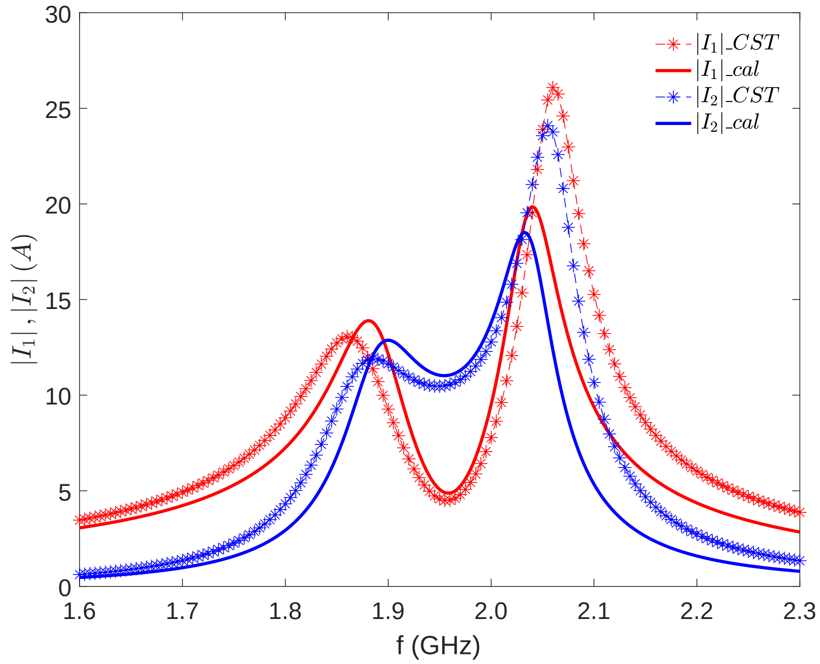

(a)

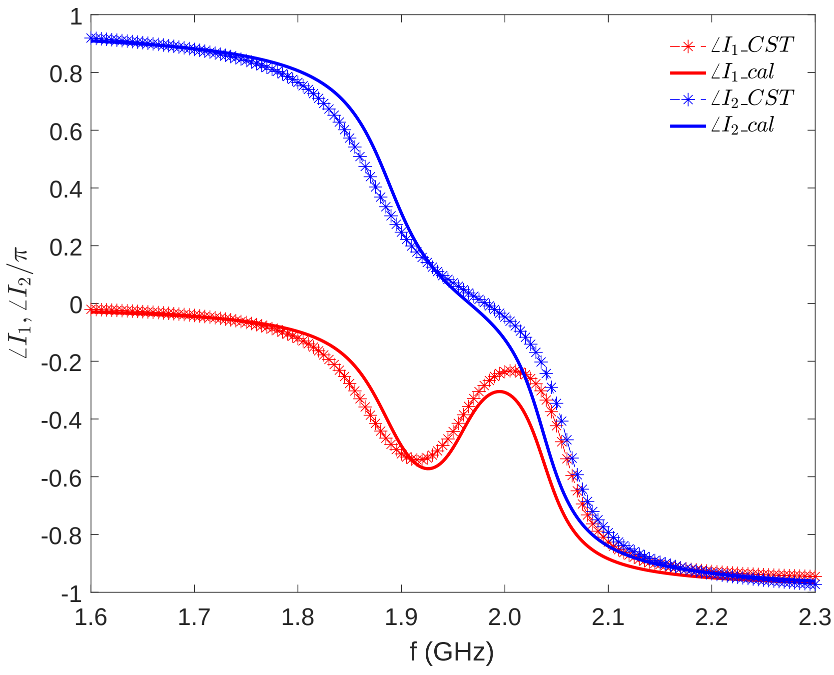

(b)

Figure 4.12: (a) The magnitude and (b) phase of the currents I_1 and I_2, the circuit calculated result (the solid lines) and CST simulated data (the star-dashed lines), for the rotating configuration: $\alpha_1 = 15°$, $\alpha_2 = 185°$, with a separation distance: $d = 4mm$.

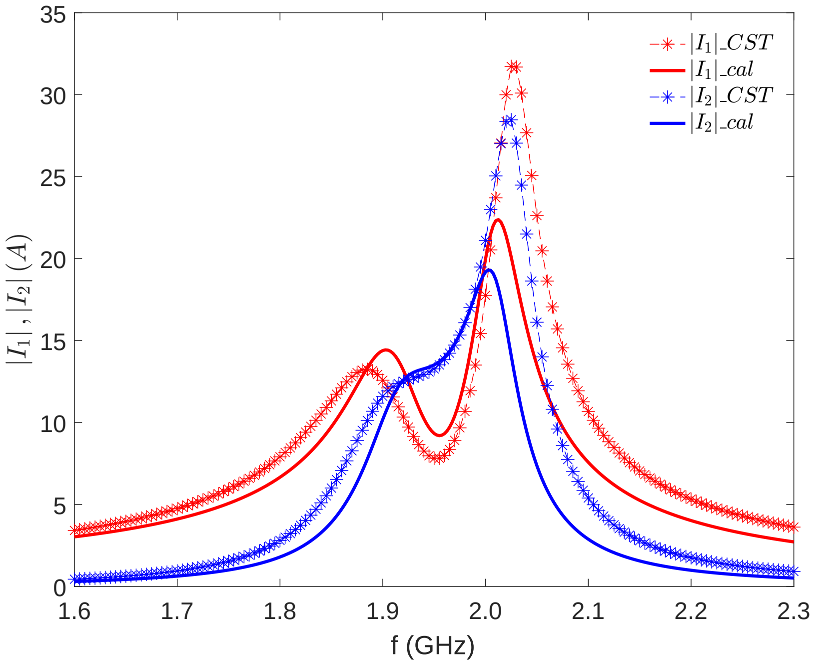

(a)

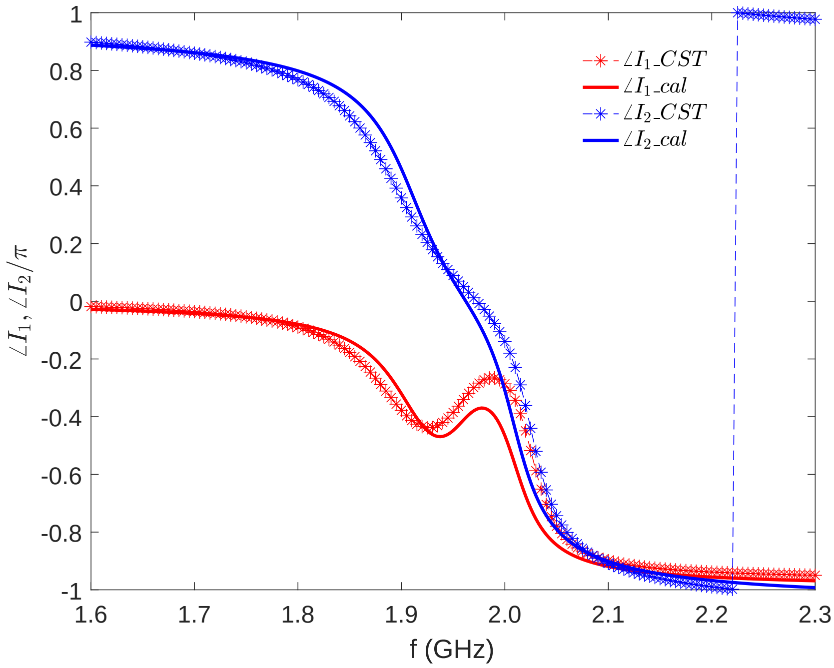

(b)

Figure 4.13: (a) The magnitude and (b) phase of the currents I_1 and I_2, the circuit calculated result (the solid lines) and CST simulated data (the star-dashed lines), for the rotating configuration: $\alpha_1 = 15°$, $\alpha_2 = 185°$, with a separation distance: $d = 8mm$.

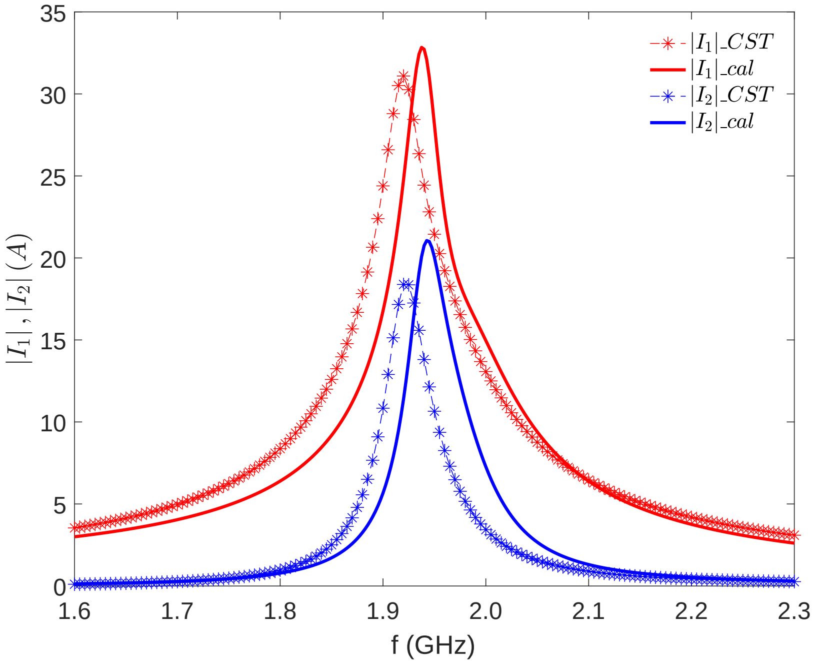

(a)

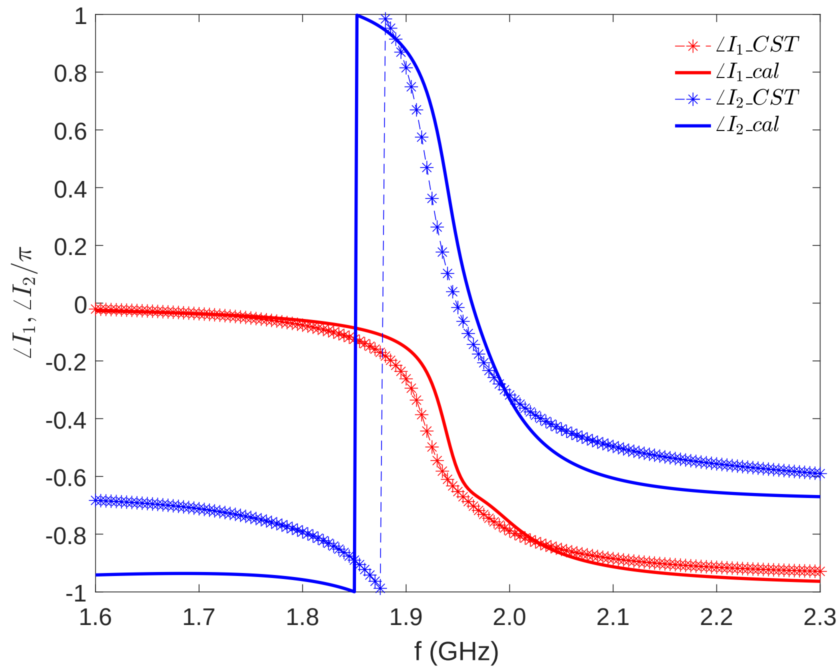

(b)

Figure 4.14: (a) The magnitude and (b) phase of the currents I_1 and I_2, the circuit calculated result (the solid lines) and CST simulated data (the star-dashed lines), for the rotating configuration: $\alpha_1 = 265°$, $\alpha_2 = 5°$, with a separation distance: $d = 4mm$.

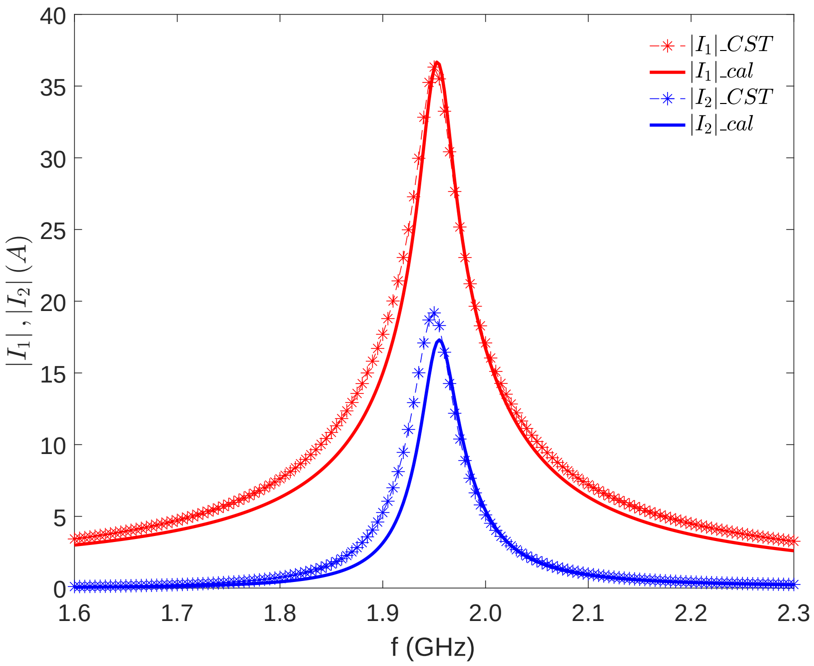

(a)

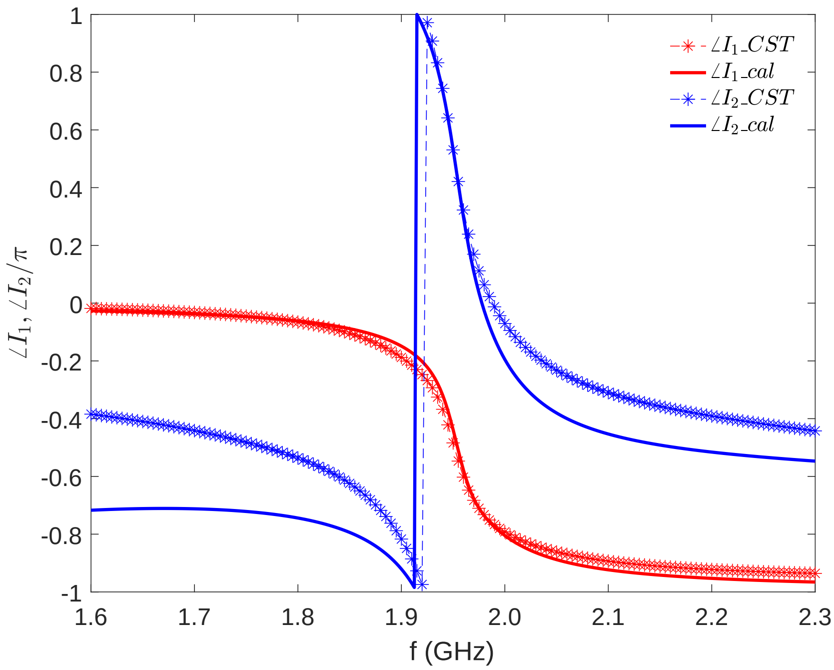

(b)

Figure 4.15: (a) The magnitude and (b) phase of the currents I_1 and I_2, the circuit calculated result (the solid lines) and CST simulated data (the star-dashed lines), for the rotating configuration: $\alpha_1 = 265°$, $\alpha_2 = 5°$, with a separation distance: $d = 8mm$.

4.4 Two-SSRR Parasitic Array: Superdirectivity

In this section, the parasitic array of two SSRRs is treated as a fully excited array of two NCLAs described in Section 3.5. Thus, the normalized far field average radiation energy density of such a two-SSRR array can be computed using Equation 3.32. The maximum currents I_1, I_2 are given by the circuit analysis demonstrated in Section 4.3. Another thing worth mentioning is that the elements' radius r in Equation 3.32 needs to be replaced by the SSRRs' effective radius r_{eff}.

With the ready-to-use model, which combines the equivalent circuit (Figure 4.9) and the Equation 3.32, the appropriate conditions for the two-SSRR parasitic array to achieve superdirectivity can be identified. In order to clearly identify the conditions, a directivity map of the endfire direction ($\theta = \pi/2$ and $\varphi = \pi$) is produced for all possible planar rotating configurations of the two-SSRR array. For simplifying the calculation, the separation distance is set to be a fixed value: $d = 4mm$, and the operational frequency is limited within a range of $1.7 \sim 2.0GHz$ considering the potential superdirectivity may possibly occur at a frequency slightly lower than the single SSRR element's resonance frequency.

The resultant directivity map is shown in Figure 4.17, respecting the structure shown in Figure 4.16. The red areas on the map (Figure 4.17) clearly imply that with a 'CC' structure shown in Figure 4.18, endfire superdirectivity (directivity≥ 4) can be achieved. The simulation result of directivity for this potential superdirective structure 'CC', within a frequency range of $1.6 \sim 2.3GHz$, is presented in Figure 4.19, which further confirms that this 'CC' structure is exactly a suitable structure for achieving endfire superdirectivity. More simulation results starting from this structure will be presented and explained in next chapter. The physical reason underlying the superdirectivity phenomenon created by this special structure will be discussed in Chapter 6.

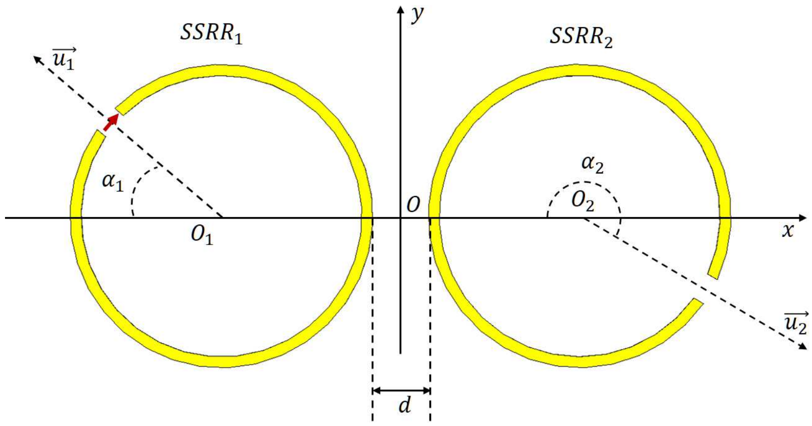

(a)

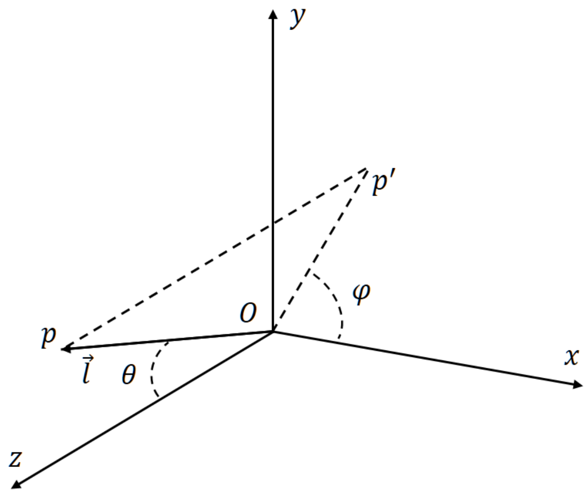

(b)

Figure 4.16: (a) The two-SSRR parasitic structure: the combinations of α_1 and α_2 indicate rotating configurations of the structure, here $d = 4mm$; and (b) its coordinate system.

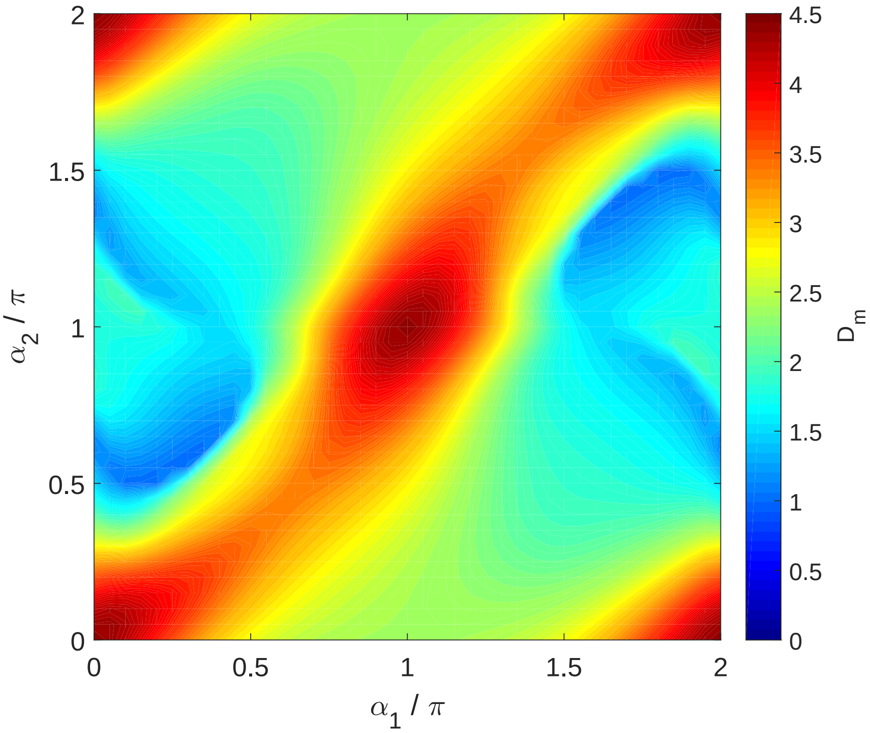

Figure 4.17: The endfire directivity map for all possible planar rotating configurations; D_m is the optimal maximum directivity for each configuration; here $d = 4mm$.

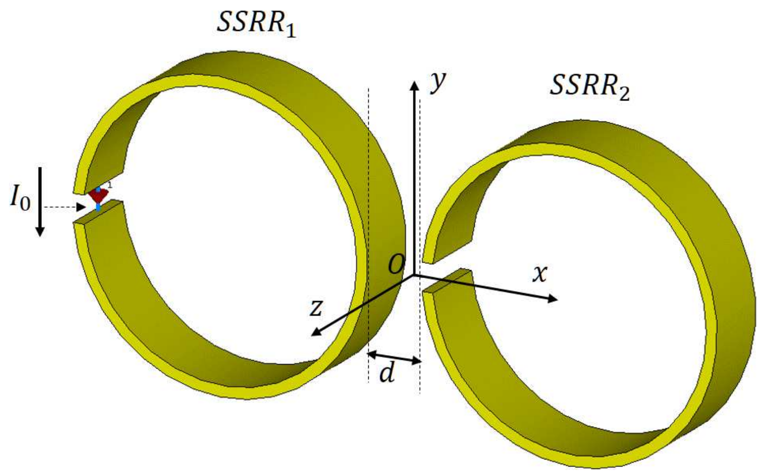

Figure 4.18: The potential superdirective 'CC' structure predicted by the analytical model, here $d = 4mm$.

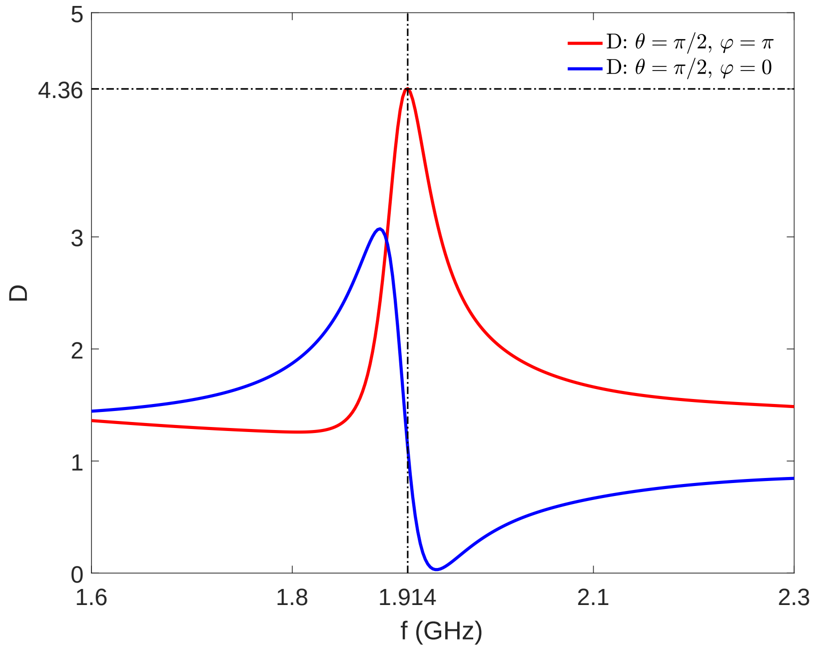

Figure 4.19: The simulation results of the endfire directivity values for the 'CC' structure, with $d = 4mm$.

Here it is also necessary to emphasize the importance of the powerful but compact analytical model finally formalized in this Chapter. The analytical model is important, not only because it has successfully predicted the 'CC' structure, also it has provided a new possibility of designing parasitic superdirective arrays. Successfully building and utilizing the model implies that it is actually possible to first build a compact model to predict potential outcomes before starting simulations and experiments, which can significantly reduce the design time. Both the conventional design process without an analytical model and our design process with such an analytical model can be demonstrated in Figure 4.20.

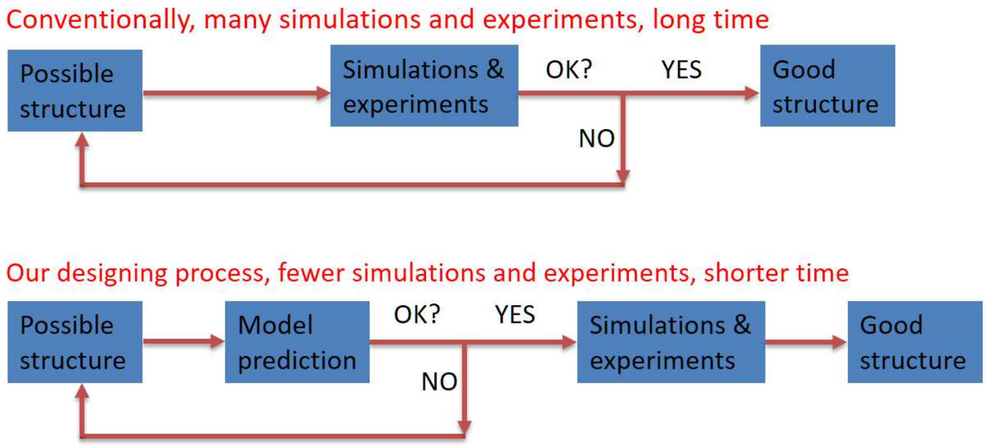

Figure 4.20: The conventional design process and our design process.

4.5 Conclusion

First an equivalent circuit, with its electrical components (L, C and R) determined through numerical simulations, is proved to be able to describe a single SSRR's impedance and current behaviours. Then based on the single SSRR's equivalent circuit, a new equivalent circuit for a two-SSRR parasitic array is introduced, which leads to the recognition of the two coupled SSRRs' maximum currents, key required values to calculate the array's radiated energy. Then combining this equivalent circuit and the method of calculating a two-NCLA array's radiated energy (introduced in Section 3.5) forms a powerful analytical model, which allows to easily but accurately predict the far field radiation behaviours of an electrically small parasitic array of two SSRRs (the two SSRRs are not necessarily standard and identical), based on certain information of the array, namely the SSRRs' dimensions, the SSRRs' electrical components (L, C and R), the SSRRs' rotating orientation angles (α_1 and α_2), the two SSRRs's separation (d) and the array's operation frequency. Then a directivity map for such a two-SSRR parasitic array is produced and the right superdirective structure (the 'CC' structure comprised of two standard SSRRs with $d = 4mm$ working at $1.914GHz$, achieving an endfire directivity of 4.36) is successfully predicted. Relevant simulation results for this 'CC' structure and its improved versions will be presented in next chapter. In the end, based on a short discussion, it is concluded that it is possible to first build a compact analytical model to predict the potential outcomes, for the design process of a parasitic superdirective array, before starting simulations and experiments, which can significantly reduce the design time.

Chapter 5

Superdirective Structures

In this chapter, superdirective structures (the model predicted 'CC' structure and its improved versions) are studied based on simulation results. First, the model predicted 'CC' structure is verified with simulation results and the design principle behind the superdirective structures in this thesis is discussed. Then, the characteristics of antenna performance (the maximum directivity, the optimal frequency, the superdirectivity bandwidth, the efficiency, the beamwidth and the Q factor) for the superdirective structures are investigated for different elements' separations. Next, with the optimal separation distances identified for all the superdirective structures' best directive performances, the corresponding characteristics of antenna performance are summarized and presented as tables. In the end, a comparison, concerning the directive performance, between these superdirective structures and two commercial two-element Yagi antenna is made.

The main new contributions in this Chapter include: 1. A verification of the model predicted 'CC' superdirective structure; 2. A new design principle for superdirective structures; 3. A thorough study of the antenna performance characteristics for the 'CC' and improved superdirective structures.

5.1 The 'CC' Structure

The analytical model predicts that a 'CC' structure ($\alpha_1 = 0$ and $\alpha_2 = 0$) can achieve superdirectivity for $d = 4mm$ at specific frequencies. This has already been confirmed by Figure 4.19. According to the directivity curve shown in Figure 3.10(a), for an array of two CLAs, the maximum directivity will certainly increase when the separation distance between the two elements decreases. In order to examine if the same trend exists for this 'CC' structure (Figure 5.1), a CST simulation is first performed for a smaller distance, $d = 1mm$. The resultant endfire directivity curves ($\theta = \pi/2$ and $\varphi = 0\&\pi$) are shown in Figure 5.2.

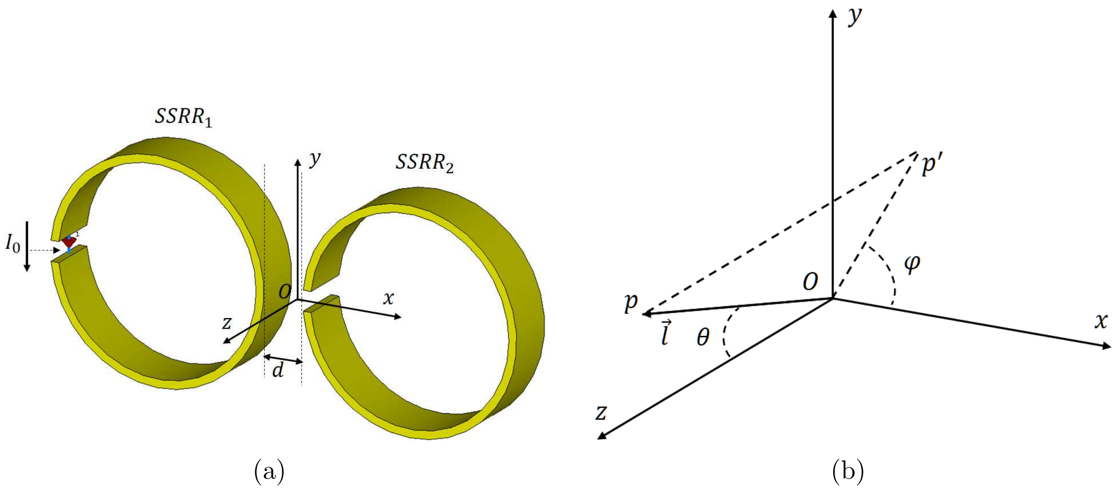

Figure 5.1: (a) The 'CC' structure and (b) its coordinate system.

Superdirectivity indeed occurs in the expected direction ($\theta = \pi/2, \varphi = \pi$). However, the maximum directivity here is apparently smaller than the that (4.36) of the directivity curve, shown in Figure 4.19, for the case of $d = 4mm$, which contradicts the two-CLA array's directivity changing trend. To further confirm that the trend does not apply here, another two sets of simulations are implemented with d set to be $0.6mm$ and $0.2mm$. The resultant endfire directivity curves are displayed in Figure 5.3.

Based on Figure 5.3, along with Figure 5.2, it seems if the separation distance is

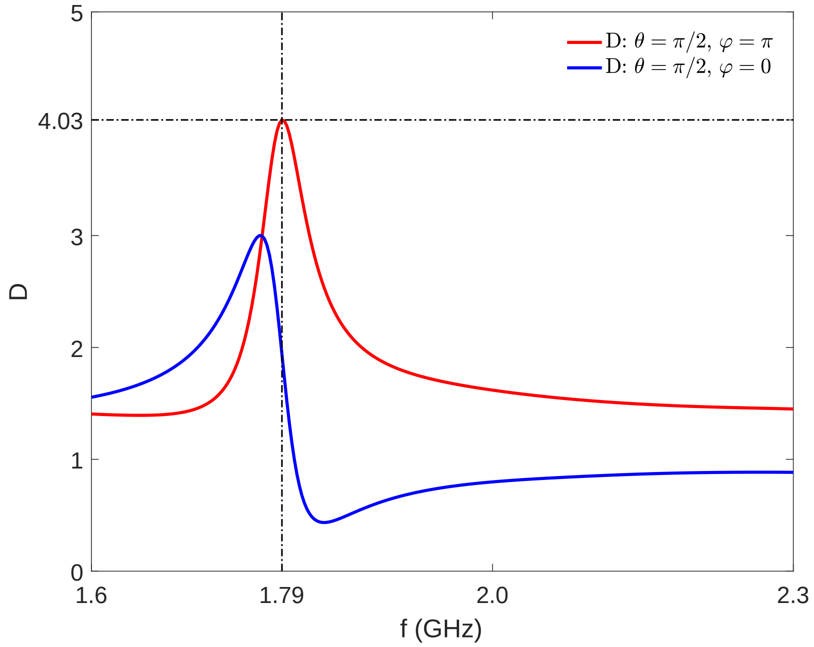

Figure 5.2: The endfire directivity curves for the 'CC' structure when $d = 1mm$.

too small, when it further decreases, the 'CC' structure's maximum directivity will decrease rather than increase. The reason why this happens is believed to be that for this 'CC' structure with only one element excited, a proper phase difference of the two elements' currents cannot always be guaranteed for each separation distance chosen, as it is for a two-CLA array with both the two elements excited separately.

In addition, for this 'CC' structure, an optimal separation distance should be located somewhere larger than $1mm$, if it exists. For the purpose of identifying the optimal separation, simulations are run with d set to be $1 \sim 10mm$, and the obtained superdirective directivity values and their corresponding optimal frequencies are plotted against the changing separation distance and presented in Figure 5.4. According to this figure, the optimal separation distance is $4mm$, with which the maximum superdirective directivity of 4.36 is achieved at an optimal frequency of $1.914GHz$. The optimal frequency is increasing along with the separation distance while always keeps lower than the single SSRR element's resonance frequency.

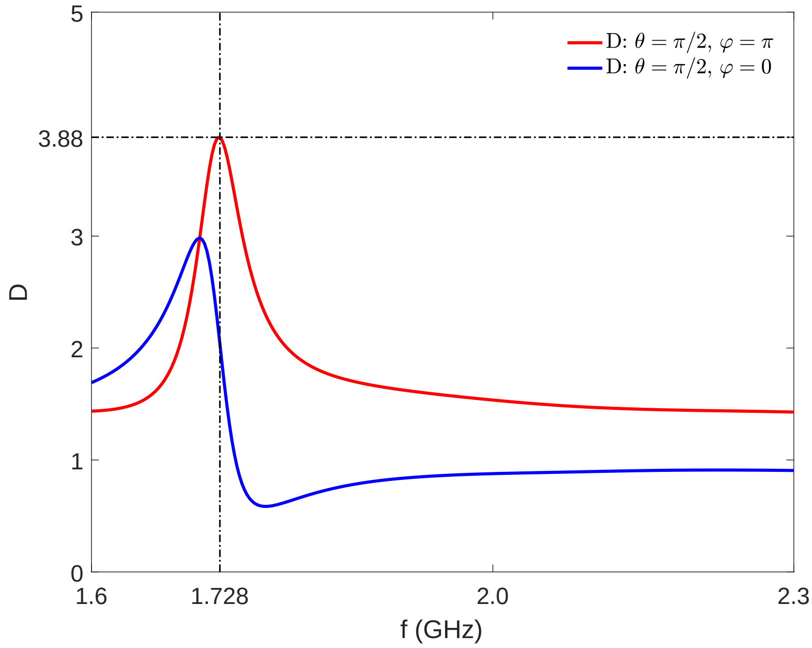

(a)

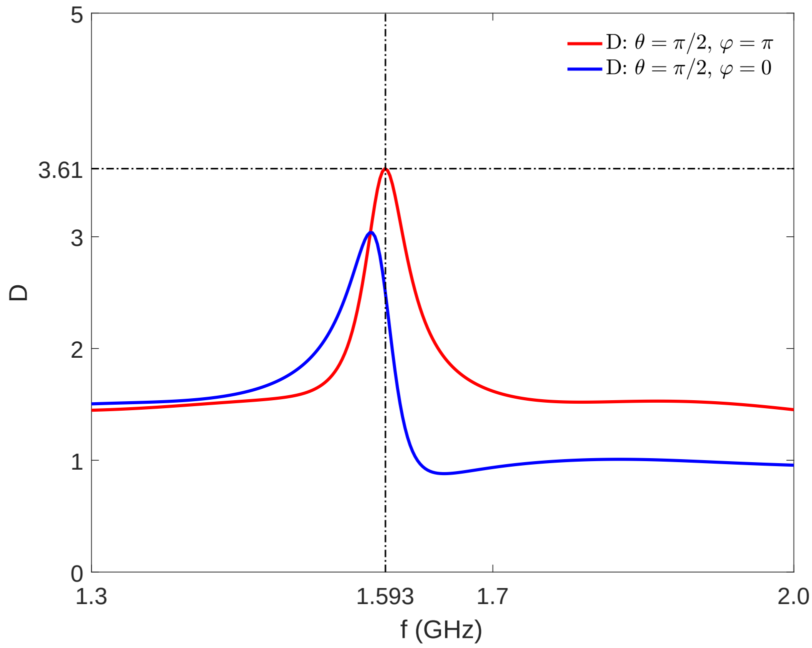

(b)

Figure 5.3: The endfire directivity curves for the 'CC' structure when (a) $d = 0.6mm$ and (b) $d = 0.2mm$.

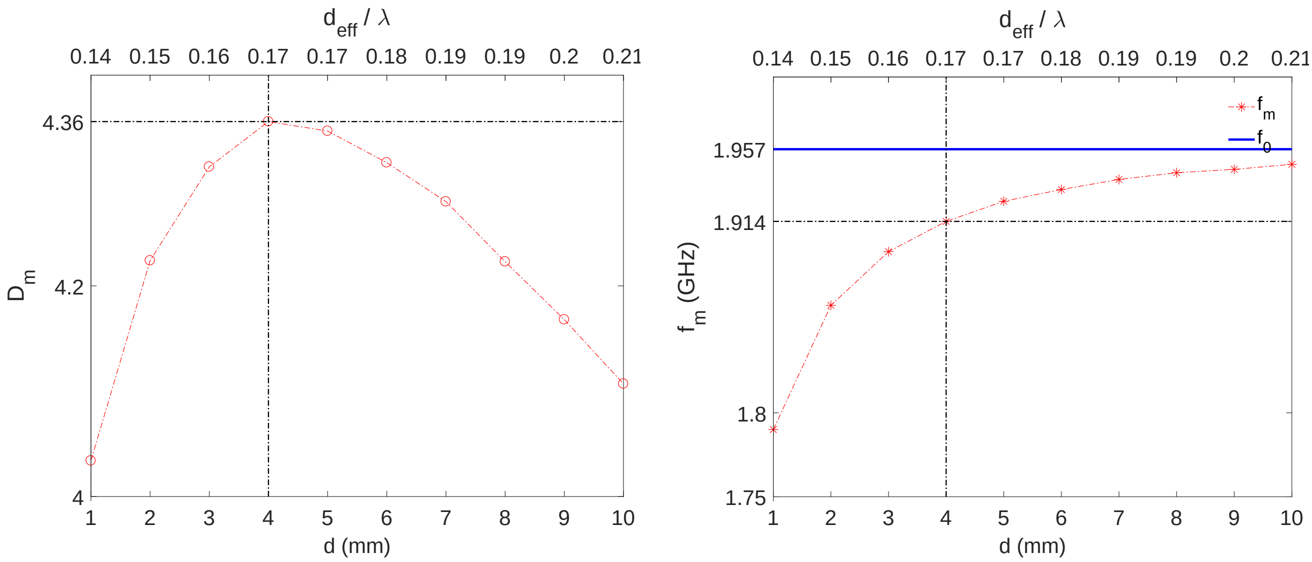

(a) (b)

Figure 5.4: (a) The maximum directivity values, in the direction of $\theta = \pi/2, \varphi = \pi$, and (b) their corresponding optimal frequencies, f_0 is the common resonance frequency of the two identical SSRR elements; the effective separation distance $d_{eff} = 2r + d$, where r is the common radius of the two identical SSRRs, λ is the operational wavelength.

Other important characteristics of antenna performance obtained from CST simulations are plotted and shown in Figure 5.5. In Figure 5.5(a), the square-dashed-line shows a newly introduced parameter, superdirectivity bandwidth. For an electrically small two-element superdirective antenna, it is defined as the frequency range, in which the antenna's directivity is above the threshold value of 4, divided by the optimal frequency corresponding to the antenna's maximum directivity. For the 'CC' structure, the superdirectivity bandwidth follows a same trend as the maximum directivity does when the separation distance increases. Figure 5.5(b) shows the antenna's efficiency grows with the increasing separation distance, which mainly results from the reduction of the ohmic loss due to the weakening of the mutual coupling. The different trends shown by the efficiency and the maximum directivity also remind us of another fact: a larger directivity does not necessarily lead to a higher gain. Figure 5.5(c) indicates the radiation beam will get broader for a larger separation distance, which can degrade the structure's directive performance. In Figure 5.5(d), a decreasing Q-factor curve suggests that for a larger separation distance, more stored energy, surrounding the antenna, will be released and transformed into radiated energy. Clearly the optimal separation $d = 4mm$ is identified for the structure's best directive performance and best bandwidth performance, but if for certain reasons the structure needs to be used for specific applications more featuring the efficiency or the Q factor, the Figure 5.5(b) and 5.5(d) can provide useful reference information.

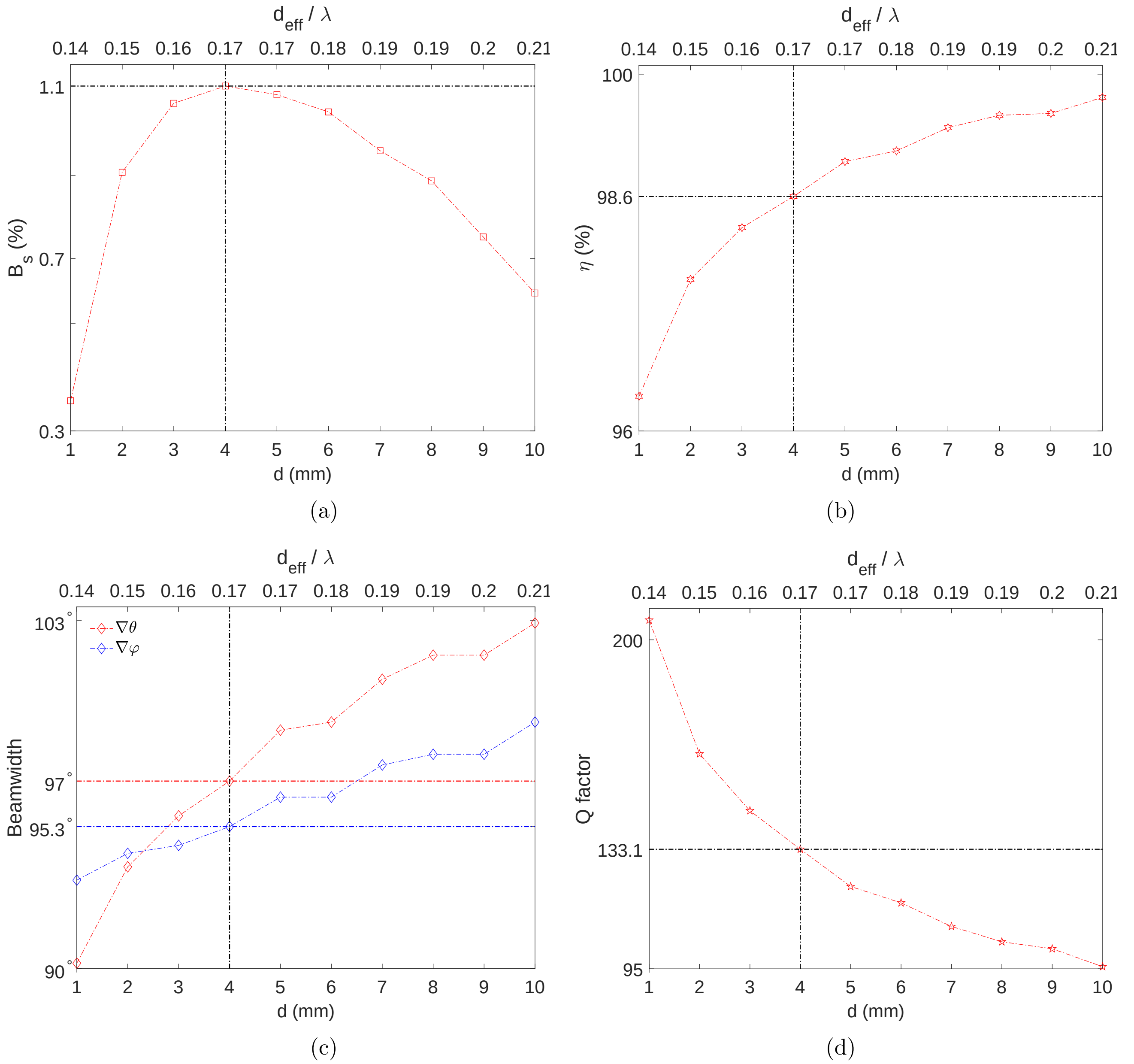

Figure 5.5: (a) The superdirectivity bandwidth, (b) the radiation efficiency, (c) the angular beamwidth and (d) the Q factor corresponding to the maximum directivity.

The design principle behind this 'CC' structure is different from that behind other common directive antennas. For example, for a Yagi-Uda antenna, the very basic design idea is to try to get as much as possible constructive interference of the fields radiated by all the elements in one endfire direction (the endfire direction pointing to the directors from the reflector) [134]. While for this 'CC' structure, the very basic design principle is to try to achieve the least destructive interference of the fields radiated by the two elements in the expected endfire direction. For the 'CC' structure with a separation distance $d = 4mm$, the magnitude and phase of the currents carried by the two SSRRs are plotted against frequency and shown in Figure 5.6. It can be clearly seen that when the maximum directivity is achieved at the frequency of $1.914GHz$ (see Figure 4.19), the currents carried by the two SSRRs have an almost same magnitude and a near-π phase difference. Because the effective separation distance between the two elements is very small (0.17λ, see Figure 5.4), according to the pattern multiplication rule, the radiated fields from the two elements cancel out in all directions except the two endfire directions. The small effective separation distance makes the effective phase difference ($kd_{eff} \sin\theta \cos\varphi + \beta$) in one endfire direction ($\theta = \pi/2, \varphi = \pi$) further away from π while makes the effective phase difference in the other endfire direction ($\theta = \pi/2, \varphi = 0$) even closer to π, which leads to the occurrence of superdirectivity in the expected endfire direction ($\theta = \pi/2, \varphi = \pi$) with the least destructive interference of the two elements' radiated fields. In order to show that the structures based on this new design principle can achieve better directive performances compared to the structures based on the Yagi-Uda design principle, at the end of this Chapter a comparison is between our superdirective structures and two commercial two-element Yagi antennas is presented.

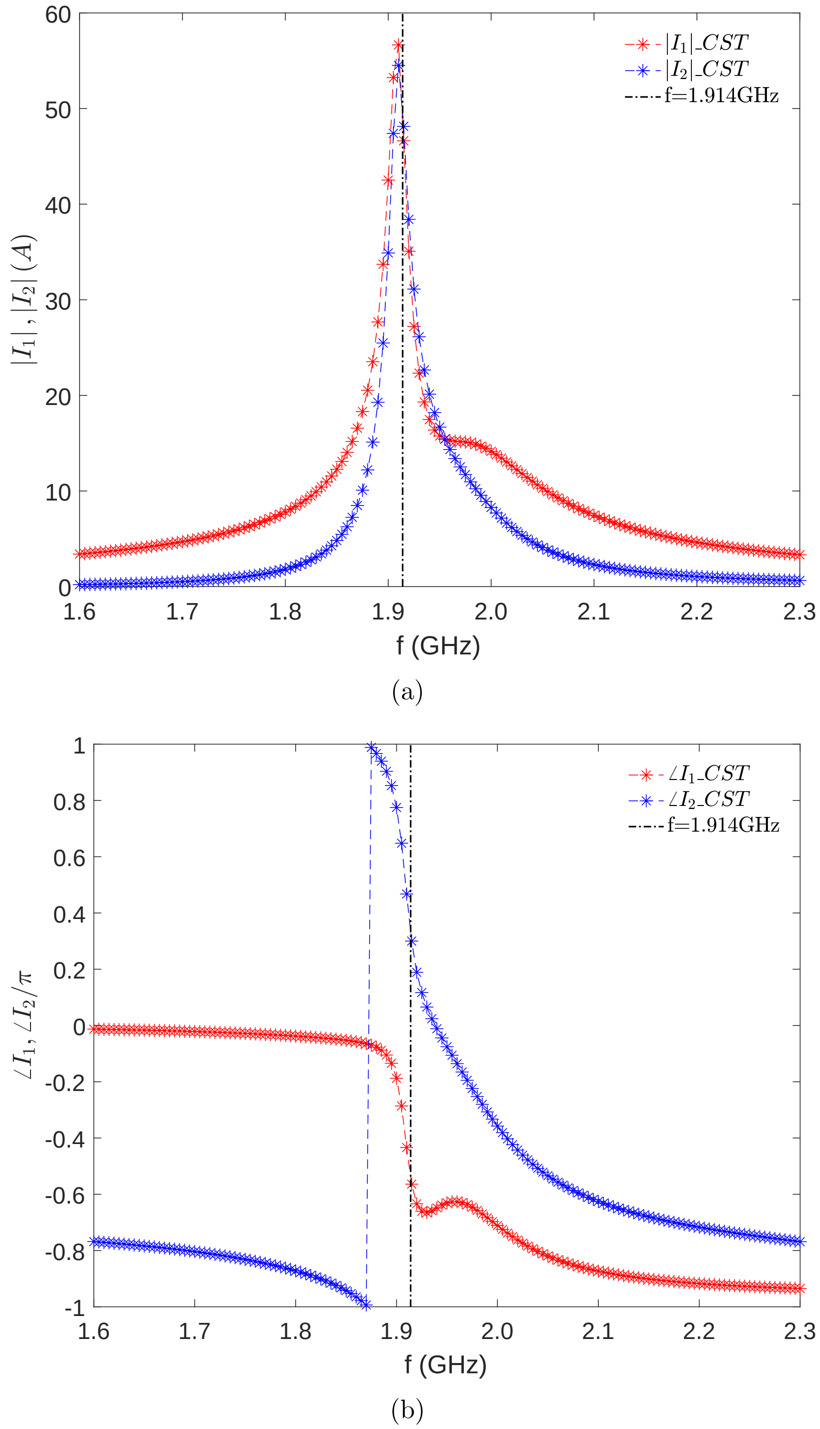

Figure 5.6: (a) The magnitude and (b) the phase of the currents carried by the two SSRRs of the 'CC' structure with a separation distance $d = 4mm$; Here the plots are produced based on CST simulation data.

5.2 Improved Superdirective Structures

In this section, improved superdirective structures, obtained through applying specific detuning changes to the original 'CC' structure, are studied. Among them, four structures, namely the 'CCEx' structure, the 'CCDg' structure, the 'CCDgEx' structure and the 'CCLr' structure, are thoroughly analysed and their characteristics of antenna performance against different d values are presented. The very basic design principle behind these improved structures is to reduce the operation frequency of the original 'CC' structure which can be accomplished through reducing the resonant frequency of the passive element.

5.2.1 The 'CCEx' Structure

First, through exchanging the locations of the active element (the excited element) and the passive element (the shorted parasitic element) respecting the original 'CC' structure in Figure 5.1, the 'CCEx' structure, shown in Figure 5.7, is introduced. The maximum endfire directivity D_m (in the direction of $\theta = \pi/2, \varphi = 0$), the optimal frequency f_m, the superdirectivity bandwidth B_s, the radiation efficiency η, the beam width $\triangledown\theta\&\triangledown\varphi$ and the Q-factor for different separation distances ($d = 1 \sim 10mm$) are displayed in Figure 5.8$\sim$5.9.

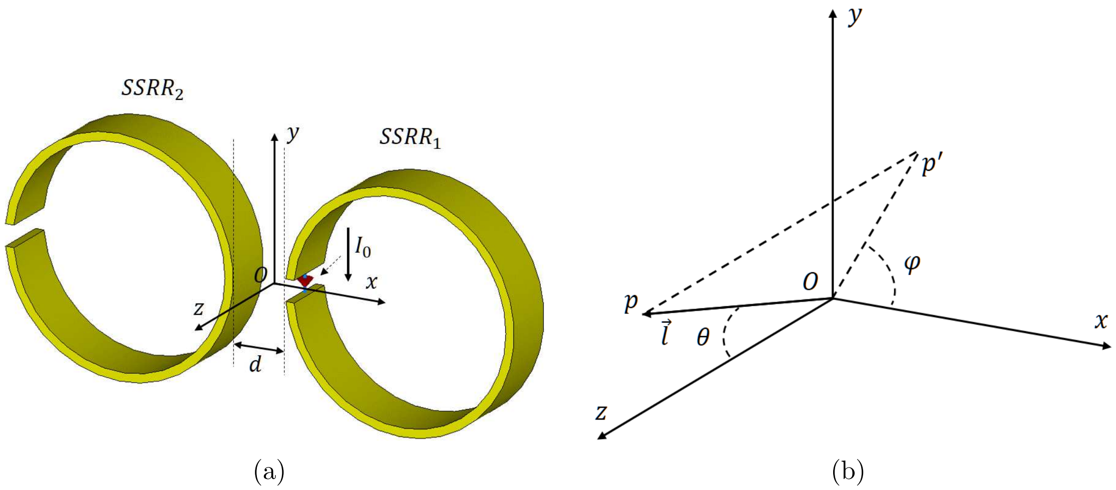

Figure 5.7: (a) The 'CCEx' structure and (b) its coordinate system.

Because no change is made upon the two identical SSRR elements, the exchange of their positions can also be treated as the reallocation of the excitation source (form the first element to the second one). This source reallocation, which creates a near π shift of the phase difference between the currents carried by the two elements, finally causes the reverse of the direction in which superdirectivity occurs.

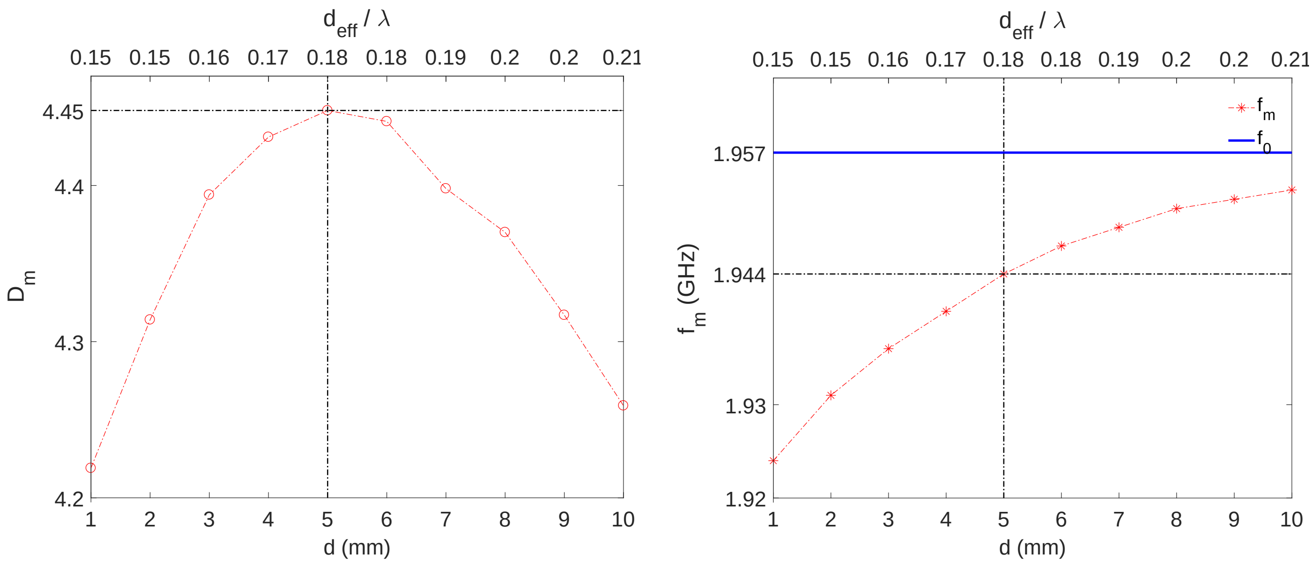

Figure 5.8: (a) The maximum directivity values, in the direction of $\theta = \pi/2, \varphi = 0$, and (b) their corresponding optimal frequencies, f_0 is the common resonance frequency of the two identical SSRR elements; the effective separation distance $d_{eff} = 2r + d$, where r is the common radius of the two identical SSRRs, λ is the operational wavelength.

Comparing Figure 5.8(a) and Figure 5.4(a), the improvement in the overall directive performance of the 'CCEx' structure over the 'CC' is not very remarkable, however, it is still noticeable that for a small separation distance ($d < 5mm$) the improvement is slightly more significant than that for a large separation. This suggests that when the separation is too small, the SSRRs' gaps can cause peculiar effect on the mutual coupling between the two SSRRs. The optimal frequencies (Figure 5.8(b)) here against different separations are always closer to the single SSRR's resonance frequency compared with those in Figure 5.4(b) for the 'CC' structure, which implies that more energy can radiate from either of the two SSRRs of the 'CCEx', leading to a higher efficiency (Figure 5.9(b)) and a lower Q factor (Figure 5.9(d)) for the 'CCEx' structure.

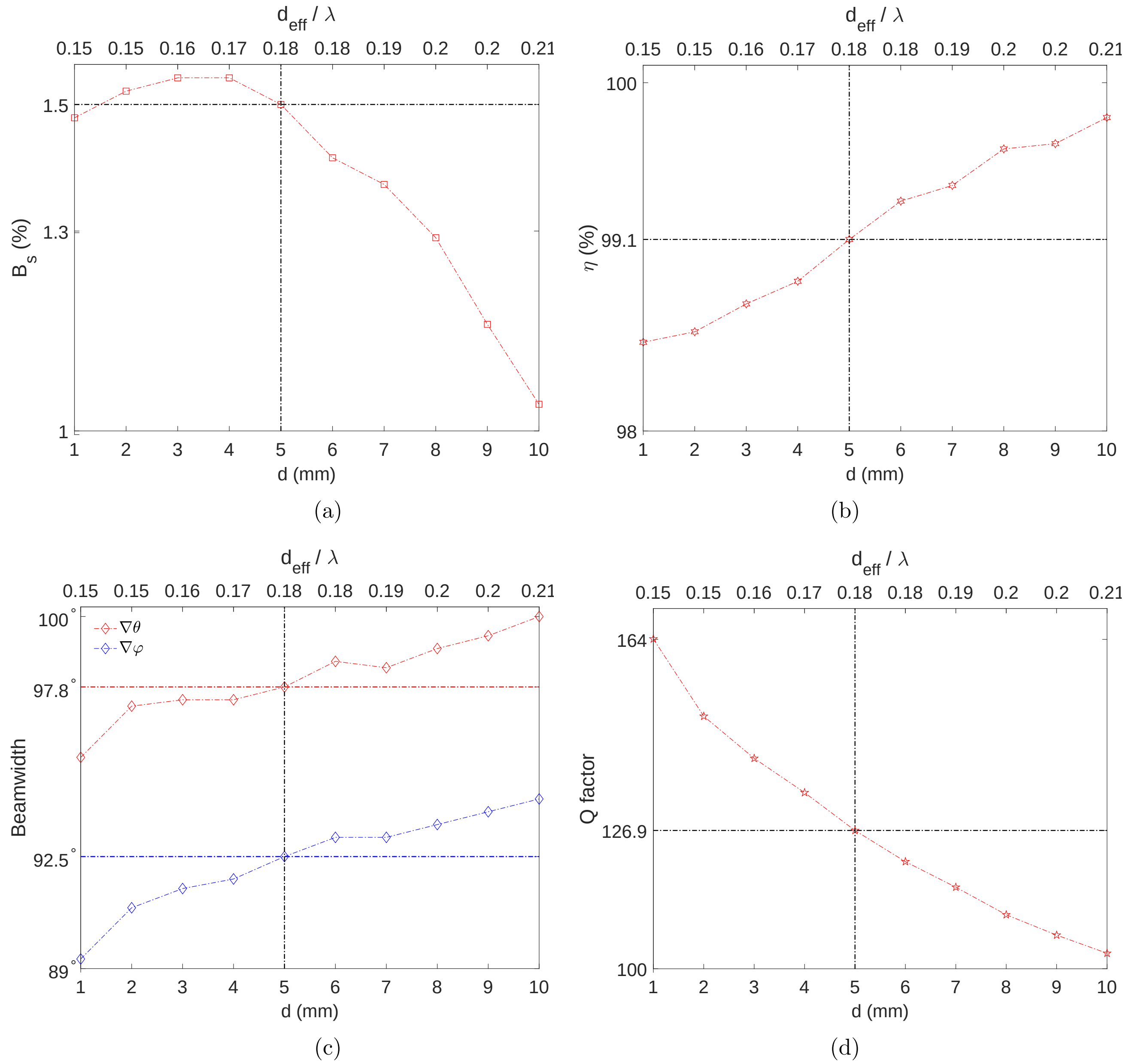

Figure 5.9: (a) The superdirectivity bandwidth, (b) the radiation efficiency, (c) the angular beamwidth and (d) the Q factor corresponding to the maximum directivity.

Considering the changing trends of other antenna performance characteristics of this 'CCEx' structure, compared with those of the 'CC', only for the superdirectivity bandwidth (Figure 5.9(a)) there shows a difference that the separation for the best bandwidth performance is not the same one for the structure's best directive performance.

5.2.2 The 'CCDg' Structure

By filling the passive element's gap of the 'CC' with dielectric material, namely alumina, a new alternative superdirective structure, the 'CCDg' is now created and shown in Figure 5.10. This new structure's antenna performance characteristics (D_m, f_m, B_s, η, beamwidth and Q-factor) for different d values are shown in Figure 5.11~5.12.

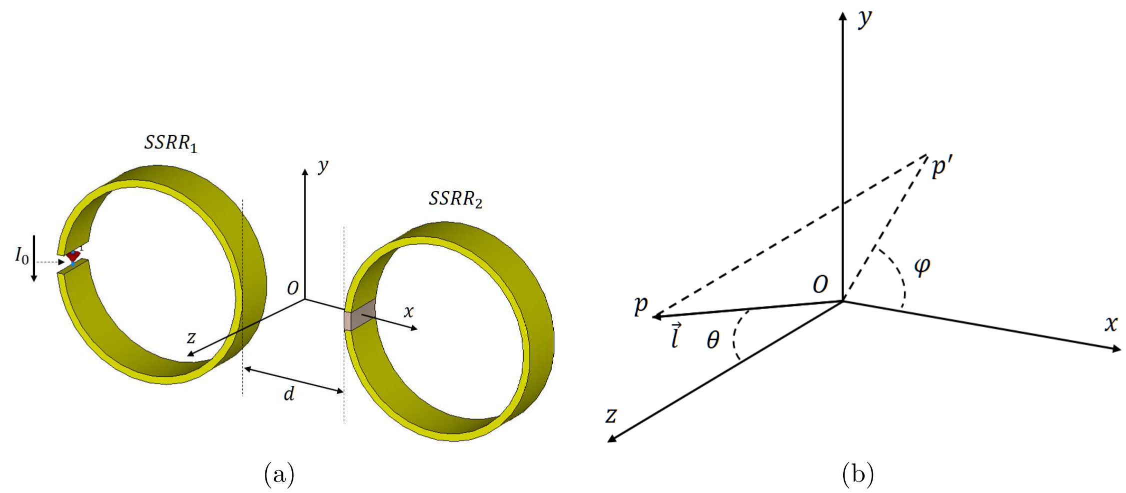

Figure 5.10: (a) The 'CCDg' structure and (b) its coordinate system.

Here this 'CCDg' structure shows a noticeable improvement in the best directive performance over the 'CC' while at the cost of an increase in the absolute separation(12mm,see Figure 5.11(a)). However, the effective separations in terms of the corresponding operation wavelength, for both of the two structures' best directive performance, are exactly the same (0.17). This truth reveals that filling the passive element's gap with alumina actually reduces the optimal operation frequency of the whole structure through reducing the resonant frequency of the passive element (Figure 5.11(b)). It also implies that the optimal operation frequency of such a two-SSRR structure is strongly related to the resonant frequency of the structure's passive element, which is further confirmed by the study of the 'CCLr' structure (Section 5.2.4).

For this 'CCDg', its superdirectivity bandwidth is slightly decreasing as the separation increases. All other three parameters (the efficiency, the beamwidth and the Q factor) follow the same changing trends, when the separation increases, as those of the 'CC' follow. Compared with the case for the 'CC', due to the gap filling, the efficiency for the best directive performance has decreased; Corresponding to the increased absolute separation, the Q factor for the best directive performance has increased.

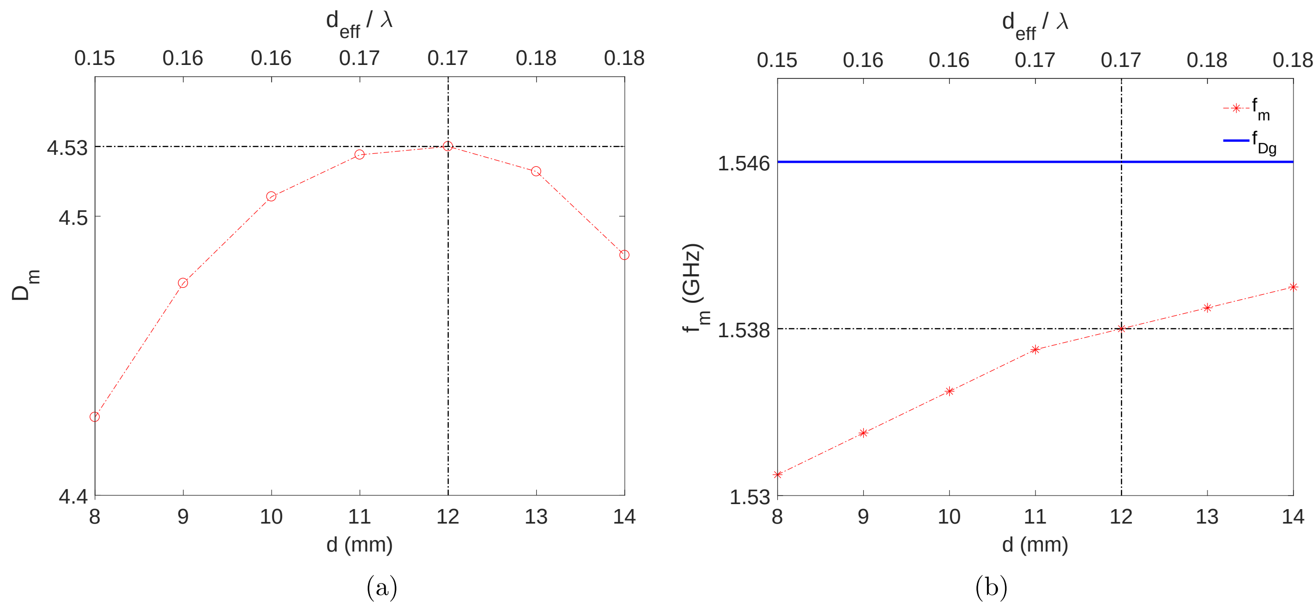

Figure 5.11: (a) The maximum directivity values, in the direction of $\theta = \pi/2, \varphi = \pi$, and (b) their corresponding optimal frequencies, f_{Dg} is the resonance frequency of the dielectrically gap filling SSRR element; the effective separation distance $d_{eff} = 2r + d$, where r is the common radius of the two SSRRs, λ is the operational wavelength.

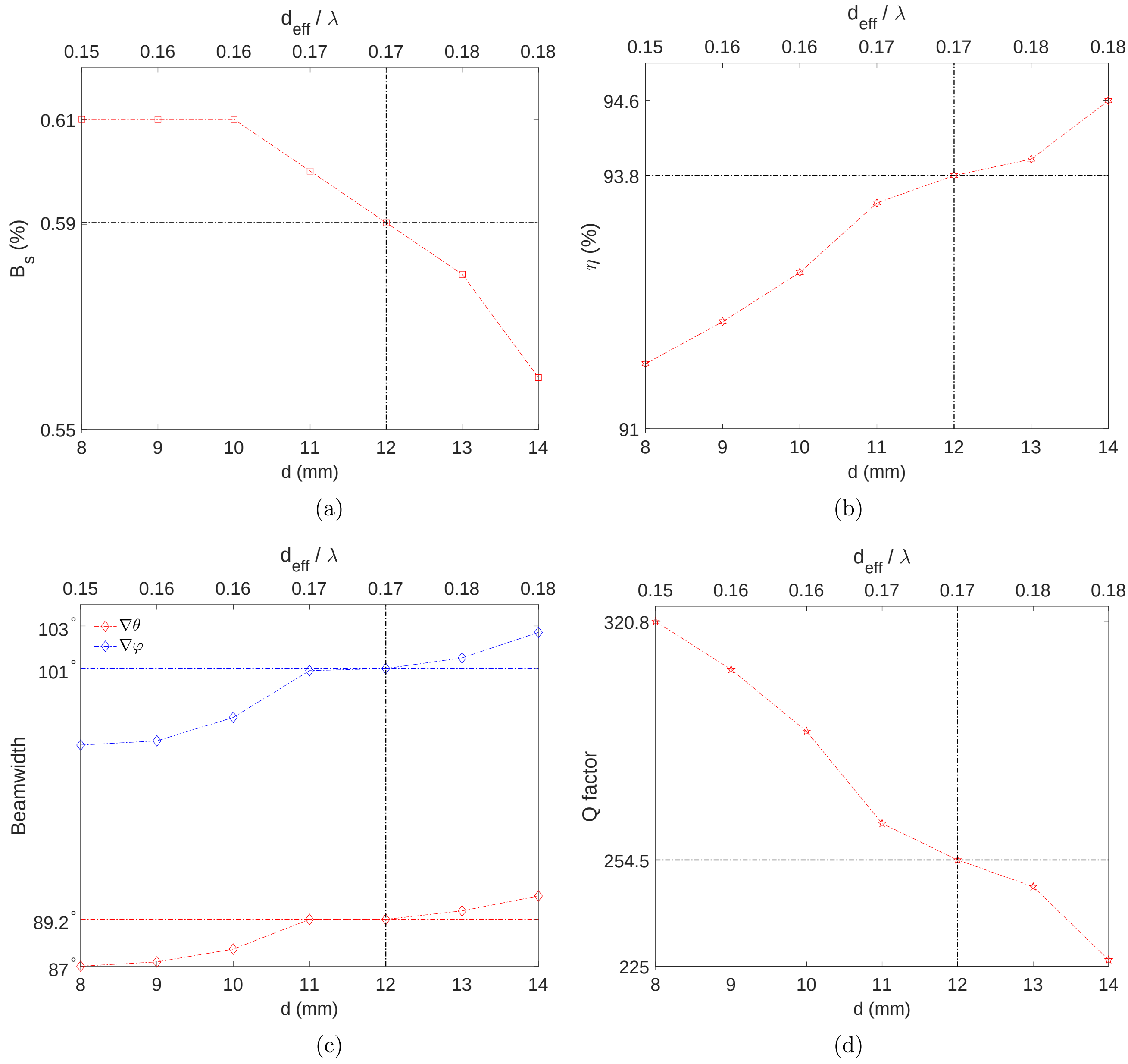

Figure 5.12: (a) The superdirectivity bandwidth, (b) the radiation efficiency, (c) the angular beamwidth and (d) the Q factor corresponding to the maximum directivity.

5.2.3 The 'CCDgEx' Structure

For the 'CCDg' structure, the locations of its two elements can also be exchanged. Then a new structure, 'CCDgEx', is now displayed in Figure 5.13. This new structure's antenna performance characteristics are shown in Figure 5.14∼5.15.

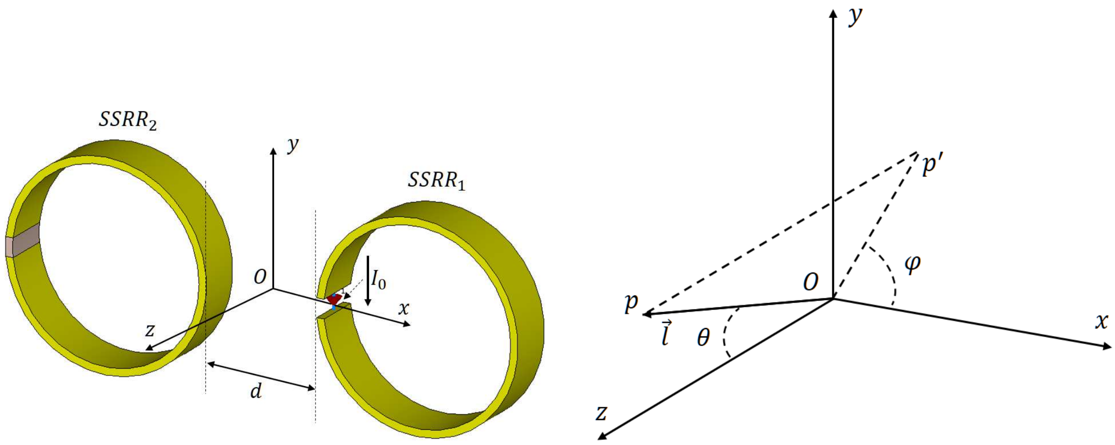

(a) (b)

Figure 5.13: (a) The 'CCDgEx' structure and (b) its coordinate system.

Compared with the case for the 'CCDg', here neither the absolute values of the antenna performance characteristics nor the changing trends of these characteristics, against the increasing separation, show significant differences, except that the overall superdirectivity bandwidth performance of this 'CCDgEx' structure is slightly better. Therefore, combining the 'CCDg' and the 'CCDgEx' structure creates a possibility to achieve superdirectivity alternately in two opposite directions ,while keep all other performances almost unaffected, just through moving the excitation source, which might be useful for certain application designs requiring stable alternating bidirectional superdirective radiation.

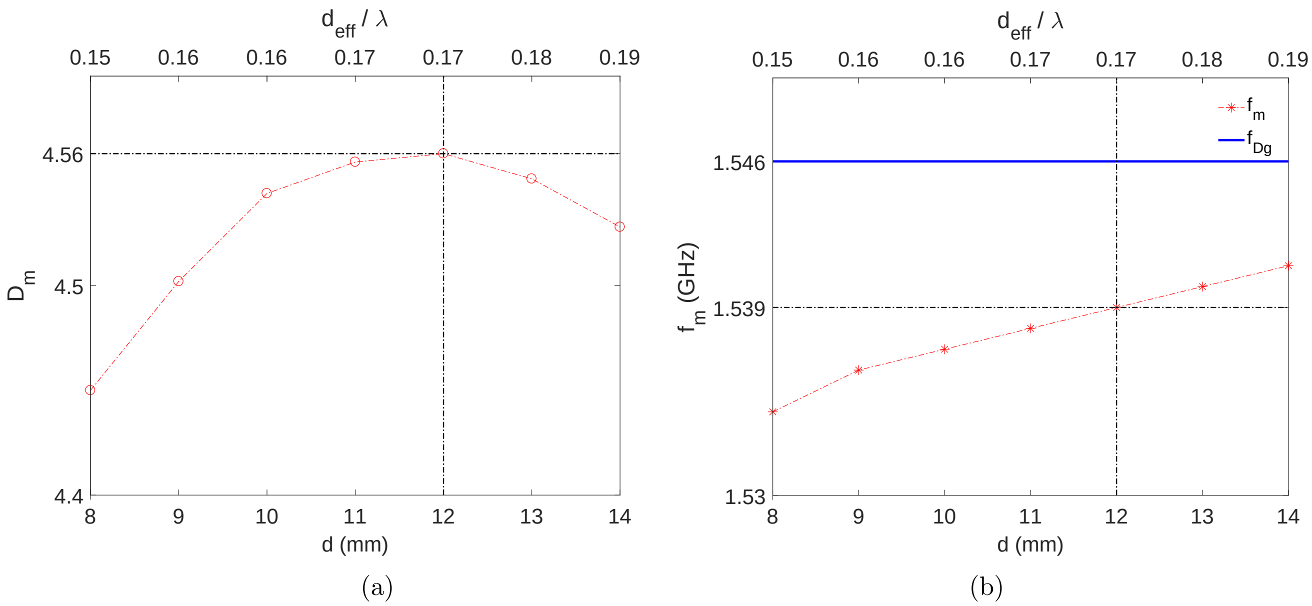

Figure 5.14: (a) The maximum directivity values, in the direction of $\theta = \pi/2, \varphi = 0$, and (b) their corresponding optimal frequencies, f_{Dg} is the resonance frequency of the dielectrically gap filling SSRR element; the effective separation distance $d_{eff} = 2r + d$, where r is the common radius of the two SSRRs, λ is the operational wavelength.

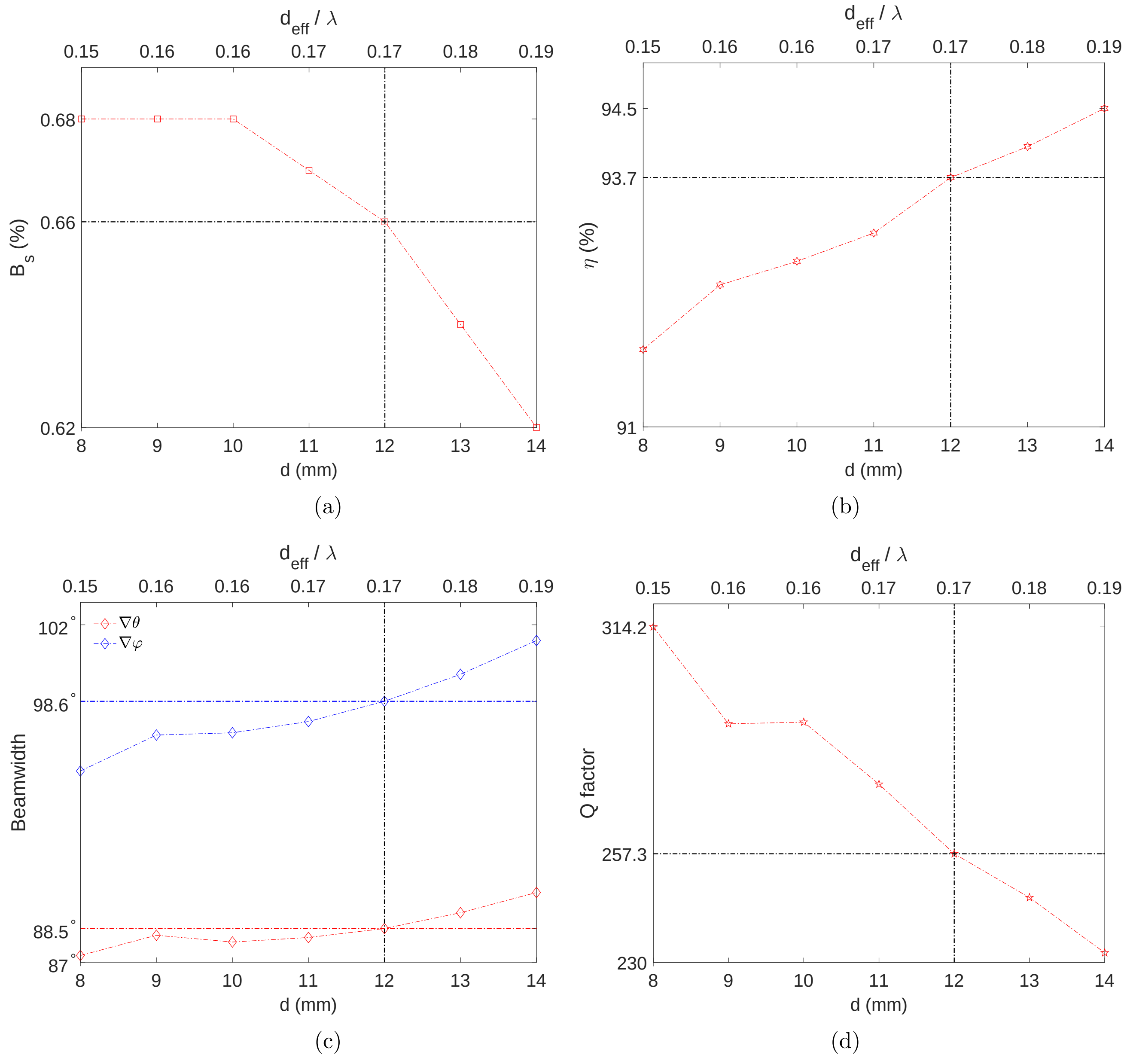

Figure 5.15: (a) The superdirectivity bandwidth, (b) the radiation efficiency, (c) the angular beamwidth and (d) the Q factor corresponding to the maximum directivity.

5.2.4 The 'CCLr' Structure

For the original 'CC' structure in Figure 5.1, increasing the diameter of its passive element can also help improve the directive performance. In this subsection, via adjusting the passive element's diameter, another alternative superdirective structure, 'CCLr', shown in Figure 5.16 is studied. The study consists of two steps: First, only the passive element's diameter is increased from $22mm$ to $34mm$ while the separation distance d is kept unchanged ($4mm$), for which the simulation results of the structure's antenna performance characteristics are shown in Figure 5.17∼5.18; Second, the separation distance d is increased from $4mm$ to $11mm$ and for each of these d values, an optimal diameter of the passive element (for $d = 4 \sim 6mm$, the optimal $2r_{Lr}$ is $32mm$; for $d = 7 \sim 11mm$, it is $34mm$) is chosen for the structure's best directive performance, for which the antenna performance characteristics are shown in Figure 5.19∼5.20.

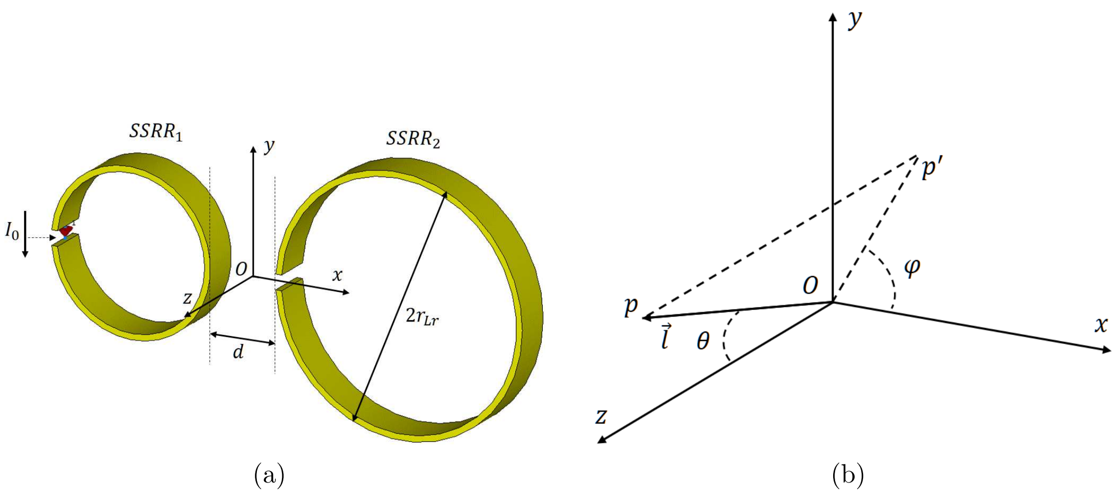

Figure 5.16: (a) The 'CCLr' structure and (b) its coordinate system.

Compared with previously studied structures in this section, this 'CCLr' provides a much more significant improvement in the directive performance by enlarging the passive element (Figure 5.17(a)). Here increasing the passive element's diameter not only has reduced the structure's operation frequency (Figure 5.17(b)), it has also adjusted the phase difference between the two SSRRs to a value requiring a smaller effective separation (0.13, in terms of one operation wavelength) to achieve the maximum directivity, which results in a larger directivity value of 4.78.

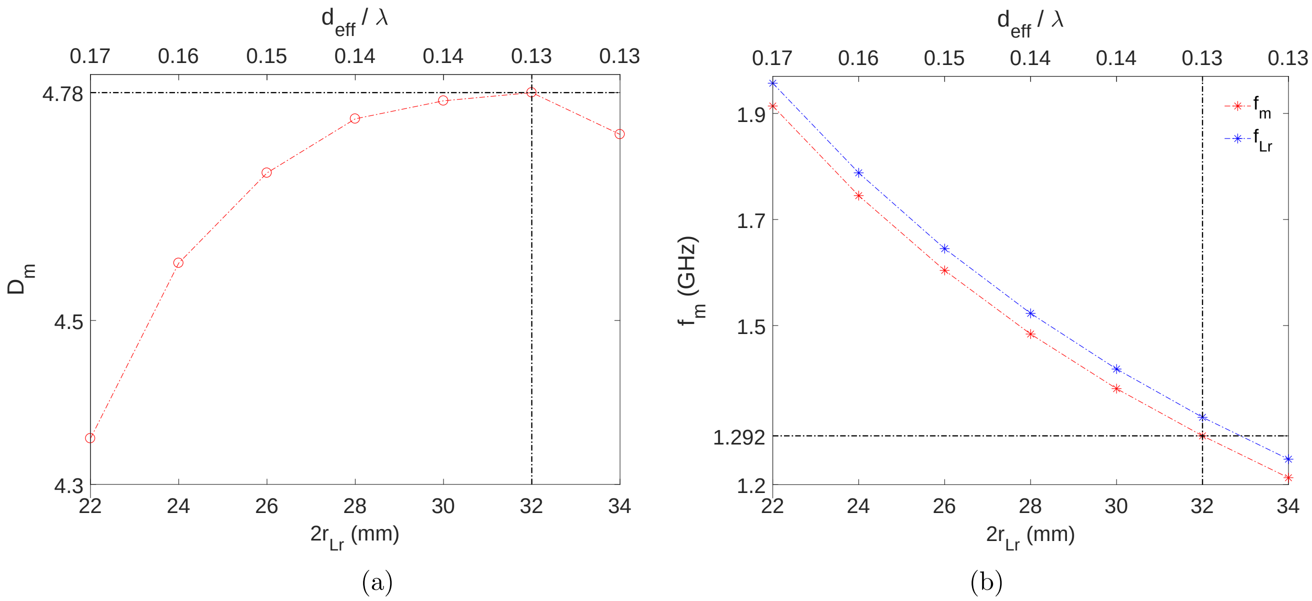

Figure 5.17: (a) The maximum directivity values, in the direction of $\theta = \pi/2, \varphi = 0$, and (b) their corresponding optimal frequencies, f_{Lr} is the resonance frequency of the enlarged SSRR element; the effective separation distance $d_{eff} = r + r_{Lr} + d$, where r is the radius of the original SSRR, r_{Lr} is the radius of the large SSRR element, λ is the operational wavelength; here $d = 4mm$ is kept unchanged.

Enlarging the passive element brings an improvement in the structure's superdirectivity bandwidth performance while at the cost of a reduced efficiency and a rising Q factor (Figure 5.18). The reduced efficiency simply results from the increased ohmic loss due to the increased metal size. The Q factor becomes higher because as the structure is enlarged, its radian sphere [42] is also increased, which can allow more energy stored surrounding the structure.

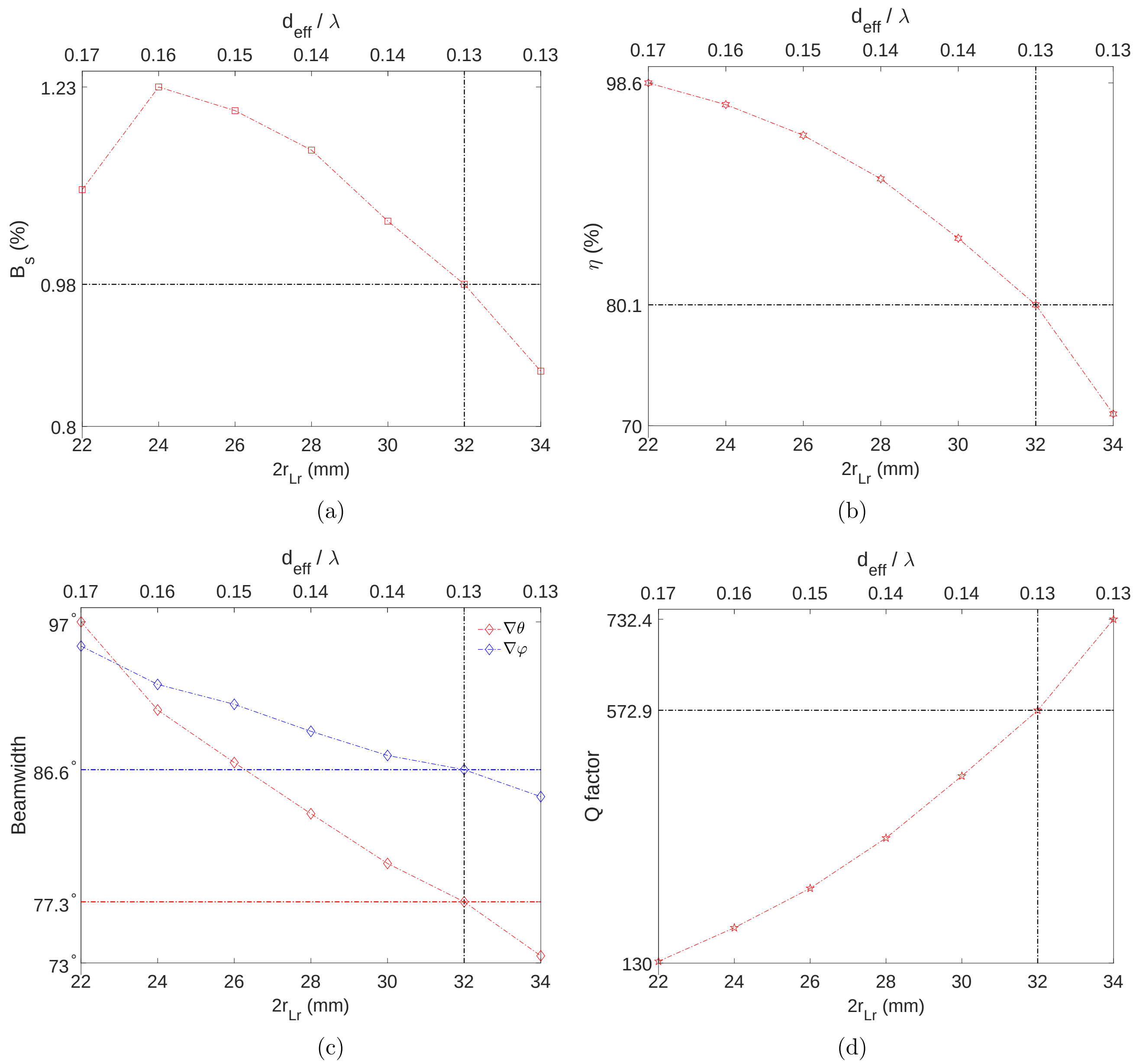

Figure 5.18: (a) The superdirectivity bandwidth, (b) the radiation efficiency, (c) the angular beamwidth and (d) the Q factor corresponding to the maximum directivity.

For the second step, increasing the separation distance provides a further improvement in the directive performance (Figure 5.19(a)): when $d = 9mm$ and $2r_{Lr} = 34mm$, an endfire directivity of 5.06, which is very close to the theoretical limit for a two-dipole array, is achieved at the operation frequency of $1.239GHz$. When the separation increases, once the passive element's diameter is fixed, the structure's antenna performance characteristics are still following same changing trends that the characteristics of the 'CC' structure follow.

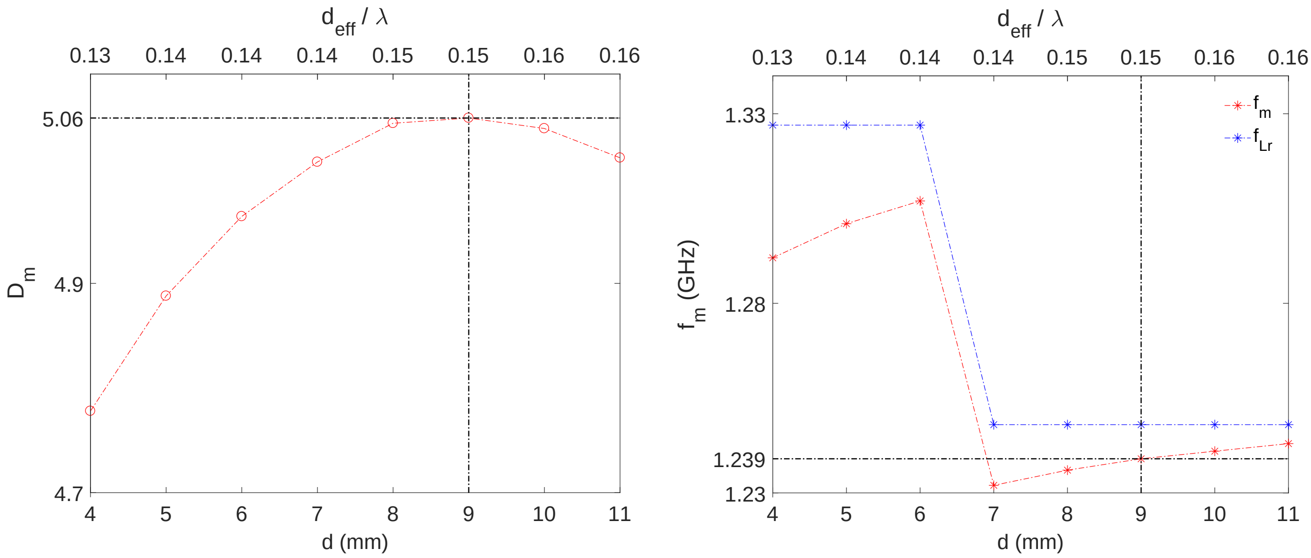

(a) (b)

Figure 5.19: (a) The maximum directivity values, in the direction of $\theta = \pi/2, \varphi = 0$, and (b) their corresponding optimal frequencies, f_{Lr} is the resonance frequency of the enlarged SSRR element; the effective separation distance $d_{eff} = r + r_{Lr} + d$, where r is the radius of the original SSRR, r_{Lr} is the radius of the large SSRR element, λ is the operational wavelength; here for $d = 4 \sim 6mm$, $2r_{Lr} = 32mm$, for $d = 7 \sim 11mm$, $2r_{Lr} = 34mm$.

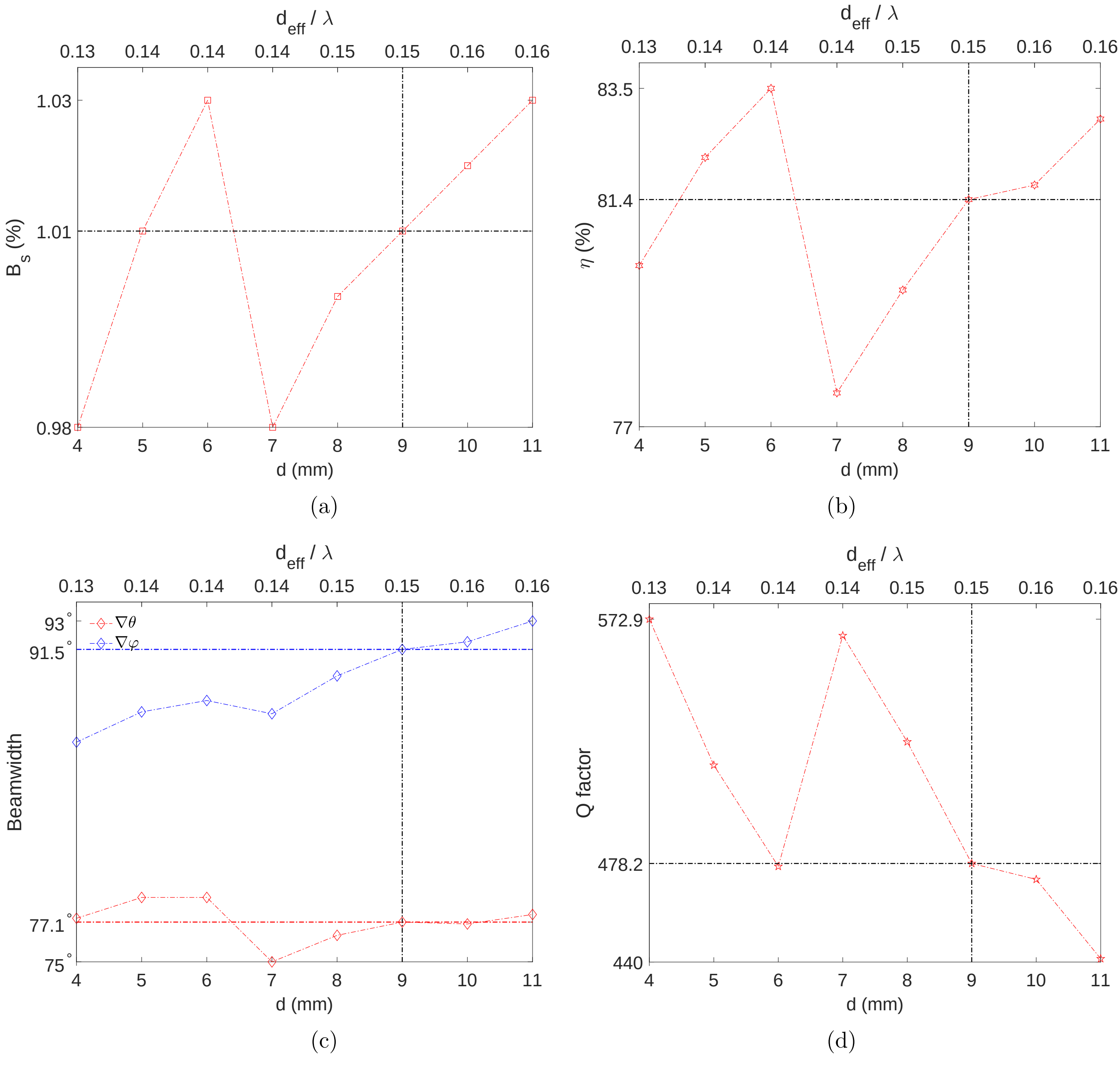

Figure 5.20: (a) The superdirectivity bandwidth, (b) the radiation efficiency, (c) the angular beamwidth and (d) the Q factor corresponding to the maximum directivity.

5.2.5 Other Structures

Another three alternative superdirective structures, shown in Figure 5.21, have also been explored. When the gap size of the original 'CC' structure's passive element is reduced from $2mm$ to $1.25mm$, the 'CCSg' structure is introduced, with an maximum endfire directivity of 4.37, standing for the best directive performance which can be achieved through only changing the passive element's gap size. Internally extending the 'CC' structure's passive element's gap introduces the 'CCIe' structure, shown in Figure 5.21(b). When the length of this internal extension is equal to $1mm$, the maximum directivity obtained is 4.38, which indicates the best directive performance only through adjusting the extension's length. Similarly, externally extending the 'CC' structure's gap introduces the 'CCEe' structure. When the length of the external extension $l_{ex} = 15mm$, a maximum directivity of 4.93, which stands for the best directive performance obtained through adjusting the extension's length, is achieved. In next section, a summary table, which includes all studied superdirective structures in this section, along with the antenna performance characteristics corresponding to these structures' best directive performance, will be presented and described.

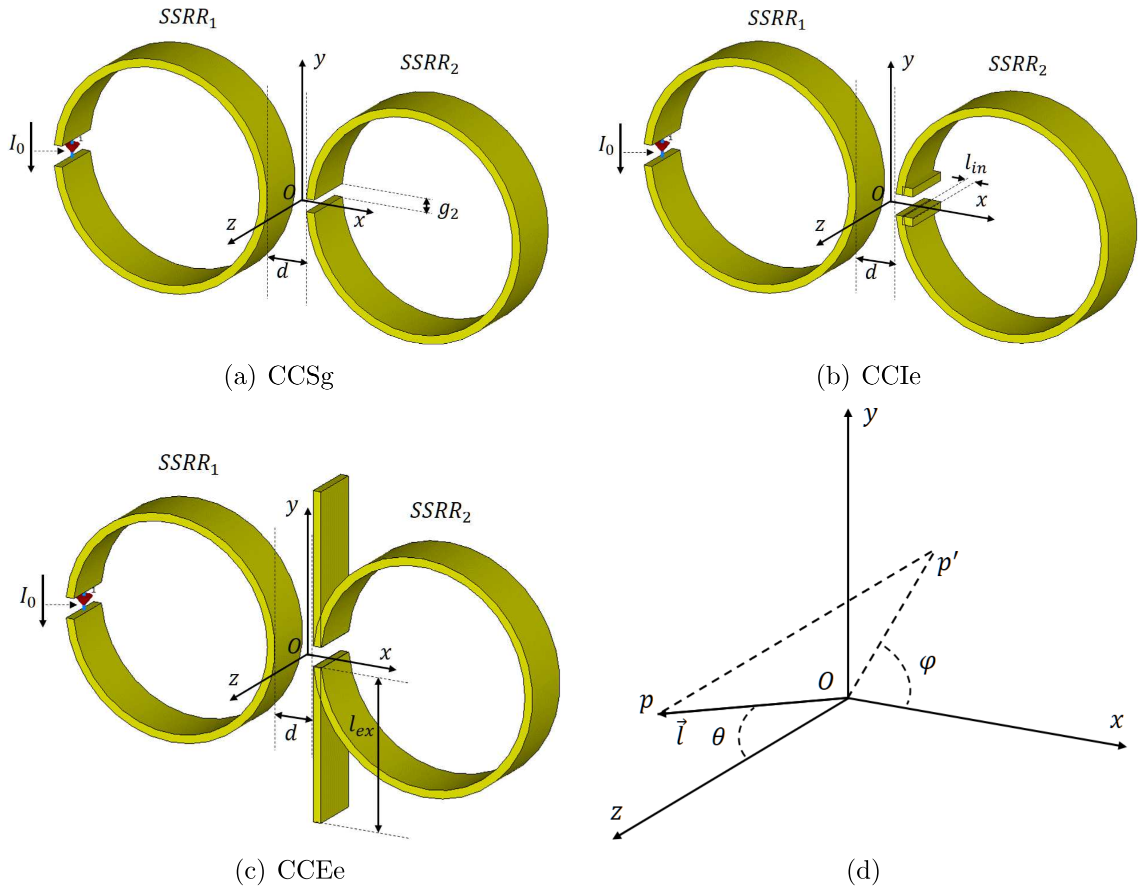

(a) CCSg (b) CCIe (c) CCEe (d)

Figure 5.21: Another three variants of the 'CC' structure: (a) 'CCSg', a smaller gap for the passive element; (b) 'CCIe', an internal extension of the passive element's gap; (c) 'CCEe', an external gap extension; (d) the coordinate system. Here $d = 4mm$.

5.3 Summary Tables of Superdirective Structures

A table of all superdirective structures studied in this research, along with their passive elements' shapes, dimensions and properties for these structures' best directive performances, is presented as Table 5.1. In this table, a passive element is labelled as SSRR$_2$, whose shape and dimension are described referring to a standard SSRR shown in Figure 5.22. The 2D normalized far field average radiation energy patterns for a standard SSRR, the 'CC' structure, the 'CCEx' structure, the 'CCDg' structure, the 'CCDgEx' structure, the 'CCLr' structure and the 'CCEe' structure are displayed in Figure 5.23. Due to the normalization, the radial axes of the polar plots are exactly denoting the far field directivity values.

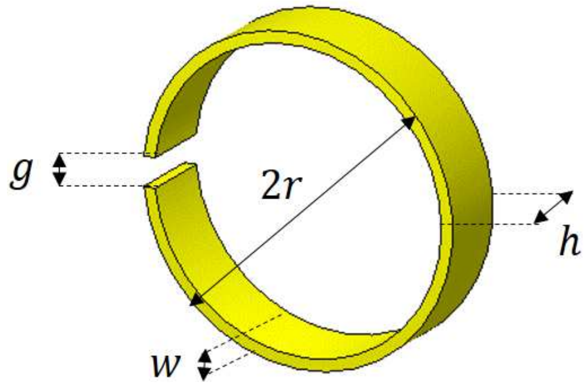

Figure 5.22: A standard copper SSRR: $2r = 22mm$, $h = 5mm$,$g = 2mm$ and $w = 0.8mm$.

Structure	Name	d (mm)	$SSRR_2$ (referring to a standard SSRR)	$f_0(GHz)$ of $SSRR_2$	$Q\ factor$ of $SSRR_2$	D_m
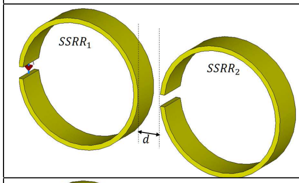	CC	4	Standard	1.957	26.7	4.36
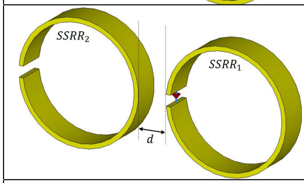	CCEx	5	Standard	1.957	26.7	4.45
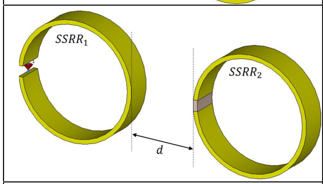	CCDg	12	Gap filled with alumina	1.546	65	4.53
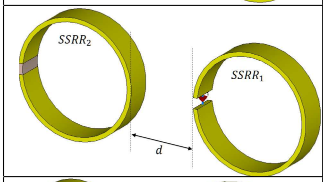	CCDgEx	12	Gap filled with alumina	1.546	65	4.56
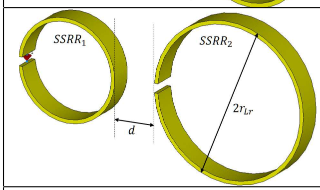	CCLr	9	$2r_{Lr} = 34mm$	1.248	28.4	5.06
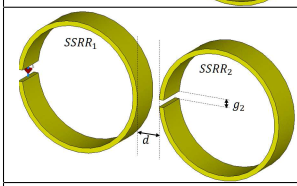	CCSg	4	$g_2 = 1.25mm$	1.86	32.5	4.37
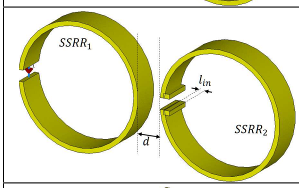	CCIe	4	$l_{in} = 1mm$	1.88	31.3	4.38
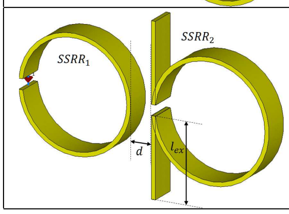	CCEe	4	$l_{ex} = 15mm$	1.658	27	4.93

Table 5.1: Superdirective structures and their passive elements' ($SSRR_2$) shapes, dimensions (referring to a standard SSRR shown in Figure 5.22) and features corresponding to the structures' best directive performances.

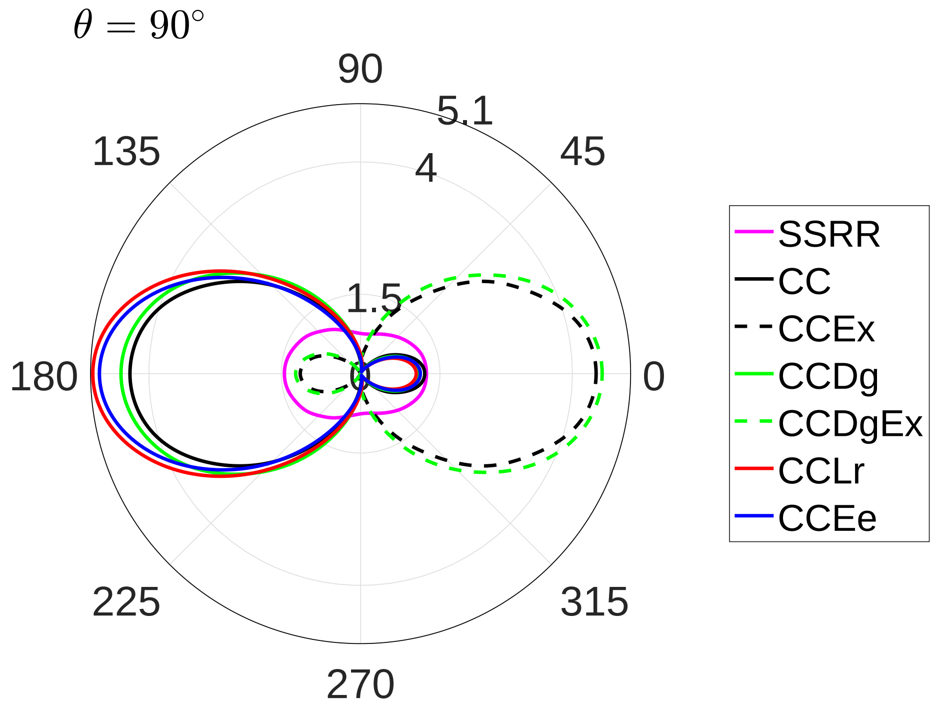

(a)

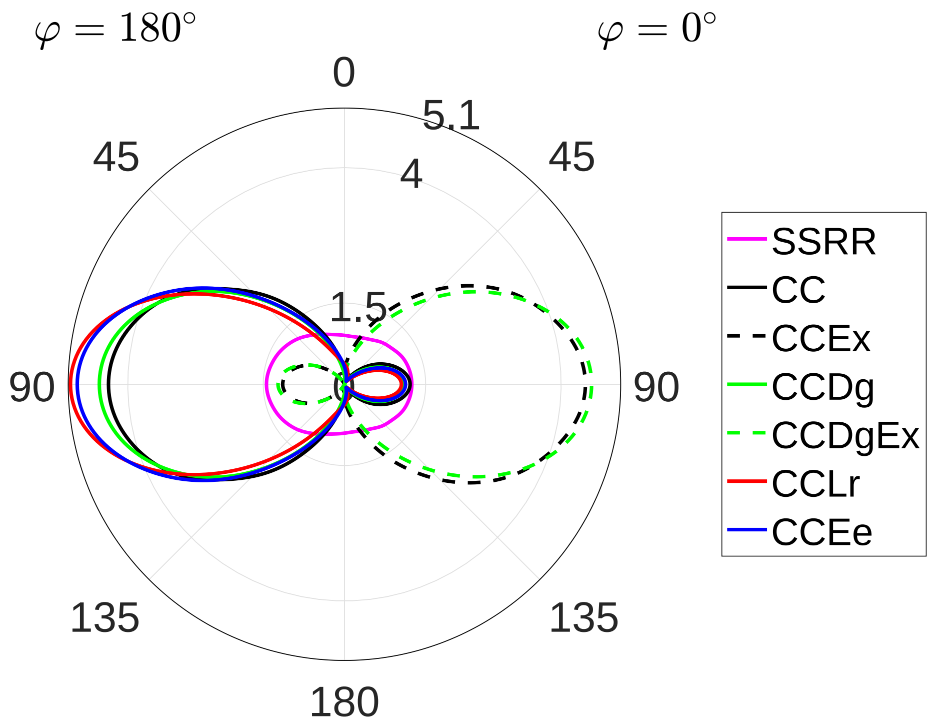

(b)

Figure 5.23: The 2D normalized radiation energy patterns for the standard SSRR and selected superdirective structures: (a) xy plane patterns, (b) xz plane patterns.

The maximum directivity values, the optimal operation frequencies and other corresponding antenna performance characteristics for the above superdirective structures are shown in Table 5.2. According to this table, both the 'CC' and the 'CCEx' structure can provide large superdirective directivity values while sustain good performances in the superdirectivity bandwidth, the efficiency and the Q factor. Among them, the 'CCEx' structure shows slight improvements over the 'CC' in all respects. Compared with these two structures, either the 'CCDg' structure or the 'CCDgEx' structure can achieve a better directive performance while at the cost of a smaller bandwidth, a lower efficiency and a higher Q factor. However, just considering these two structures ('CCDg' and 'CCDgEx'), it can be clearly seen that except their superdirectivity achieves in opposite directions, they present almost the same performance characteristics as antennas, which might be useful for certain application designs requiring stable alternating bidirectional superdirective radiation. For those applications very sensitive to directive performance, the 'CCLr' structure and the 'CCEe' structure can be good choices. Both these two structures can provide very high superdirective directivity values, which are close to the theoretical limit value (5.25) of a two-dipole array, at the cost of low radiation efficiencies and high Q factors.

Structure	CC	CCEx	CCDg	CCDgEx	CCLr	CCSg	CCIe	CCEe
D_m	4.36 $\leftarrow$	4.45 $\rightarrow$	4.53 $\leftarrow$	4.56 $\rightarrow$	5.06 $\leftarrow$	4.37 $\leftarrow$	4.38 $\leftarrow$	4.93 $\leftarrow$
$f_{D_m}(GHz)$	1.914	1.944	1.538	1.539	1.239	1.819	1.838	1.615
$B_s(\%)$	1.1	1.49	0.59	0.66	1.01	0.98	1.02	0.88
$\eta(\%)$	98.6	99.1	93.8	93.7	81.4	97.5	98	89.2
$\Delta\theta$ (xy-plane)	97°	97.8°	89.2°	88.5°	77.1°	93.4°	94.4°	85.1°
$\Delta\varphi$ (xz-plane)	95.3°	92.5°	101°	98.6°	91.5°	95°	95.4°	87.5°
$Q\ factor$	133.1	126.9	254.5	257.3	478.2	170	159.7	414.9

Table 5.2: The maximum directivities, the optimal frequencies and the corresponding antenna performance characteristics (B_s, η, the beamwidth and the Q factor) for the superdirective structures shown in Table 5.1; The arrow following the D_m value indicates the direction in which the superdirectivity occurs, referring to the coordinate system shown in Figure 5.1: a left arrow indicates the negative x direction while a right arrow indicates the positive x direction.

In order to show that the proposed and studied structures based on our new design principle in this research can provide better directive performances than the antennas based on Yagi-Uda design principle can do, a comparison (see Table 5.3) is made between superdirective structures (the ‘CC’, the ‘CCDg’, the ‘CCLr’ and the ‘CCEe’) selected from Table 5.2 and two commonly used commercial two-element Yagi antennas. One (labelled as SteppIR here) of the two Yagi antennas is from *SteppIR Antennas* and another one (JK402) is from *JK Antennas*. Their specifications are listed on the two companies’ websites [135] [136]. According to Table 5.3, both the two Yagi antennas can produce similar even better linear maximum gain compared with the four superdirective structures, but their giant sizes (L_{max}) suggests they are far from being superdirective. Even when considering the electrical size (L_{max}/λ), the ratio R_{GL} still implies that our structures are considerably more directive than the two realistic antennas are.

Structure/antenna	CC	CCDg	CCLr	CCEe	SteppIR	JK402
G_{lin}	4.3	4.25	4.12	4.4	4.57	4.12
f_{op} (MHz)	1914	1538	1239	1615	20	40
L_{max} (m)	0.048	0.056	0.065	0.048	10.973	14.478
L_{max}/λ	0.31	0.29	0.27	0.26	0.73	1.93
$R_{GL} = \frac{G_{lin}}{L_{max}/\lambda}$	13.9	14.7	15.3	16.9	6.3	2.1

Table 5.3: The linear maximum gain, the operation frequency, the maximum dimension (in meters and in terms of the corresponding operation wavelength) and the R_{GL} for the 'CC' structure, the 'CCDg' structure, the 'CCLr' structure, the 'CCEe' structure, the two-element Yagi antennas: the SteppIR antenna working at $20MHz$ fabricated by SteppIR and the JK402 antenna working at $40MHz$ fabricated by JK Antennas; The data of the two Yagi antennas are measured data provided by their websites.

5.4 Conclusion

First, the analytical prediction that a 'CC' structure can produce superdirectivity has been verified by CST simulations. Based on simulation results, when the structure achieves superdirectivity, the antenna performance characteristics of the structure (the mximum directivity, the optimal frequency, the superdirectivity bandwidth, the efficiency, the beamwidth and the Q factor) can be adjusted through changing the elements' separation. Also the design principle behind this 'CC' structure has been discussed.

Second, improved superdirective structures, namely 'CCEx', 'CCDg', 'CCDgEx', 'CCLr', 'CCSg', 'CCIe' and 'CCEe', are identified. Especially for the 'CCEx', the 'CCDg' and the 'CCDgEx', their antenna performance characteristics are studied against an increasing elements' separation, and for the 'CCLr' the same characteristics are studied when increasing the passive element's diameter and the separation, based on simulation results.

Third, according to the antenna performance characteristics identified corresponding to the studied structures' best directive performances: (a) Both the 'CC' and the 'CCEx' structure can provide large superdirective directivity values while sustain good performances in the bandwidth, the efficiency and the Q factor, and the 'CCEx' structure shows slight improvements over the 'CC' in all respects. (b) Combining the 'CCDg' and the 'CCDgEx' might be useful for certain application designs requiring stable alternating bidirectional superdirective radiation. (c) Either the 'CCLr' or the 'CCEe' can provide very large directivity values, which are very close to the theoretical limit value (5.25) of a two-dipole array, at the cost of a small bandwidth, a low efficiency and a high Q factor.

Fourth, these two-SSRR parasitic superdirective structures (the 'CC' and its improved structures) show better directive performances than the realistic two-element Yagi antennas do.

Chapter 6

Energy Flow

Since two-SSRR parasitic superdirective structures have been realized and their antenna performance characteristics have been studied based on simulation results, the aim of this chapter is to explore the near field physical mechanism behind the far field superdirectivity phenomenon through studying the energy flow surrounding the radiating structures. The study of near field energy flow is performed through analysing both the time-average Poynting vector and the instantaneous Poynting vector, with the help of the concept of causal surfaces.

After a brief introduction of causal surfaces, the energy flow for a single magnetic dipole and two-dipole arrays (non-superdirective and superdirective) is analytically studied and visualised. Then the energy flow study is again implemented for a standard SSRR and two-SSRR arrays (superdirective and non-superdirective) based on CST simulation data. In the end, a comparative discussion, considering all above analysed structures, reveals the physical reason behind superdirectivity.

The main new contributions in this Chapter include: 1. The visualization of the near field power flow for dipole based and SSRR based non-superdirective and superdirective structures; 2. A explanation of the far field superdirectivity effect with the help of the causal surface.

6.1 Causal Surface

The concept of causal surfaces was first raised by *Schantz* in 1995 [137]. It exists due to the existence of a surface where the overall magnetic field approaches zero because the induced magnetic field and the radiated magnetic field, around a changing current, point in opposite directions. This causal surface partitions the original static field energy into a radiated portion and an absorbed portion, which can be noticed on energy flow plots and space-time diagrams.

6.2 Energy Flow: Dipole and Two-dipole Arrays

The 2D normalized far field average radiation energy patterns for an ideal magnetic dipole, two non-superdirective arrays comprised of two identical ideal magnetic dipoles and a superdirective array of two identical ideal magnetic dipoles (Figure 6.1), are displayed in Figure 6.2. Due to a proper normalization, the polar plots' radial axes indicate the far field directivity values.

A magnetic dipole can be regarded as a small loop carrying a uniform current [10]. For a single magnetic dipole, its far field radiation pattern presents a doughnut shape and its maximum far field directivity remains 1.5 in the loop (circular current) plane as Figure 6.2 suggests. For an array of two magnetic dipoles, with a fixed elements' separation (here $d_{eff} = 0.1\lambda$) and a set of currents as: $I_1 = I_0 e^{-i\beta/2}$ and $I_2 = I_0 e^{i\beta/2}$, where I_0 is the common current magnitude and β is the phase difference. Through properly choosing the phase difference β, the array can be either non-superdirective or superdirective. Here, setting the phase difference to be 0 makes the array produce a very similar far field radiation pattern with that produced by a single magnetic dipole; Setting the phase difference to be 0.5π makes the array show a preferential radiation direction but it is not significant enough to achieve superdirectivity; Setting the phase difference as $\beta = 0.922\pi$ makes the array optimally superdirective with a

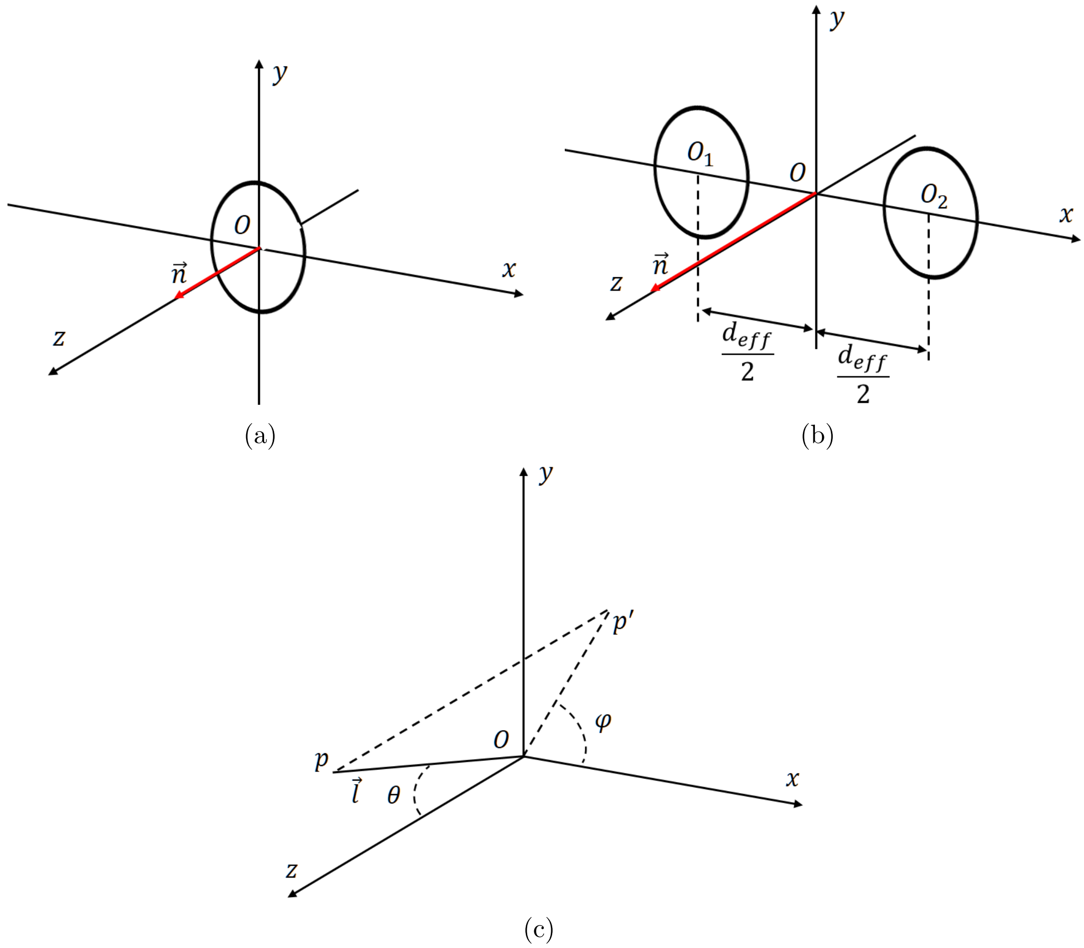

Figure 6.1: The sketches of (a) a single magnetic dipole, (b) an array of two magnetic dipoles and (c) their common coordinate system: here for the array, d_{eff} is set to be 0.1λ; λ is the operation wavelength; p is the observation point in far field.

endfire directivity of 5.1.

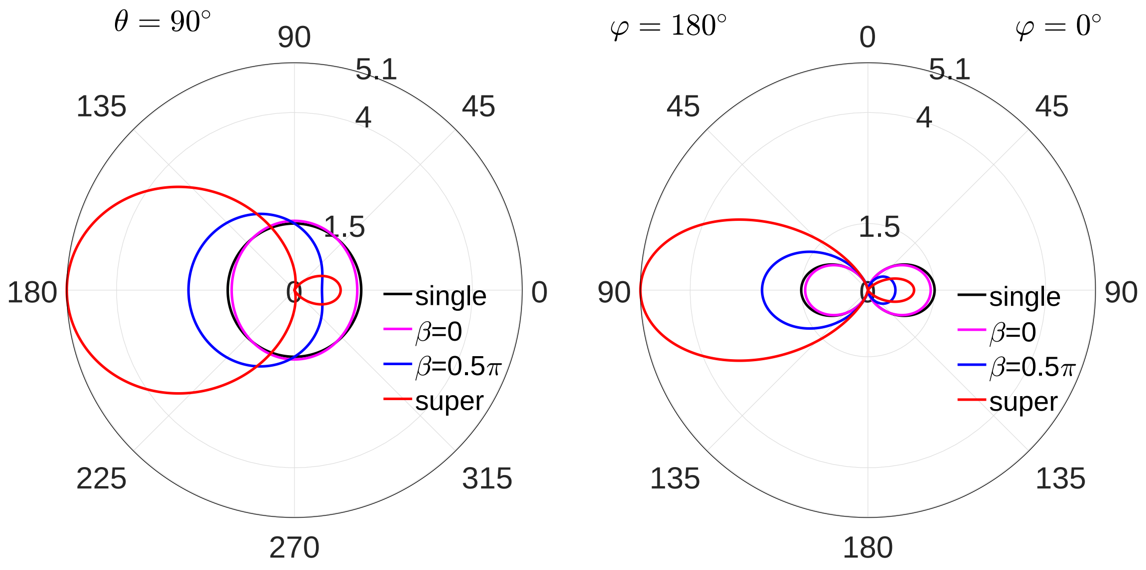

(a) (b)

Figure 6.2: The 2D normalized far field radiation energy patterns for a single magnetic dipole, a $\beta = 0$ non-superdirective array of two magnetic dipoles, a $\beta = 0.5\pi$ non-superdirective array of two magnetic dipoles and a superdirective array of two magnetic dipoles: (a) xy plane patterns, (b) xz plane patterns; The radial axes of the polar plots indicate the far field directivity values; β is the phase difference between the currents carried by an array's two dipole elements.

For the energy flow study in near field region ($|\vec{l}| < \lambda$), the time-average Poynting vectors for the above four dipole structures are firstly shown in Figure 6.3. It can be clearly seen that for the single magnetic dipole and for the $\beta = 0$ non-superdirective array the energy flows outwards strictly along radial lines (Figure 6.3(a)) avoiding only the z-direction, whereas for the superdirective array (Figure 6.3(d)) the streamlines follow curved paths forming a single preferential direction in the endfire (negative x) direction. The $\beta = 0.5\pi$ non-superdirective array (Figure 6.3(c)) shows in between behaviours that a direction preference of the energy flow can be noticed but it is not as strong as that is for a superdirective array. The colour bar (Figure 6.3(e)) adopted here indicates a fixed range of the energy density, which applies to all plots of the radial energy flow (time-average and instantaneous) in this section (Section 6.2) except the space-time diagrams.

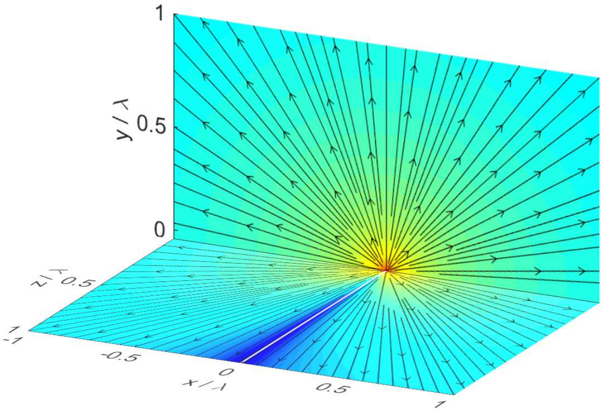

(a) Single dipole

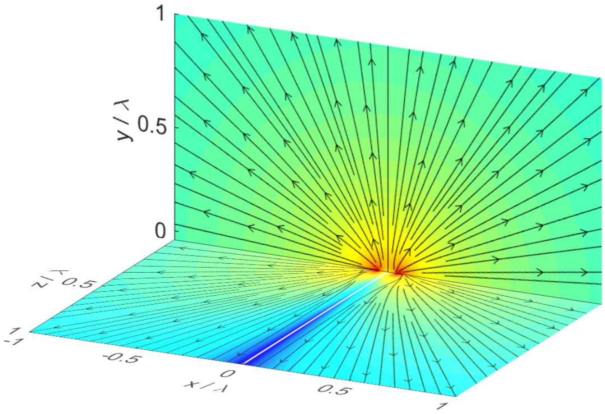

(b) $\beta = 0$ array

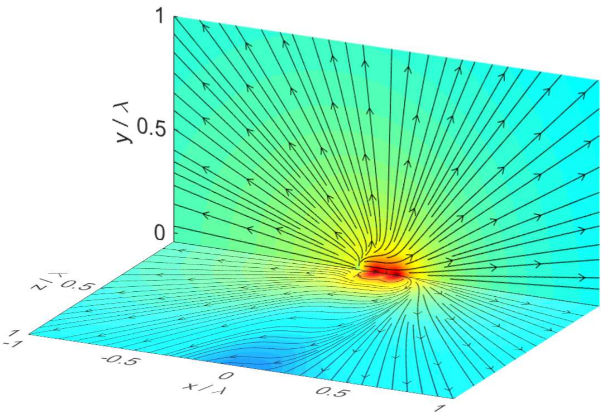

(c) $\beta = 0.5\pi$ array

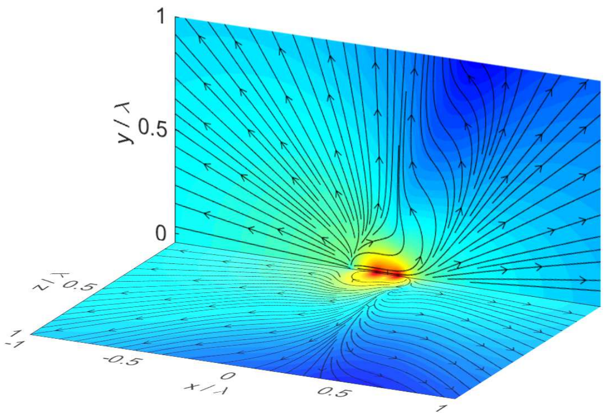

(d) Superdirective array

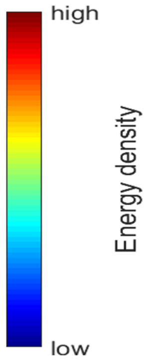

(e) Color bar

Figure 6.3: The time-average energy flow in near field region for (a) a single magnetic dipole, (b) a $\beta = 0$ non-superdirective array of two identical magnetic dipoles, (c) a $\beta = 0.5\pi$ non-superdirective array of two magnetic dipoles and (d) a superdirective array; The color map shows the logarithmic scale of the time-average energy density as (e) the color bar indicates; The streamlines indicate the time-average Poynting vectors corresponding to the energy density.

In order to better understand the time-average behaviours, it is necessary to analyse the time evolution of the instantaneous Poynting vector. Here a harmonic time dependence of $e^{i\omega t}$ is assumed for the electromagnetic fields. Figure 6.4∼6.7 show the instantaneous Poynting vectors of four time frames ($t = 0$, $t = 0.125T$, $t = 0.25T$ and $t = 0.375T$) for a single magnetic dipole, a $\beta = 0$ non-superdirective array, a $\beta = 0.5\pi$ non-superdirective array and a superdirective array, corresponding to Figure 6.3. T is the time period for the electromagnetic fields corresponding to the assumed harmonic time dependence. Here the expression $t = 0$ indicates the start time frame of a specific time circle, not the time point when a radiating structure starts to work. Based on the calculation of the Poynting vector, it can be easily concluded that the period of energy flow equals to $0.5T$, half of the fields' period. Therefore the chosen four time frames should be enough to show the progressive changes of energy flow within one periodic time circle. The instantaneous Poynting vector allows us to visualize both the radiated and the stored energy. These two types of energy are spatially separated by the so called causal surfaces [138], which can be described as surfaces with zero energy flow across them. These causal surfaces can be clearly seen in Figure 6.4∼6.7 as dark blue contours.

For either the case of a single magnetic dipole (see Figure 6.4) or the case of a $\beta = 0$ non-superdirective array, the causal surface has a regular spherical shape, which gradually moves away from the radiating structure as time grows. The regularity of these surfaces, indicating zero radial energy flow, ensures exactly same portion of energy radiates in any direction and no preferential radiation direction can be possibly formed in xy plane. This apparently agrees with the omnidirectional far field radiation patterns of these two structures (Figure 6.2).

The existence of tangential energy flow on the causal surfaces implies that the Poynting vectors inside and outside such a surface do not necessarily point in opposite directions (see Figure 6.4((a), (c), (d)) and Figure 6.5((a), (c), (d))). Only during a certain time slot [1] (see Figure 6.4(b) and Figure 6.5(b)), within the vicinity of a radiating structure, inside one causal surface the energy flows back towards the dipole while outside the surface the energy still flows outwards normally.

[1] For a single magnetic dipole, it is the first quarter of the period, which will be seen from the corresponding space-time diagram shown in Figure 6.8.

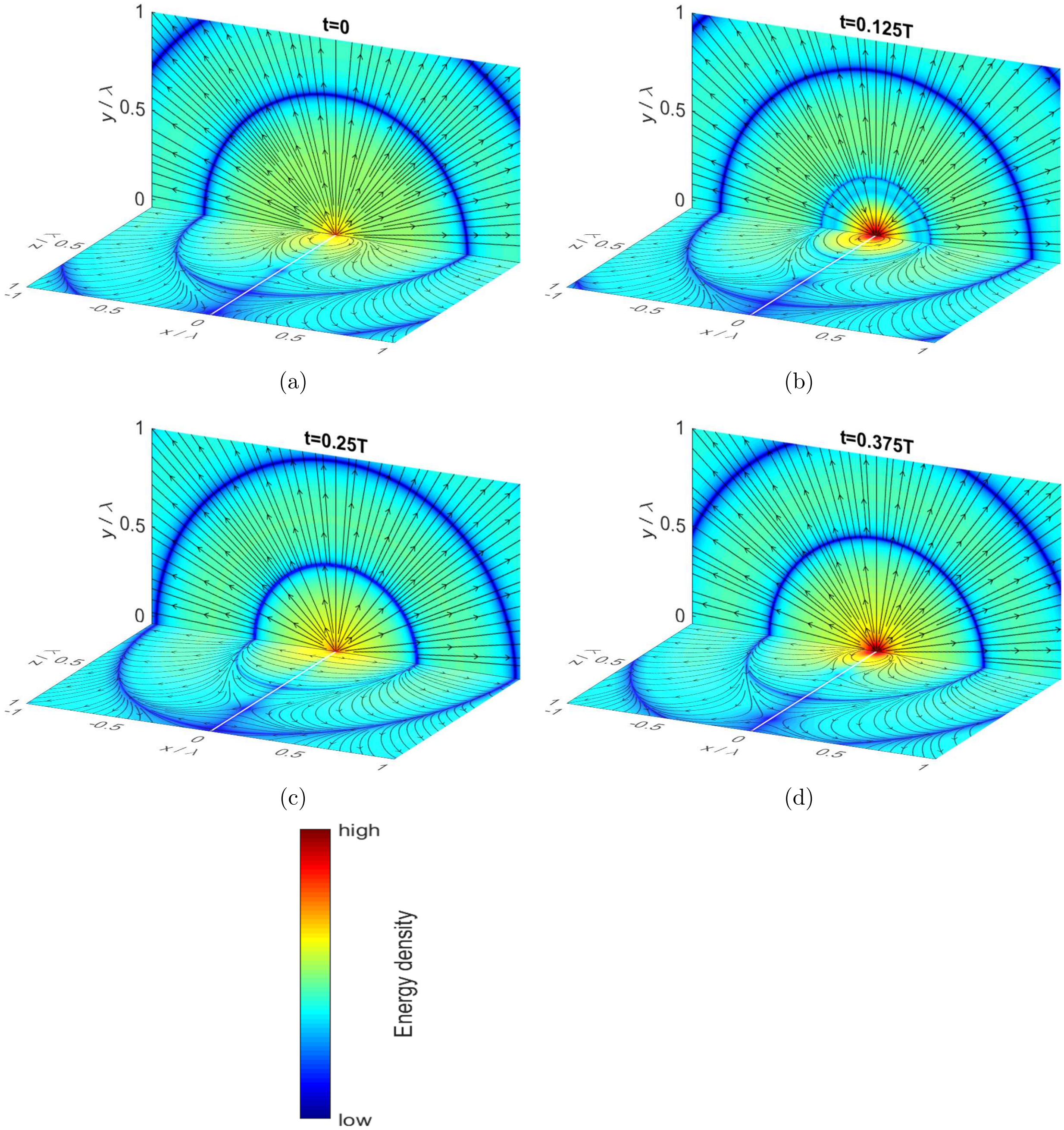

(a) (b) (c) (d)

(e) Color bar

Figure 6.4: The instantaneous energy flow of a single magnetic dipole in near field region for four time frames: (a) $t = 0$, (b) $t = 0.125T$, (c) $t = 0.25T$ and (d) $t = 0.375T$; The colour map shows the logarithmic scale of the instantaneous energy density as (e) the colour bar indicates; The streamlines indicate the instantaneous Poynting vectors corresponding to the energy density.

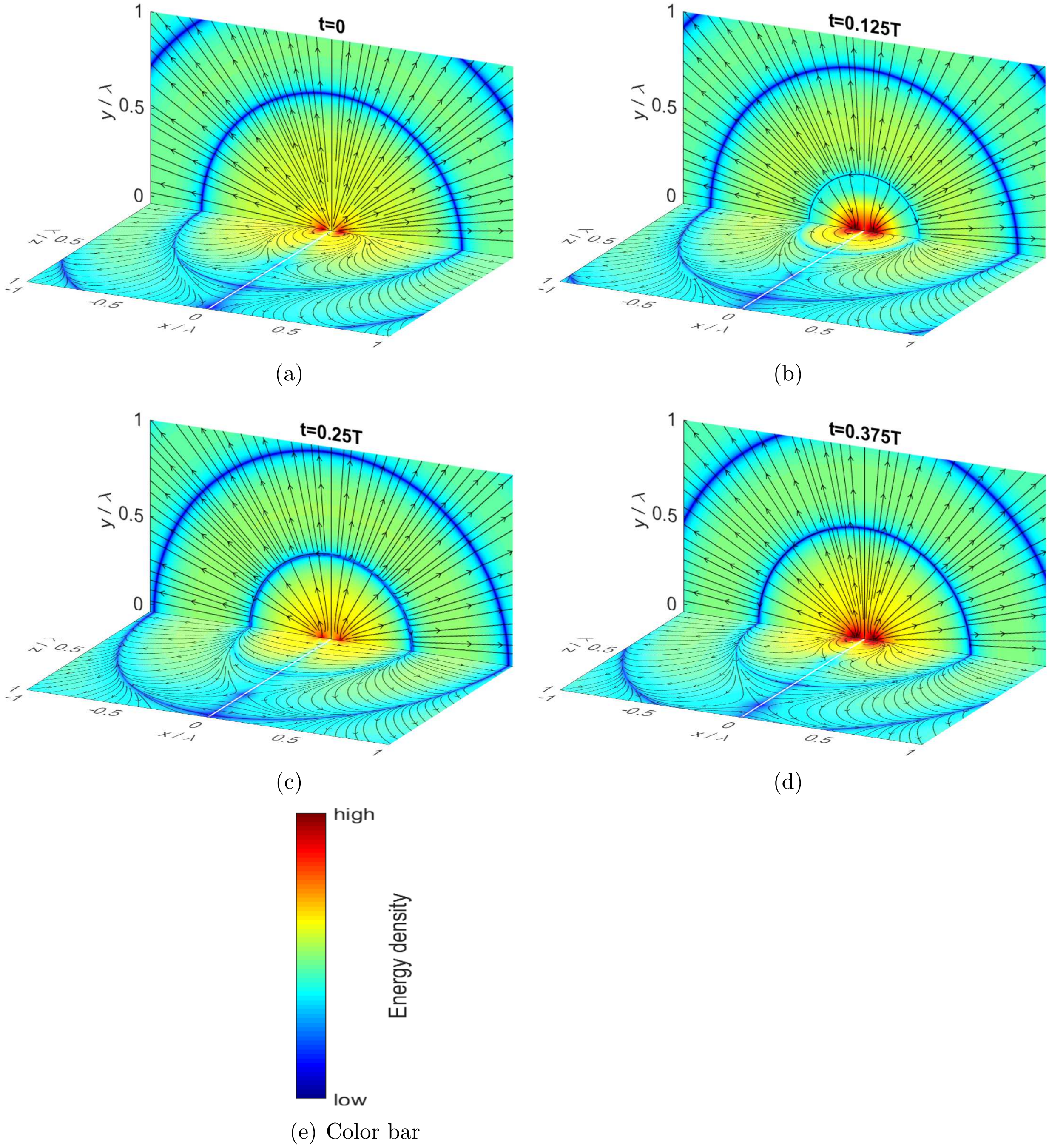

Figure 6.5: The instantaneous energy flow of $\beta = 0$ non-superdirective array of two magnetic dipoles in near field region for four time frames: (a) $t = 0$, (b) $t = 0.125T$, (c) $t = 0.25T$ and (d) $t = 0.375T$; The colour map shows the logarithmic scale of the instantaneous energy density as (e) the colour bar indicates; The streamlines indicate the instantaneous Poynting vectors corresponding to the energy density.

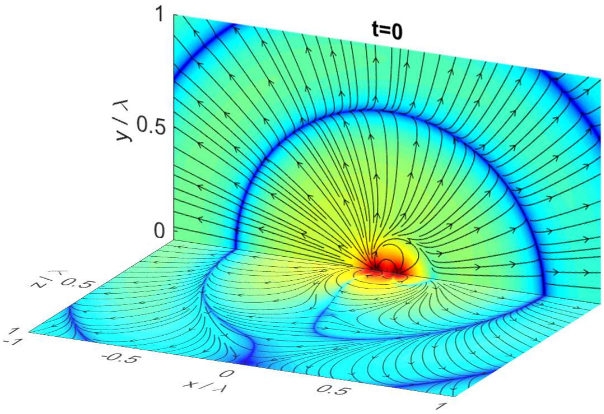

(a)

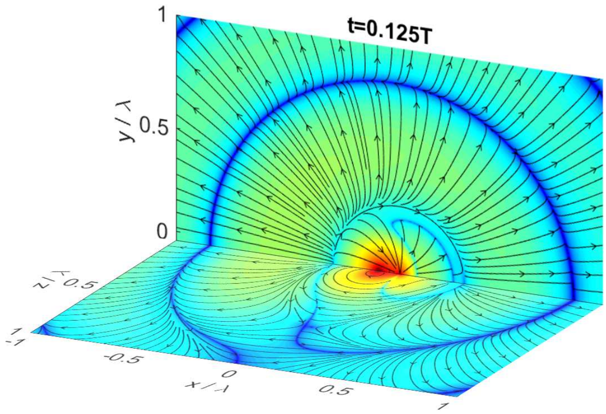

(b)

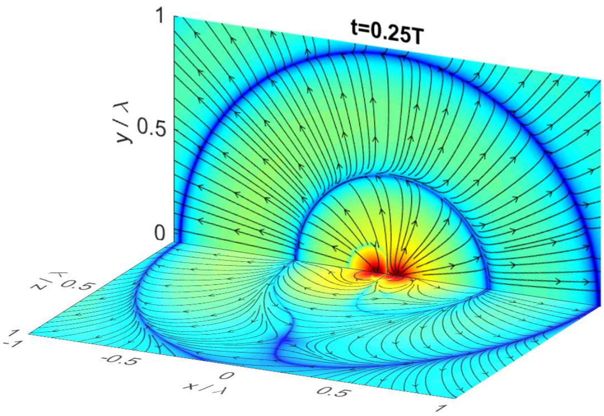

(c)

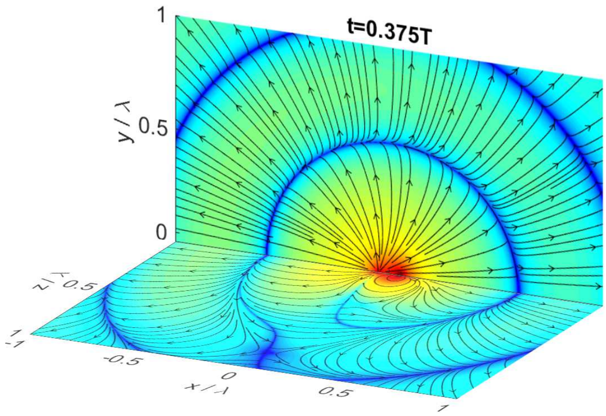

(d)

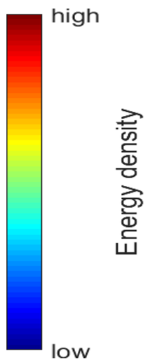

(e) Color bar

Figure 6.6: The instantaneous energy flow of a $\beta = 0.5\pi$ non-superdirective array of two magnetic dipoles in near field region for four time frames: (a) $t = 0$, (b) $t = 0.125T$, (c) $t = 0.25T$ and (d) $t = 0.375T$; The colour map shows the logarithmic scale of the instantaneous energy density as (e) the colour bar indicates; The streamlines indicate the instantaneous Poynting vectors corresponding to the energy density.

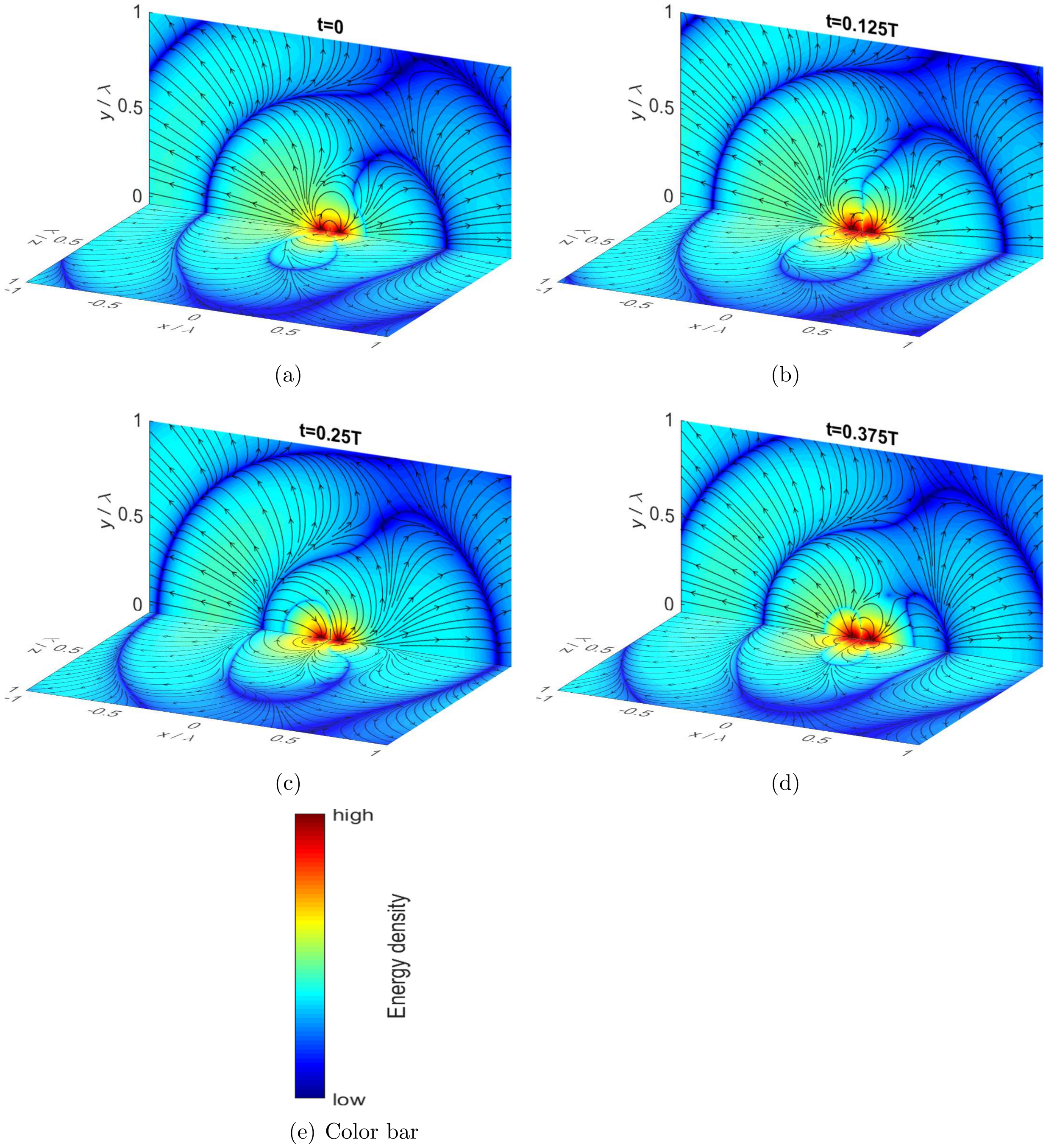

(a) (b) (c) (d)

(e) Color bar

Figure 6.7: The instantaneous energy flow of a superdirective array of two magnetic dipoles in near field region for four time frames: (a) $t = 0$, (b) $t = 0.125T$, (c) $t = 0.25T$ and (d) $t = 0.375T$; The colour map shows the logarithmic scale of the instantaneous energy density as (e) the colour bar indicates; The streamlines indicate the instantaneous Poynting vectors corresponding to the energy density.

Different from the cases for a single magnetic dipole and a $\beta = 0$ non-superdirective array, in Figure 6.7 the causal surface of the superdirective array shows a significant distorted shape rather than a regular one. Even though the causal surface also moves away from the array as time grows, its distorted shape makes the energy no longer evenly flow in xy plane and forces a preferential radiation direction ($\theta = \pi/2$ and $\varphi = \pi$) to form. The shape distortion is believed to result from the constructively and destructively interference of the fields generated by the array's two dipole elements, which carry currents with a same magnitude and an appropriately chosen phase difference ($\beta = 0.922\pi$) corresponding to the elements' separation ($d_{eff} = 0.1\lambda$). Also unlike what Figure 6.4 and Figure 6.5 show, here the phenomenon that energy flows back to the radiating structure, in its vicinity, from the two endfire directions ($\theta = \pi/2$, $\varphi = \pi$ and $\theta = \pi/2$, $\varphi = 0$) do not always happen at the same time, which can be seen more clearly from the corresponding space-time diagram (Figure 6.8).

For the case of a $\beta = 0.5\pi$ non-superdirective array, the causal surface (see Figure 6.6) also shows a shape distortion compared with those of a single dipole and a $\beta = 0$ array, but this distortion is far from being as significant as that for a superdirective array. Therefore a slight preference of radiation direction can be noticed but it is not strong enough for the array to be superdirective.

Energy flow can also be visualized using the so called space-time diagrams [138], displayed in Figure 6.8 for the positive and negative x direction. Each of the space-time diagrams in Figure 6.8 shows, as a contour plot, the variation of the direction (inwards or outwards) of the instantaneous Poynting vector's radial component along the x axis as a function of time. The regions of the inwards energy flow associated with the stored energy shown as dark blue areas are separated by the regions of the outwards energy flow (yellow). The transition to the far field (as $|x|$ increases) is accompanied by the merging of the burst of the radiated energy seen also in Figure 6.4~6.7 as areas separated by zero energy flow surfaces spreading in space with the velocity of light.

On these space-time diagrams, the causal surfaces always show up as pairs (causal pairs). For each of these causal pairs, there is always one causal surface on the left hand side while the other one on the right hand side of the line $x = 0$. For either a single magnetic dipole (Figure 6.8(a)) or a $\beta = 0$ array (Figure 6.8(b)), the two causal surfaces of every causal pair always appear symmetrically on the two sides of the line $x = 0$. However for either the $\beta = 0.5\pi$ array (Figure 6.8(c)) or the superdirective array (Figure 6.8(d)), the appearance of the causal pairs shows an asymmetry about the line $x = 0$. Due to the relative time shift between the inwards energy flow regions (dark blue), on the left and right hand side of the $x = 0$ line, the distances from the two causal surfaces of one causal pair to the line $x = 0$ no longer equal to each other, which, corresponding to the causal surfaces' distortions in Figure 6.6 and 6.7, then results in a preferential energy radiation direction. Here only for the superdirective array, the asymmetry is significant enough to form a strong preference for endfire radiation, which finally leads to the endfire superdirectivity.

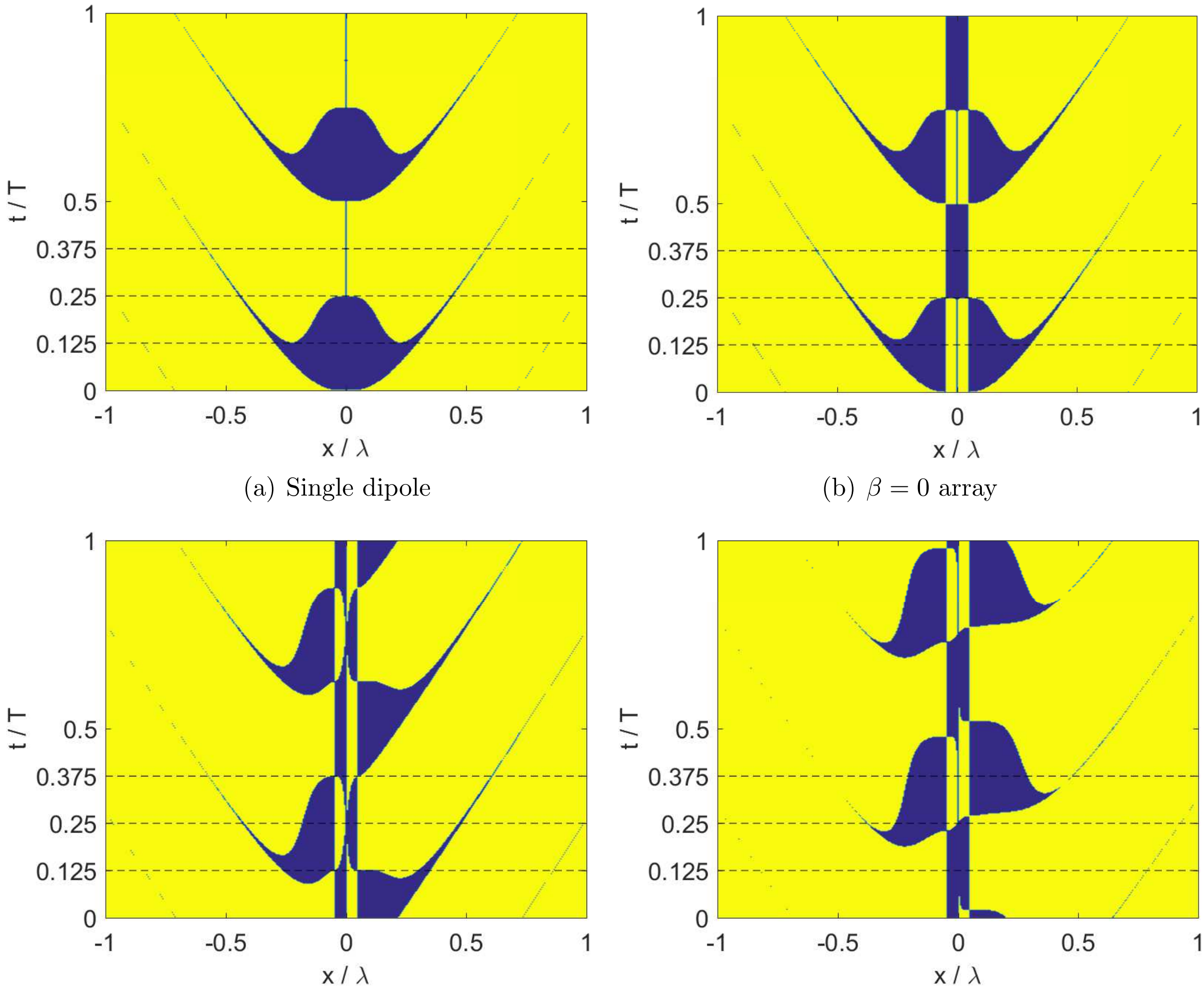

(a) Single dipole

(b) $\beta = 0$ array

(c) $\beta = 0.5\pi$ array

(d) Superdirective array

Figure 6.8: The space-time diagrams of inwards (dark blue part of the contour) and ourwards (yellow) energy flow along the x axis for (a) the single magnetic dipole, (b) the $\beta = 0$ non-superdirective array, (c) the $\beta = 0.5\pi$ non-superdirective array and (d) the superdirective array; The black dashed lines indicate the time frames presented in Figure 6.4∼6.7.

6.3 Energy Flow: SSRR and Two-SSRR Parasitic Arrays

In this section, the energy flow study is performed, based on CST simulation results, for a standard SSRR shown in Figure 5.22, three superdirective structures, namely the 'CC' structure, the 'CCEx' structure and the 'CCLr' structure, shown in Table 5.1 and 5.2, and a non-superdirective 'Near' structure shown in Figure 6.9. The 2D normalized far field average radiation energy patterns for these structures are plotted, using simulation data, and displayed in Figure 6.10.

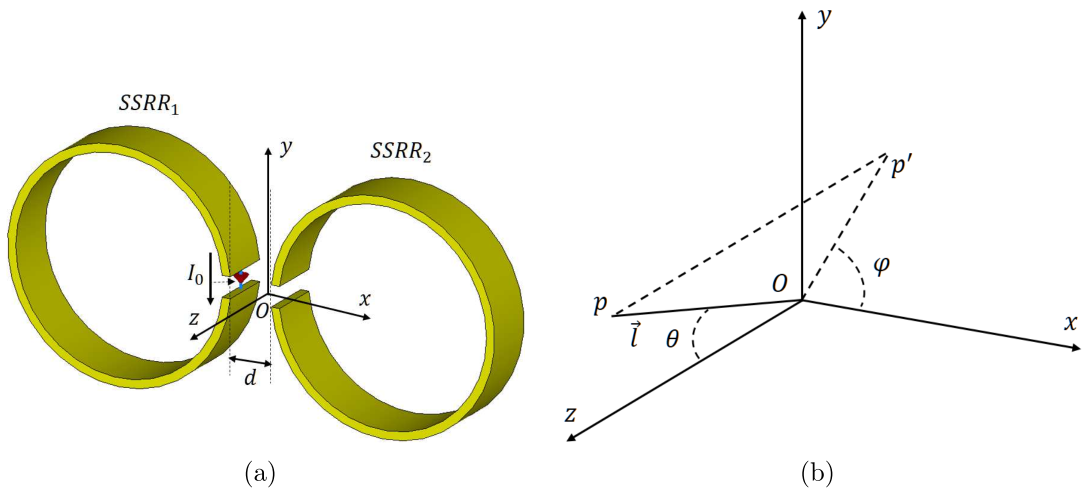

Figure 6.9: (a) The 'Near' structure and (b) the coordinate system for the energy flow analysis: here both the two elements are standard SSRRs shown in Figure 5.22, the separation distance between them $d = 4mm$; p is the observation point in far field.

Here for each of the three superdirective structures, the optimal elements' separation and the optimal operation frequency are specifically chosen for the structure's best directive performance, based on the CST simulation data presented in Section 5.3. For the 'CC' structure, the optimal separation distance is $4mm$ and the optimal frequency is $1.914GHz$, which leads to the structure's largest directivity value of 4.36. For the 'CCEx' structure, the optimal separation and frequency are respectively $5mm$ and $1.944GHz$, and the structure's largest directivity is 4.45. For the 'CCLr' structure, the largest directivity value of 5.06 is achieved with the optimal separation of $9mm$ and the optimal frequency of $1.239GHz$. The separation distance and the operation frequency for the 'Near' structure are set to be the same as those optimal values for the 'CC' structure, which results in a largest directivity of 1.852 in the endfire direction. For the single SSRR, the operation frequency is simply chosen as its resonant frequency, $1.957GHz$, leading to a largest directivity of 1.44 in the endfire direction.

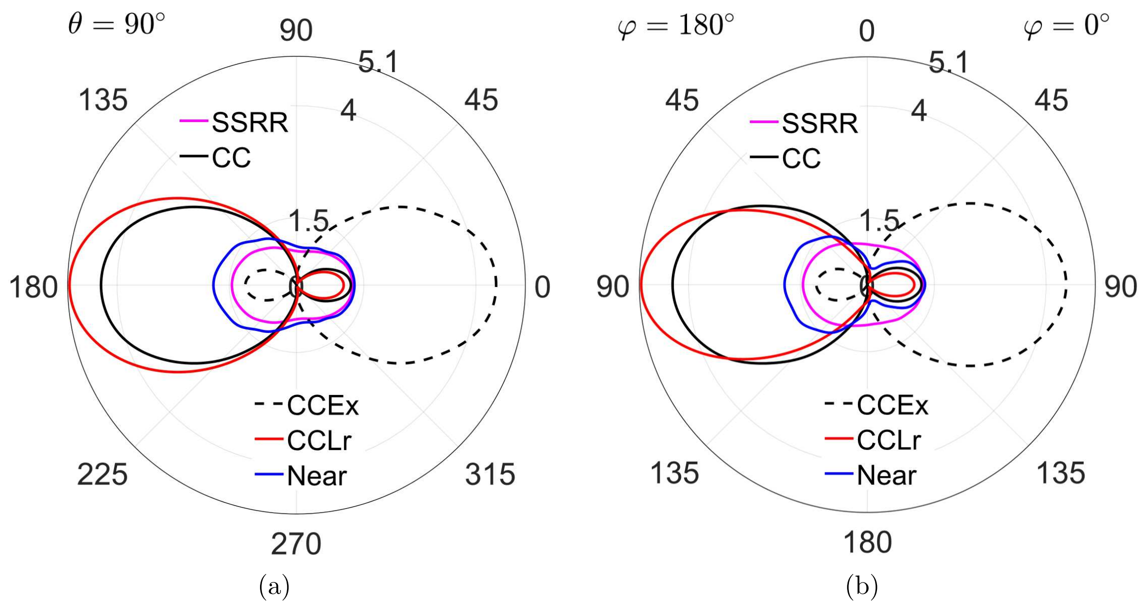

Figure 6.10: The 2D normalized far field radiation energy patterns for a standard SSRR ($D_m = 1.44$ for $1.957GHz$), the 'CC' structure ($D_m = 4.36$ for $1.914GHz$), the 'CCEx' structure ($D_m = 4.45$ for $1.944GHz$), the 'CCLr' structure ($D_m = 5.06$ for $1.239GHz$) and the 'Near' structure ($D_m = 1.852$ for $1.914GHz$): (a) xy plane patterns, (b) xz plane patterns; The radial axes of the polar plots indicate the far field directivity values.

The time-average energy flow in near field ($|\vec{l}\,| < \lambda$) for these structures are plotted using CST simulation data and presented in Figure 6.11. Unlike a single magnetic dipole, carrying a non-uniform current enables the single standard SSRR's time-average energy flow (see Figure 6.11(a)) to show a slightly preferential direction (negative x) and not to avoid z direction. The time-average energy flow of the 'CC' structure (Figure 6.11(b)) suggests this superdirective 'CC' structure has a similar radiating behaviour with that of a two-dipole superdirective array (Figure 6.3(d)). For the 'CCEx' structure, the time-average energy flow plot (Figure 6.11(c)) is almost the same as that for the 'CC' structure except the reverse of the preferential radiation direction (from the negative x direction to the positive x direction). This reverse is believed to be caused by a near π shift of two SSRRs' currents' phase difference, due to the reallocation of the excitation source. For the 'CCLr' structure (Figure 6.11(d)), even though its overall energy density within near field region is relatively low, the structure's energy flow shows a significantly stronger radiation preference in the negative x direction, compared with the case for the 'CC' structure. The relatively low energy density presented in Figure 6.11(d) results from the decrease in the radiation efficiency (see Table 5.2) caused by the enlarged passive SSRR element (see Table 5.1). A radiation preference in the negative x direction can also be noticed from the time-average energy flow of the 'Near' structue (Figure 6.11(e)) but it is apparently not strong enough for the structure to achieve superdirectivity. The color bar in Figure 6.11(f) presents a fixed range of the logarithm scaled energy density, which applies to all energy flow plots in this section (Section 6.3) except the space-time diagrams.

The time evolution of the instantaneous Poynting vectors of these SSRR structures are shown in Figure 6.12∼6.16. For either the single SSRR (Figure 6.12) or the 'Near' structure (Figure 6.16), the causal surface shows a slight distortion compared with the case for a single magnetic dipole (Figure 6.4). However for all the three superdirective structures ('CC', 'CCEx' and 'CCLr'), their causal surfaces are always strongly distorted within one time circle when they gradually move away from the radiating structures (Figure 6.13∼ 6.15). These strong distortions force more energy to radiate in one endfire direction and then cause the unidirectional endfire superdirectivity.

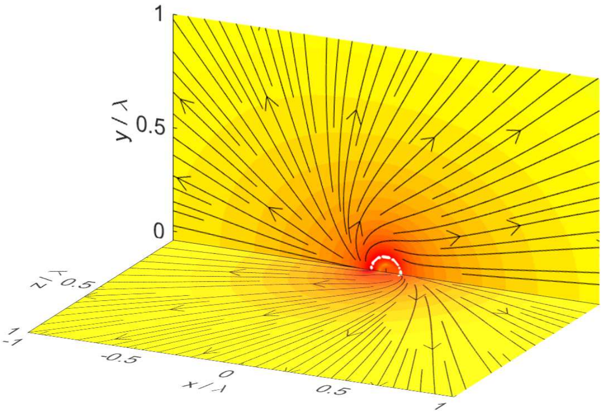

(a) Single SSRR

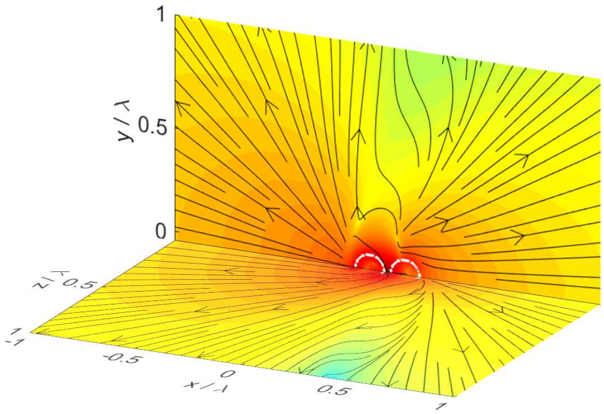

(b) CC

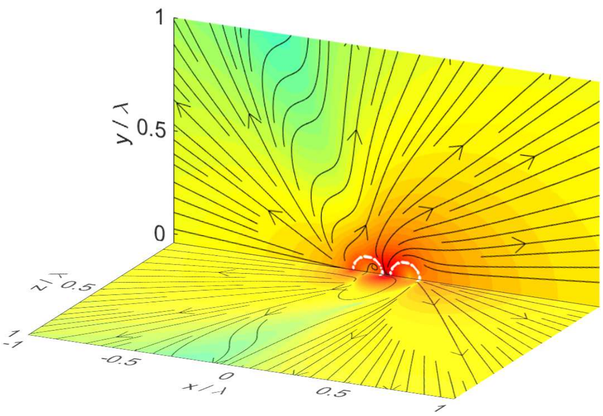

(c) CCEx

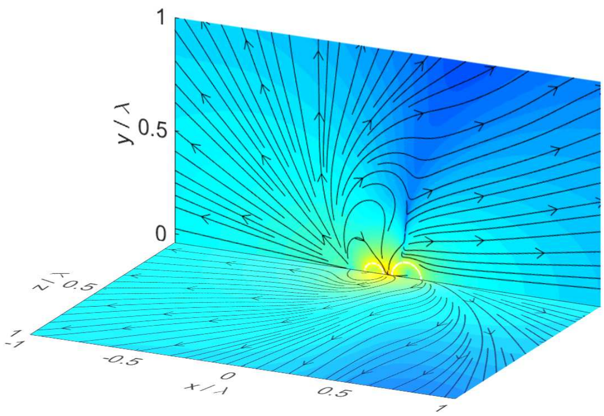

(d) CCLr

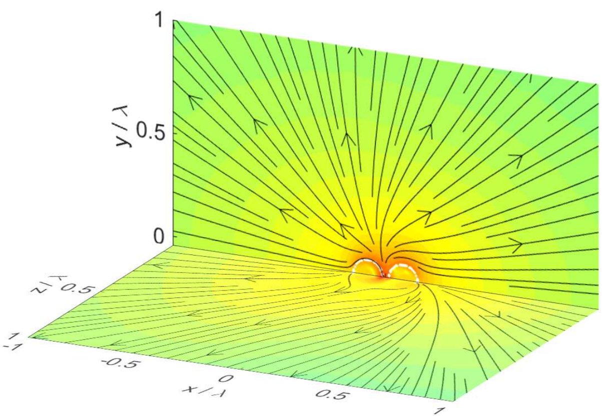

(e) Near

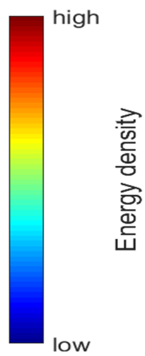

(f)

Figure 6.11: The time-average energy flow in near field region for (a) the SSRR, (b) the 'CC' structure, (c) the 'CCEx' structure, (d) the 'CCLr' structure and (e) the 'Near' structure; The color map shows the logarithmic scale of the time-average energy density as (f) the color bar indicates; The streamlines indicate the time-average Poynting vectors corresponding to the energy density.

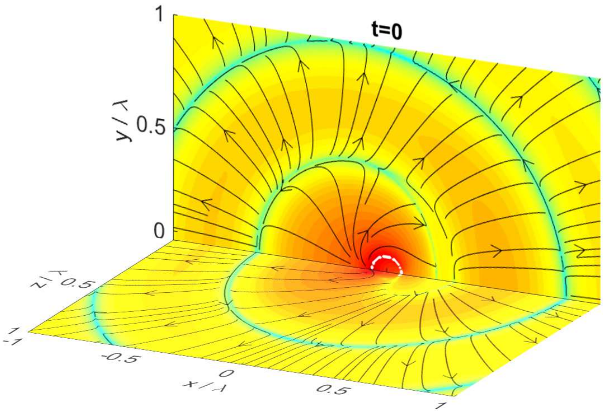

(a)

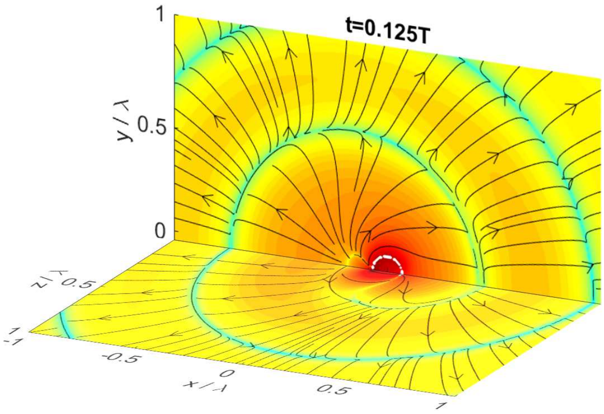

(b)

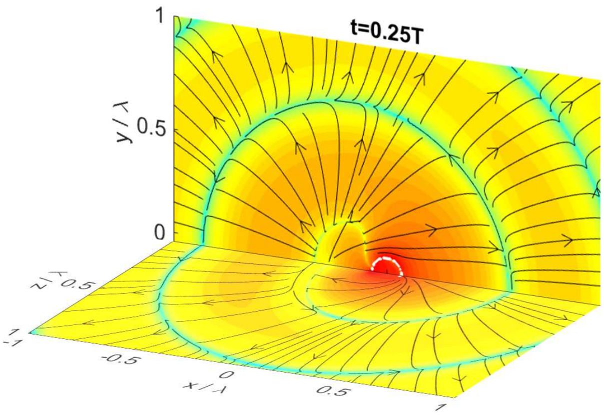

(c)

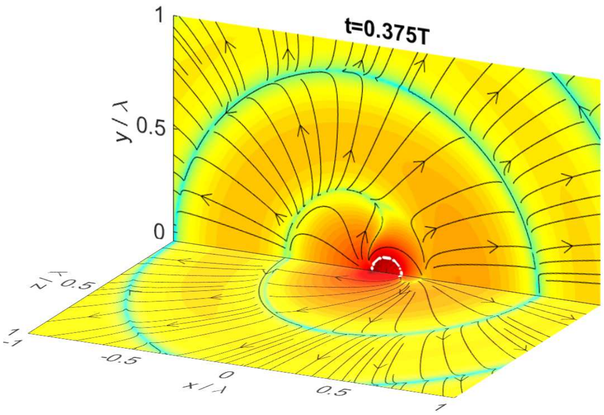

(d)

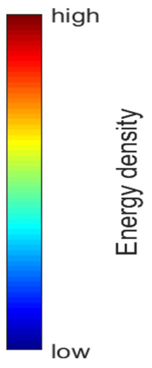

(e) Color bar

Figure 6.12: The instantaneous energy flow of the SSRR in near field region for four time frames: (a) $t = 0$, (b) $t = 0.125T$, (c) $t = 0.25T$ and (d) $t = 0.375T$; The colour map shows the logarithmic scale of the instantaneous energy density as (e) the colour bar indicates; The streamlines indicate the instantaneous Poynting vectors corresponding to the energy density.

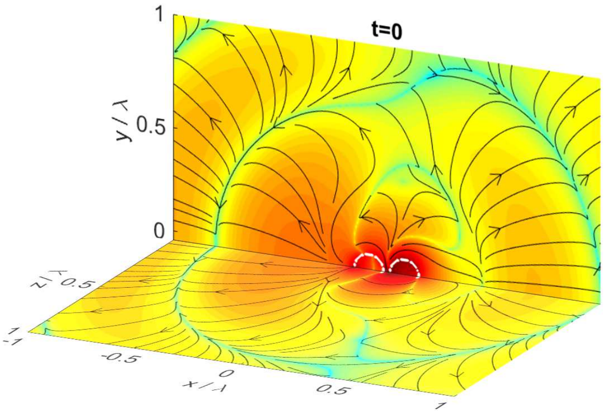

(a)

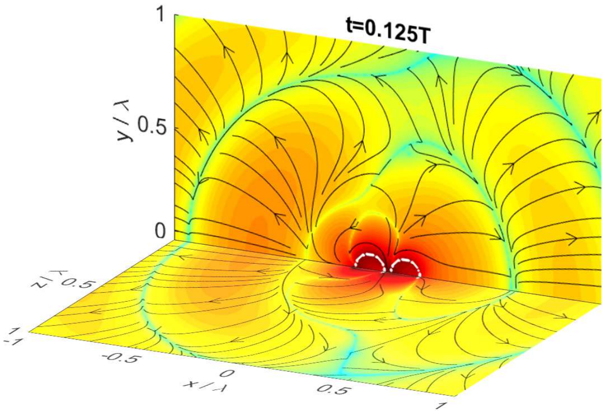

(b)

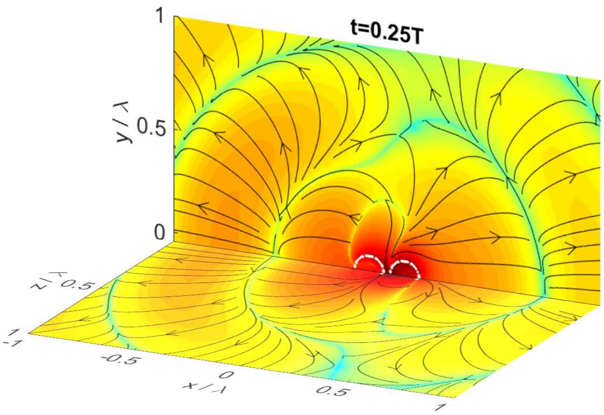

(c)

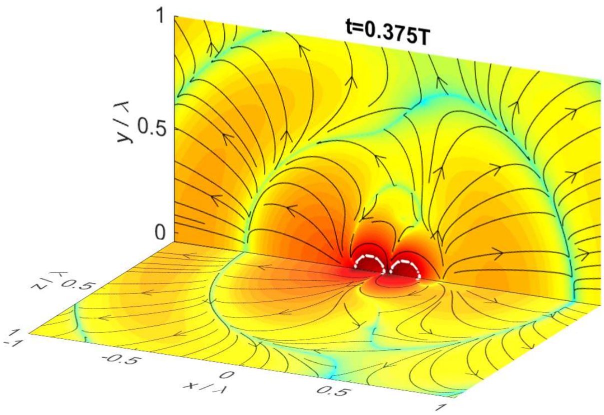

(d)

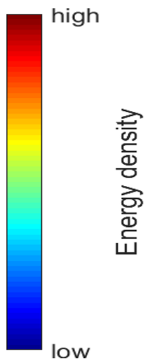

(e) Color bar

Figure 6.13: The instantaneous energy flow of the ‘CC’ structure in near field region for four time frames: (a) $t = 0$, (b) $t = 0.125T$, (c) $t = 0.25T$ and (d) $t = 0.375T$; The colour map shows the logarithmic scale of the instantaneous energy density as (e) the colour bar indicates; The streamlines indicate the instantaneous Poynting vectors corresponding to the energy density.

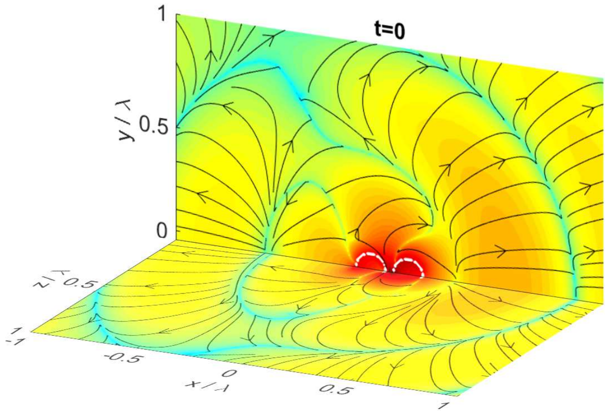

(a)

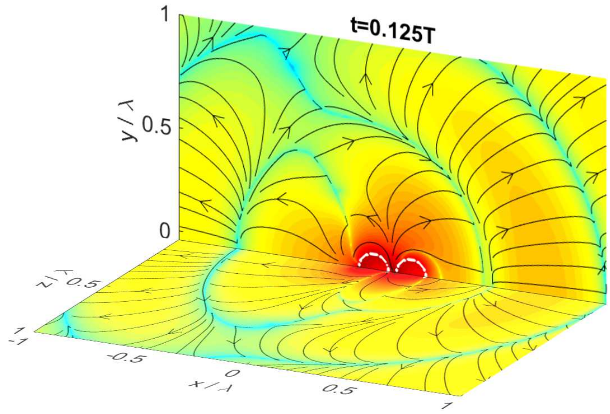

(b)

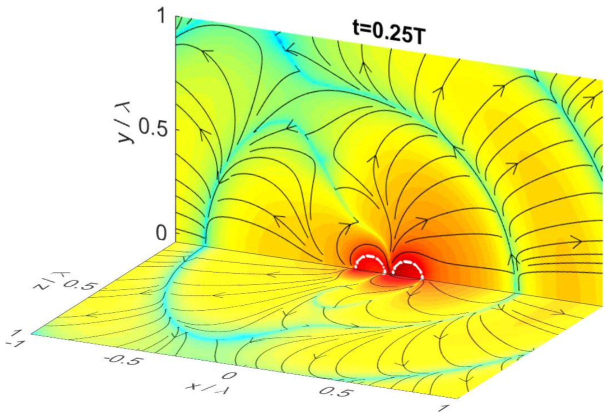

(c)

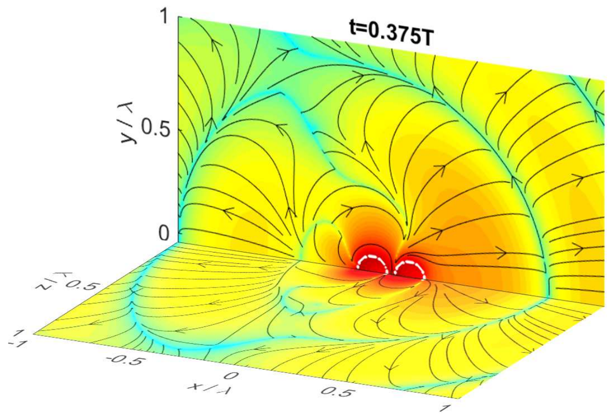

(d)

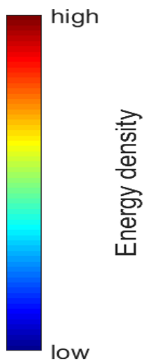

(e) Color bar

Figure 6.14: The instantaneous energy flow of the 'CCEx' structure in near field region for four time frames: (a) $t = 0$, (b) $t = 0.125T$, (c) $t = 0.25T$ and (d) $t = 0.375T$; The colour map shows the logarithmic scale of the instantaneous energy density as (e) the colour bar indicates; The streamlines indicate the instantaneous Poynting vectors corresponding to the energy density.

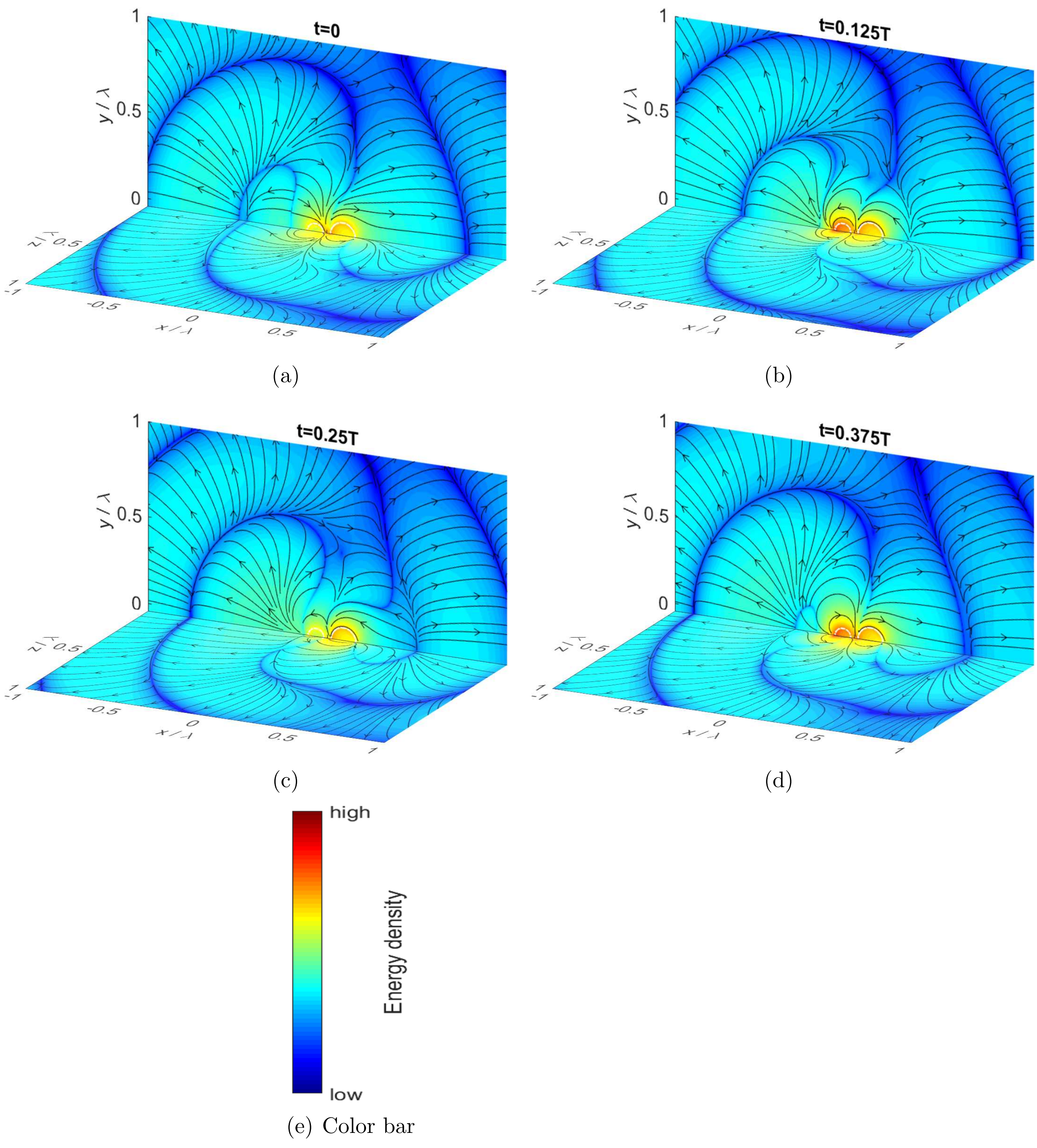

(a) (b) (c) (d)

(e) Color bar

Figure 6.15: The instantaneous energy flow of the 'CCLr' structure in near field region for four time frames: (a) $t = 0$, (b) $t = 0.125T$, (c) $t = 0.25T$ and (d) $t = 0.375T$; The colour map shows the logarithmic scale of the instantaneous energy density as (e) the colour bar indicates; The streamlines indicate the instantaneous Poynting vectors corresponding to the energy density.

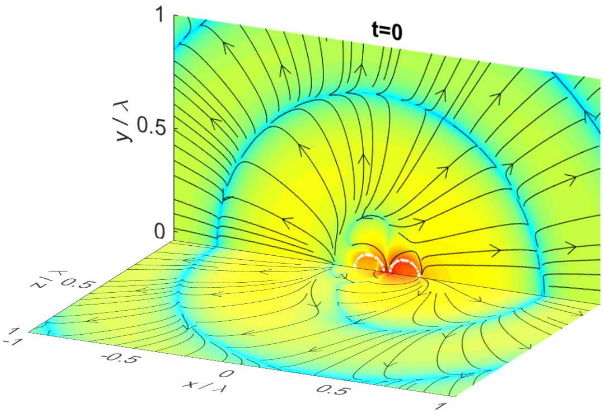

(a)

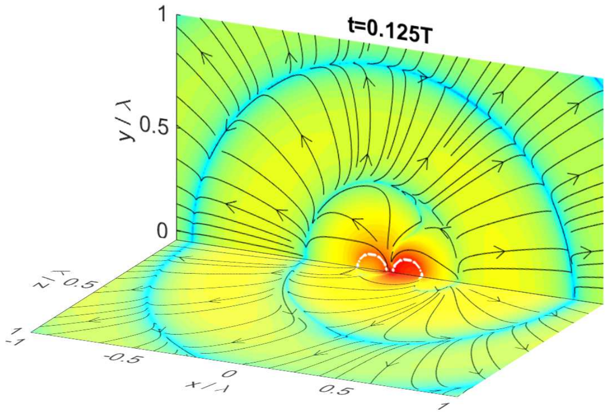

(b)

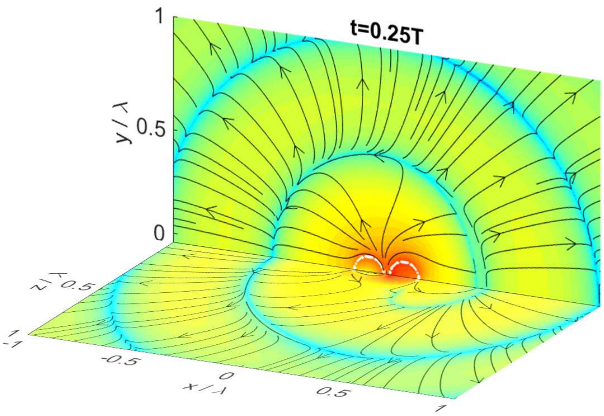

(c)

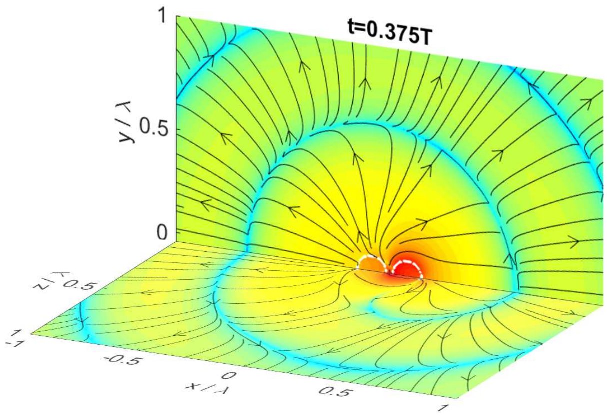

(d)

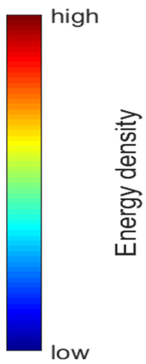

(e) Color bar

Figure 6.16: The instantaneous energy flow of the 'Near' structure in near field region for four time frames: (a) $t = 0$, (b) $t = 0.125T$, (c) $t = 0.25T$ and (d) $t = 0.375T$; The colour map shows the logarithmic scale of the instantaneous energy density as (e) the colour bar indicates; The streamlines indicate the instantaneous Poynting vectors corresponding to the energy density.

The space-time diagrams for the above five structures are shown in Figure 6.17. None of these diagrams presents a causal pair symmetry as Figure 6.8(a) (for a single magnetic dipole) shows. However, only the asymmetries shown in Figure 6.17(b) (for 'CC'), in Figure 6.17(c) (for 'CCEx') and in Figure 6.17(d) (for 'CCLr') are significant enough for these structures to achieve superdirectivity. In addition, for the 'CCLr' structure, the enlarged passive element also leads to that the energy flowing back to the radiating structure from the positive x direction is much more than that flowing back from the negative x direction, which also contributes to the structure's enhanced directive performance.

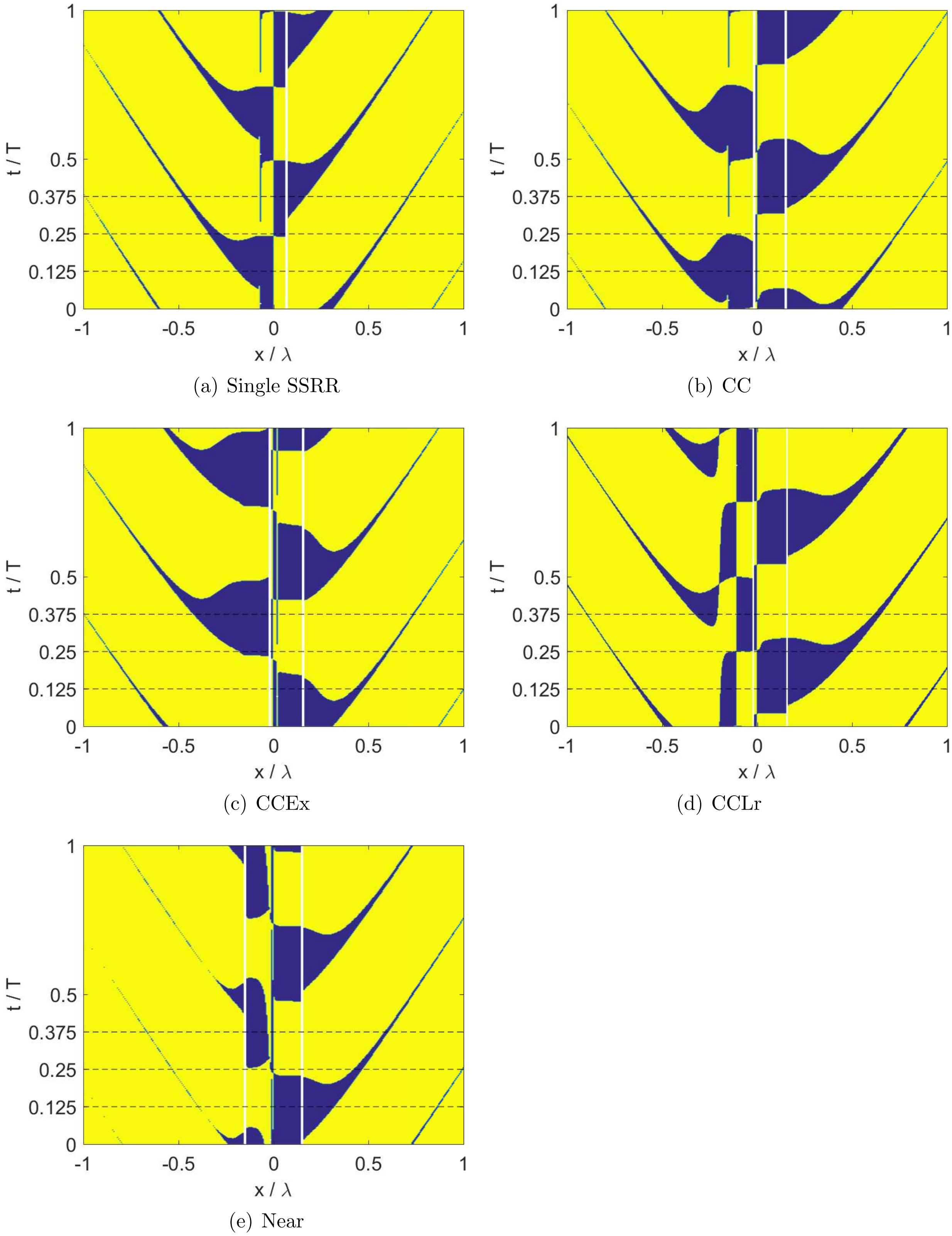

Figure 6.17: The space-time diagrams of inwards (dark blue part of the contour) and ourwards (yellow) energy flow along the x axis for (a) the single SSRR, (b) the 'CC' structure, (c) the 'CCEx' structure, (d) the 'CCLr' structure and (e) the 'Near' structure; The black dashed lines indicate the time frames presented in Figure 6.12∼6.16.

6.4 Conclusion

In summary, based on the near field energy flow study performed for magnetic dipole based structures (analytical results) and SSRR based structures (simulation results), the distortion of the causal surfaces, caused by the constructively and destructively interference of the fields from an array's two elements, is the main reason why endfie superdirectivity can happen.

Chapter 7

Summary

7.1 Conclusion

In summary, the work discussed in this dissertation explores a new design of model-supporting, simple, compact, robust and high efficiency superdirective antenna structures and the physical reason behind superdirectivity. Especially it focuses on building an analytical model for an electrically small two-element parasitic array of metamaterial elements (which can be used to analyse the array's currents' behaviours and to identify conditions for the array to achieve superdirectivity), studying and improving the model predicted superdirective structure, and visualizing the near field energy flow around superdirective structures. Simulation results have shown that the easy-to-use analytical model has successfully predicted a simple, compact, robust and usable high efficiency superdirective structure (the 'CC' structure). Based on simulation results, improved versions of the 'CC' structure have been identified and detailedly studied. Also with the help of causal surfaces, the physical reason behind the superdirectivity phenomenon has been finally recognized.

First, the study of electrically small two-element arrays shows that the largest directivity of an array of two identical standard SSRRs working around $f = 1.9GHz$

can only be lower than 5.

Second, a method of calculating a two-SSRR (initially two-NCLA) array's far field radiated energy, rigorously derived from Maxwell's Equations, combined with an equivalent circuit for a two-SSRR parasitic array, has formed a powerful but compact analytical model, which in principle allows to easily but accurately predict the far field radiation behaviours of an electrically small parasitic array of two SSRRs (the two SSRRs are not necessarily standard and identical), based on certain information of the array, namely the SSRRs' dimensions, the SSRRs' electrical components (L, C and R), the SSRRs' rotating orientation angles (α_1 and α_2), the two SSRRs's separation (d) and the array's operation frequency. Using this model, a simple, compact, robust and high efficiency superdirective structure (the 'CC' structure comprised of two standard SSRRs with $d = 4mm$ working at $1.914GHz$, achieving a directivity of 4.36) has been successfully predicted. Successfully building and applying the analytical model implies that it is possible to first build a compact analytical model to predict the potential outcomes, for the design process of a parasitic superdirective array, before starting simulations and experiments, which can significantly reduce the design time.

Third, according to CST simulation results, for two-SSRR parasitic superdirective structures (the 'CC' and its improved versions), characteristics of antenna performance (the maximum directivity, the optimal frequency, the superdirectivity bandwidth, the efficiency, the beamwidth and the Q factor) can be adjusted through changing the two elements' separation d. The simulation results also have shown that with optimal separations identified for all the studied superdirective structures' (the 'CC' and its improved versions) best directive performances: (a) Both the 'CC' and the 'CCEx' structure can provide large superdirective directivity values (for 'CC', 4.36 and for 'CCEx', 4.45) while sustain good performances in the superdirectivity bandwidth (for 'CC', 1.1% and for 'CCEx', 1.49%), the efficiency (for 'CC', 98.6%

and for 'CCEx', 99.1%) and the Q factor (for 'CC', 133.1 and for 'CCEx', 126.9), and the 'CCEx' structure shows slight improvement over the 'CC' in all respects. (b) Combining the 'CCDg' and the 'CCDgEx' might be helpful for certain application designs requiring stable alternating bidirectional superdirective radiation. (c) Either the 'CCLr' or the 'CCEe' can provide very large directivity values (for 'CCLr', 5.06 and for 'CCEe', 4.93), which are very close to the theoretical limit value (5.25) of a two-dipole array, at the cost of small superdirectivity bandwidths (for 'CCLr', 1.01% and for 'CCEe', 0.88%), low efficiencies (for 'CCLr', 81.4% and for 'CCEe', 89.2%) and high Q factors (for 'CCLr', 478.2 and for 'CCEe', 414.9). (d) These two-SSRR parasitic superdirective structures show better directive performance than the realistic two-element Yagi antennas do.

In the end, the near field energy flow study has been performed for magnetic dipole based structures (analytical results) and SSRR based structures (simulation results). It implies that the distortion of the causal surfaces, caused by the constructively and destructively interference of the fields from an array's two elements, is the main reason why endfie superdirectivity can happen.

7.2 Outlook

Practical superdiretive structures offer a promising future for sonar array signal processing. The advantages of simple, compact, robust and usable high efficiency superdirective arrays continuously inspire more interest in this field. As technology moves forward, increasing attention will be received and more applications of simple, compact, robust and usable high efficiency superdirective arrays will be discovered.

Limited by the equipments (anechoic chamber, whole space signal detector and so on) which potentially can be used for measuring the far field directivity of the superdirective arrays, relevant experimental measurements have not been included in the project. Appropriate equipments will possibly be purchased and installed in future. It is important to obtain reliable and comprehensive experimental data with suitable equipments, which will both further confirm the theoretical studies and facilitate the fabrications of superdirective antennas.

Further work on multiple working bands can be implemented through proportionally increasing or decreasing the whole structure's size (for any one of the studied superdirective structures). The working frequency is expected to move within a certain range without affecting the structure's performance, which will enable the superdirective structures to properly work for various applications in different frequency spectrums, leading to the versatility of the superdirectie structures. The lower and upper limit of the frequency range within which the working frequency change does not affect the antennas' superdirective performances is also worth exploring.

Additional research can be carried out focusing on developing a three-SSRR superdirective array. In order to identify conditions for this three-element array to achieve superdirectivity. The theoretical model developed in this research needs to be further extended by figuring out an equivalent circuit for such a three-element array, which should consider the mutual coupling between all the three elements. Extending the model may be complicated, but realizing a simple, compact, robust and usable high efficiency three-SSRR parasitic superdirective array can be very attractive.

Bibliography

[1] Y. Wang, Y. Yang, Z. He, Y. Han, and Y. Ma, "A general superdirectivity model for arbitrary sensor arrays," *EURASIP Journal on Advances in Signal Processing*, vol. 2015, no. 1, p. 68, 2015.

[2] G. J. Foschini and M. J. Gans, "On limits of wireless communications in a fading environment when using multiple antennas," *Wireless personal communications*, vol. 6, no. 3, pp. 311–335, 1998.

[3] G. G. Raleigh and J. M. Cioffi, "Spatio-temporal coding for wireless communication," *IEEE Transactions on communications*, vol. 46, no. 3, pp. 357–366, 1998.

[4] M. L. Morris, M. A. Jensen, and J. W. Wallace, "Superdirectivity in mimo systems," *IEEE Transactions on Antennas and Propagation*, vol. 53, no. 9, pp. 2850–2857, 2005.

[5] "Ieee standard for definitions of terms for antennas," *IEEE Std 145-2013 (Revision of IEEE Std 145-1993)*, pp. 1–50, March 2014.

[6] N. Yaru, "A note on super-gain antenna arrays," *Proceedings of the IRE*, vol. 39, no. 9, pp. 1081–1085, 1951.

[7] S. Egashira and E. Nishiyama, “Stacked microstrip antenna with wide bandwidth and high gain,” *IEEE Transactions on Antennas and Propagation*, vol. 44, no. 11, pp. 1533–1534, 1996.

[8] D. Li, Z. Szabo, X. Qing, E.-P. Li, and Z. N. Chen, “A high gain antenna with an optimized metamaterial inspired superstrate,” *IEEE transactions on antennas and propagation*, vol. 60, no. 12, pp. 6018–6023, 2012.

[9] A. D. Yaghjian, T. H. O’Donnell, E. E. Altshuler, and S. R. Best, “Electrically small supergain end-fire arrays,” *Radio Science*, vol. 43, no. 3, 2008.

[10] C. A. Balanis, *Antenna theory: analysis and design*. John Wiley & Sons, 2012.

[11] W. L. Stutzman and G. A. Thiele, *Antenna theory and design*. John Wiley & Sons, 2012.

[12] L. V. John and L. Volakis, “Antenna engineering handbook,” *New York: McGraw-Hill*, 2007.

[13] A. W. Rudge, ed., *Handbook of Antenna Design, Vol. 2*. Electromagnetic Waves, Institution of Engineering and Technology, 1983.

[14] M. Dawoud and A. Anderson, “Superdirectivity with appreciable bandwidth in arrays of radiating elements fed by microwave transistors,” in *Microwave Conference, 1974. 4th European*, pp. 278–282, IEEE, 1974.

[15] H. Salt, “Practical realization of superdirective arrays,” *Radio and Electronic Engineer*, vol. 47, no. 4, pp. 143–156, 1977.

[16] L. Yuan, D. Weibo, and X. Rongqing, “A design of superdirective endfire array in hf band,” in *Radio Science Conference, 2004. Proceedings. 2004 Asia-Pacific*, pp. 74–77, IEEE, 2004.

[17] E. Shamonina and L. Solymar, "Superdirectivity by virtue of coupling between meta-atoms," in *Advanced Electromagnetic Materials in Microwaves and Optics (METAMATERIALS), 2013 7th International Congress on*, pp. 97–99, IEEE, 2013.

[18] C. W. Oseen, "Die einsteinsche nadelstichstrahlung und die maxwellschen gleichungen," *Annalen der Physik*, vol. 374, no. 19, pp. 202–204, 1922.

[19] G. de Villiers and P. E. R., *The Limits of Resolution.* Taylor & Francis Group, 2017.

[20] W. W. Hansen and J. Woodyard, "A new principle in directional antenna design," *Proceedings of the Institute of Radio Engineers*, vol. 26, no. 3, pp. 333–345, 1938.

[21] K. Franz, "The gain and the (rudenberg)'absorption surfaces' of large directive arrays," *Hochfreq. Elektroakust.*, vol. 54, p. 198, 1939.

[22] S. A. Schelkunoff, "A mathematical theory of linear arrays," *Bell Labs Technical Journal*, vol. 22, no. 1, pp. 80–107, 1943.

[23] M. Uzsoky and L. Solymar, "Theory of super-directive linear arrays," *Acta Physica Academiae Scientiarum Hungaricae*, vol. 6, no. 2, pp. 185–205, 1956.

[24] C. Bouwkamp and N. De Bruijn, "The problem of optimum antenna current distribution," *Philips Res. Rep.*, vol. 1, no. 2, pp. 135–158, 1946.

[25] L. La Paz and G. A. Miller, "Optimum current distributions on vertical antennas," *Proceedings of the IRE*, vol. 31, no. 5, pp. 214–232, 1943.

[26] G. T. Di Francia, "Resolving power and information," *Josa*, vol. 45, no. 7, pp. 497–501, 1955.

[27] A. Bloch, R. Medhurst, and S. Pool, “A new approach to the design of super-directive aerial arrays,” *Proceedings of the IEE-Part III: Radio and Communication Engineering*, vol. 100, no. 67, pp. 303–314, 1953.

[28] D. Reid, “The gain of an idealized yagi array,” *Journal of the Institution of Electrical Engineers-Part IIIA: Radiolocation*, vol. 93, no. 3, pp. 564–566, 1946.

[29] A. Uzkov, “An approach to the problem of optimum directive antenna design,” in *Comptes Rendus (Doklady) de lAcademie des Sciences de lURSS*, vol. 53, pp. 35–38, 1946.

[30] O. S. Kim, S. Pivnenko, and O. Breinbjerg, “Superdirective magnetic dipole array as a first-order probe for spherical near-field antenna measurements,” *IEEE Transactions on antennas and propagation*, vol. 60, no. 10, pp. 4670–4676, 2012.

[31] A. Haskou, A. Sharaiha, S. Collardey, M. Pigeon, and K. Mahdjoubi, “A design methodology for electrically small superdirective antenna arrays,” in *Antennas and Propagation Conference (LAPC), 2014 Loughborough*, pp. 405–409, IEEE, 2014.

[32] C. L. Dolph, “A current distribution for broadside arrays which optimizes the relationship between beam width and side-lobe level,” *Proceedings of the IRE*, vol. 34, no. 6, pp. 335–348, 1946.

[33] W. H. Kummer, “Basic array theory,” *Proceedings of the IEEE*, vol. 80, no. 1, pp. 127–140, 1992.

[34] R. C. Hansen, “Array pattern control and synthesis,” *Proceedings of the IEEE*, vol. 80, no. 1, pp. 141–151, 1992.

[35] H. J. Riblet, "Discussion on 'a current distribution for broadside arrays which optimizes the relationship between beam width and side-lobe level'," *Proceedings of the IRE*, vol. 35, pp. 489–492, 1947.

[36] H. Salzer, "Note on the fourier coefficients for chebyshev patterns," *Proceedings of the IEE-Part C: Monographs*, vol. 103, no. 4, pp. 286–288, 1956.

[37] M. Dawoud and A. Anderson, "Design of superdirective arrays with high radiation efficiency," *IEEE Transactions on Antennas and Propagation*, vol. 26, no. 6, pp. 819–823, 1978.

[38] R. H. DuHamel, "Optimum patterns for endfire arrays," *Proceedings of the IRE*, vol. 41, no. 5, pp. 652–659, 1953.

[39] C. J. Drane, "Derivation of excitation coefficients for chebyshev arrays," in *Proceedings of the Institution of Electrical Engineers*, vol. 110, pp. 1755–1758, IET, 1963.

[40] R. J. Stegen, "Excitation coefficients and beamwidths of tschebyscheff arrays," *Proceedings of the IRE*, vol. 41, no. 11, pp. 1671–1674, 1953.

[41] R. Hansen, "Directivity of chebyshev arrays," *IEEE Transactions on Antennas and Propagation*, vol. 18, no. 6, pp. 815–818, 1970.

[42] H. A. Wheeler, "Fundamental limitations of small antennas," *Proceedings of the IRE*, vol. 35, no. 12, pp. 1479–1484, 1947.

[43] H. A. Wheeler, "The radiansphere around a small antenna," *Proceedings of the IRE*, vol. 47, no. 8, pp. 1325–1331, 1959.

[44] L. J. Chu, "Physical limitations of omnidirectional antennas," *Journal of Applied Physics*, vol. 19, no. 12, pp. 1163–1175, 1948.

[45] R. F. Harrington, "Effect of antenna size on gain, bandwidth, and efficiency," *J. Res. Nat. Bur. Stand*, vol. 64, no. 1, pp. 1–12, 1960.

[46] R. C. Hansen, "Fundamental limitations in antennas," *Proceedings of the IEEE*, vol. 69, no. 2, pp. 170–182, 1981.

[47] Y. Lo, S. Lee, and Q. Lee, "Optimization of directivity and signal-to-noise ratio of an arbitrary antenna array," *Proceedings of the IEEE*, vol. 54, no. 8, pp. 1033–1045, 1966.

[48] C. Lin, D. Nyquist, and K. Chen, "Parasitic array of two loaded short antennas," *IEEE Transactions on Antennas and Propagation*, vol. 21, no. 6, pp. 852–855, 1973.

[49] E. Newman, J. Richmond, and C. Walter, "Superdirective receiving arrays," *IEEE Transactions on Antennas and Propagation*, vol. 26, no. 5, pp. 629–635, 1978.

[50] E. Newman and M. Schrote, "A wide-band electrically small superdirective array," *IEEE Transactions on Antennas and Propagation*, vol. 30, no. 6, pp. 1172–1176, 1982.

[51] M. Dawoud, "Scanning properties of superdirective antenna arrays," in *Antennas and Propagation, 1993., Eighth International Conference on*, pp. 694–697, IET, 1993.

[52] H. Cox, R. Zeskind, and T. Kooij, "Practical supergain," *IEEE Transactions on Acoustics, Speech, and Signal Processing*, vol. 34, no. 3, pp. 393–398, 1986.

[53] V. V. Veremy and V. P. Shestopalov, "Superdirective antenna with passive resonant reflector," *Radio Science*, vol. 26, no. 2, pp. 631–636, 1991.

[54] V. Veremey, "Superdirective antennas with passive reflectors," *IEEE Antennas and Propagation Magazine*, vol. 37, no. 2, pp. 16–27, 1995.

[55] V. V. Veremey and R. Mittra, "Scattering from structures formed by resonant elements," *IEEE Transactions on antennas and propagation*, vol. 46, no. 4, pp. 494–501, 1998.

[56] S. Bokhari, H. Smith, J. Mosig, J. Zurcher, and F. Gardiol, "Superdirective antenna array of printed parasitic elements," *Electronics Letters*, vol. 28, no. 14, pp. 1332–1334, 1992.

[57] D. K. Cheng, "Gain optimization for yagi-uda arrays," *IEEE Antennas and Propagation Magazine*, vol. 33, no. 3, pp. 42–46, 1991.

[58] K. Itoh, O. Ishii, Y. Nagai, N. Suzuki, Y. Kimachi, and O. Michikami, "Two-element superdirective array antenna composed of high-tc superconducting small helical radiators," *Journal of superconductivity*, vol. 5, no. 5, pp. 485–490, 1992.

[59] W. Tager, "Near field superdirectivity (nfsd)," in *Acoustics, Speech and Signal Processing, 1998. Proceedings of the 1998 IEEE International Conference on*, vol. 4, pp. 2045–2048, IEEE, 1998.

[60] R. Haviland, "Supergain antennas: possibilities and problems," *IEEE Antennas and Propagation Magazine*, vol. 37, no. 4, pp. 13–26, 1995.

[61] D. P. Scholnik and J. O. Coleman, "Superdirectivity and snr constraints in wideband array-pattern design," in *Radar Conference, 2001. Proceedings of the 2001 IEEE*, pp. 181–186, IEEE, 2001.

[62] E. Shamonina, K. Ringhofer, and L. Solymar, "Configurations optimizing the directivity of planar arrays," *AEU-International Journal of Electronics and Communications*, vol. 56, no. 2, pp. 115–119, 2002.

[63] H. J. Chaloupka, X. Wang, and J. Coetzee, "A superdirective 3-element array for adaptive beamforming," *Microwave and Optical Technology Letters*, vol. 36, no. 6, pp. 425–430, 2003.

[64] N. W. Bikhazi and M. A. Jensen, "The relationship between antenna loss and superdirectivity in mimo systems," *IEEE transactions on wireless communications*, vol. 6, no. 5, 2007.

[65] S. R. Best, E. E. Altshuler, A. D. Yaghjian, J. M. McGinthy, and T. H. O'Donnell, "An impedance-matched 2-element superdirective array," *IEEE Antennas and Wireless Propagation Letters*, vol. 7, pp. 302–305, 2008.

[66] S. Mondal, "Two element superdirective array of shorted planar inverted cone antenna,"

[67] Y. Ma, Y. Yang, Z. He, K. Yang, C. Sun, and Y. Wang, "Theoretical and practical solutions for high-order superdirectivity of circular sensor arrays," *IEEE Transactions on Industrial Electronics*, vol. 60, no. 1, pp. 203–209, 2013.

[68] E. E. Altshuler, T. H. ODonnell, and A. D. Yaghjian, "A superdirective array using very small genetic antennas," *Digest, URSI General Assembly, Maestricht*, 2002.

[69] E. E. Altshuler, T. H. O'Donnell, A. D. Yaghjian, and S. R. Best, "A monopole superdirective array," *IEEE Transactions on Antennas and Propagation*, vol. 53, no. 8, pp. 2653–2661, 2005.

[70] T. H. O'Donnell and A. D. Yaghjian, "Electrically small superdirective arrays using parasitic elements," in *Antennas and Propagation Society International Symposium 2006, IEEE*, pp. 3111–3114, IEEE, 2006.

[71] T. H. O'Donnell, A. D. Yaghjian, and E. Altshuler, "Frequency optimization of parasitic superdirective two element arrays," in *Antennas and Propagation Society International Symposium, 2007 IEEE*, pp. 3932–3935, IEEE, 2007.

[72] I. Liberal, I. Ederra, R. Gonzalo, and R. W. Ziolkowski, "Superbackscattering antenna arrays," *IEEE Transactions on Antennas and Propagation*, vol. 63, no. 5, pp. 2011–2021, 2015.

[73] J. B. Pendry, A. J. Holden, D. Robbins, and W. Stewart, "Magnetism from conductors and enhanced nonlinear phenomena," *IEEE transactions on microwave theory and techniques*, vol. 47, no. 11, pp. 2075–2084, 1999.

[74] D. R. Smith, W. J. Padilla, D. Vier, S. C. Nemat-Nasser, and S. Schultz, "Composite medium with simultaneously negative permeability and permittivity," *Physical review letters*, vol. 84, no. 18, p. 4184, 2000.

[75] S. Enoch, G. Tayeb, P. Sabouroux, N. Guérin, and P. Vincent, "A metamaterial for directive emission," *Physical Review Letters*, vol. 89, no. 21, p. 213902, 2002.

[76] K. Buell, H. Mosallaei, and K. Sarabandi, "Metamaterial insulator enabled superdirective array," *IEEE transactions on antennas and propagation*, vol. 55, no. 4, pp. 1074–1085, 2007.

[77] A. Alù and N. Engheta, "Enhanced directivity from subwavelength infrared/optical nano-antennas loaded with plasmonic materials or metamaterials," *IEEE Transactions on Antennas and Propagation*, vol. 55, no. 11, pp. 3027–3039, 2007.

[78] A. D. Yaghjian, "Increasing the supergain of electrically small antennas using metamaterials," in *Antennas and Propagation, 2009. EuCAP 2009. 3rd European Conference on*, pp. 858–860, IEEE, 2009.

[79] T. Kokkinos and A. P. Feresidis, "Electrically small superdirective endfire arrays of metamaterial-inspired low-profile monopoles," *IEEE Antennas and Wireless Propagation Letters*, vol. 11, pp. 568–571, 2012.

[80] A. Ludwig, C. D. Sarris, and G. V. Eleftheriades, "Metascreen-based superdirective antenna in the optical frequency regime," *Physical review letters*, vol. 109, no. 22, p. 223901, 2012.

[81] E. Shamonina, V. Kalinin, K. Ringhofer, and L. Solymar, "Magnetoinductive waves in one, two, and three dimensions," *Journal of Applied Physics*, vol. 92, no. 10, pp. 6252–6261, 2002.

[82] E. Shamonina and L. Solymar, "Superdirective meta-molecules," in *Advanced Electromagnetic Materials in Microwaves and Optics (METAMATERIALS), 2014 8th International Congress on*, pp. 268–270, IEEE, 2014.

[83] B. Sentucq, A. Sharaiha, and S. Collardey, "Superdirective metamaterial-inspired electrically small antenna arrays," in *Antennas and Propagation (EuCAP), 2013 7th European Conference on*, pp. 151–155, IEEE, 2013.

[84] A. Haskou, A. Clemente, A. Sharaiha, C. Delaveaud, S. Collardey, and L. Rudant, "Ultra-compact superdirective two-and three-element linear arrays," in *The 3rd Advanced Electromagnetics Symposium (AES2014)*, p. 105, 2014.

[85] A. Haskou, A. Sharaiha, and S. Collardey, "Design of small parasitic loaded superdirective end-fire antenna arrays," *IEEE Transactions on Antennas and Propagation*, vol. 63, no. 12, pp. 5456–5464, 2015.

[86] S. Dakhli, H. Rmili, K. Mahdjoubi, J.-M. Floch, and F. Choubani, "Analysis of a compact and superdirective metamaterial-inspired monopole antenna," *International Journal of Antennas and Propagation*, vol. 2014, 2014.

[87] M. Gupta and J. Saxena, "Superdirective patch antenna array using metamaterial," in *Electronics, Computing and Communication Technologies (IEEE CONECCT), 2014 IEEE International Conference on*, pp. 1–6, IEEE, 2014.

[88] H. Matzner and K. T. McDonald, "Isotropic radiators," *arXiv preprint physics/0312023*, 2003.

[89] J. H. Poynting, "On the transfer of energy in the electromagnetic field," *Philosophical Transactions of the Royal Society of London*, vol. 175, pp. 343–361, 1884.

[90] I. S. Grant and W. R. Phillips, *Electromagnetism.* John Wiley & Sons, 2013.

[91] D. J. Griffiths and R. College, *Introduction to electrodynamics*, vol. 3. prentice Hall Upper Saddle River, NJ, 1999.

[92] L. Solymar, "Lectures on electromagnetic theory: a short course for engineers," *Oxford and New York, Oxford University Press, 1976. 251 p*, vol. 1, p. 141, 1976.

[93] E. Shamonina and L. Solymar, "Maximum directivity of arbitrary dipole arrays," *IET Microwaves, Antennas & Propagation*, vol. 9, no. 2, pp. 101–107, 2015.

[94] R. C. Hansen and R. E. Collin, *Small antenna handbook.* John Wiley & Sons, 2011.

[95] R. Bancroft, "Fundamental dimension limits of antennas," *Centurion Wireless Technologies*, 2002.

[96] Y. Urzhumov and D. R. Smith, "Metamaterial-enhanced coupling between magnetic dipoles for efficient wireless power transfer," *Physical Review B*, vol. 83, no. 20, p. 205114, 2011.

[97] E. Tatartschuk, N. Gneiding, F. Hesmer, A. Radkovskaya, and E. Shamonina, "Mapping inter-element coupling in metamaterials: Scaling down to infrared," *Journal of Applied Physics*, vol. 111, no. 9, p. 094904, 2012.

[98] L. Solymar and E. Shamonina, *Waves in metamaterials.* Oxford University Press, 2009.

[99] F. Richard, R. Leighton, and M. Sands, "The feynman lectures on physics (the new millennium edition)," *Reading: Addison-Wesley Publishing Company*, 2010.

[100] J. D. Jackson, *Classical electrodynamics.* Wiley, 1999.

[101] L. Urankar, "Vector potential and magnetic field of current-carrying finite arc segment in analytical form, part i: Filament approximation," *IEEE Transactions on magnetics*, vol. 16, no. 5, pp. 1283–1288, 1980.

[102] J. Allen and S. Segre, "The electric field in single-turn and multi-sector coils," *Il Nuovo Cimento (1955-1965)*, vol. 21, no. 6, pp. 980–987, 1961.

[103] O. Sydoruk, E. Tatartschuk, E. Shamonina, and L. Solymar, "Analytical formulation for the resonant frequency of split rings," *Journal of Applied Physics*, vol. 105, no. 1, p. 014903, 2009.

[104] N. Gneiding, O. Zhuromskyy, E. Shamonina, and U. Peschel, "Circuit model optimization of a nano split ring resonator dimer antenna operating in infrared spectral range," *Journal of Applied Physics*, vol. 116, no. 16, p. 164311, 2014.

[105] G. V. Eleftheriades and K. G. Balmain, *Negative-refraction metamaterials: fundamental principles and applications.* John Wiley & Sons, 2005.

[106] G. S. Smith, "Loop antennas," *Antenna Engineering Handbook*, pp. 5–13, 1984.

[107] D. Kajfez and A. Z. Elsherbeni, "Determination of antenna q from the reflection-coefficient data [antenna designer's notebook]," *IEEE Antennas and Propagation Magazine*, vol. 55, no. 4, pp. 154–162, 2013.

[108] E. B. Rosa and F. W. Grover, *Formulas and tables for the calculation of mutual and self-inductance.* No. 169, US Government Printing Office, 1948.

[109] F. W. Grover, *Additions to the Formulas for the Calculation of Mutual and Self Inductance.* US Government Printing Office, 1918.

[110] M. O. T. Release, "The mathworks, inc., ndtick, mdssdchusetts, unitea stdtes.lsqcurvefit solver," 2012.

[111] C. R. Paul, *Fundamentals of electric circuit analysis.* Wiley, 2001.

[112] C. M. STUDIO and U. M. Version, "Sep. 2008, cst ag, darmstadt, germany," 2009.

[113] H. E. Knoepfel, *Magnetic fields: a comprehensive theoretical treatise for practical use.* John Wiley & Sons, 2008.

[114] G. E. Owen, *Introduction to electromagnetic theory.* Courier Corporation, 2003.

[115] D. A. Powell, M. Lapine, M. V. Gorkunov, I. V. Shadrivov, and Y. S. Kivshar, "Metamaterial tuning by manipulation of near-field interaction," *Physical Review B*, vol. 82, no. 15, p. 155128, 2010.

[116] L. Foged, A. Giacomini, L. Duchesne, E. Leroux, L. Sassi, and J. Mollet, "Advanced modelling and measurements of wideband horn antennas," in *Antenna*

Technology and Applied Electromagnetics [ANTEM 2005], 11th International Symposium on, pp. 1–4, IEEE, 2005.

[117] R. Dickie, R. Cahill, H. Gamble, V. Fusco, P. Huggard, B. Moyna, M. Oldfield, N. Grant, and P. De Maagt, "Polarisation independent bandpass fss," *Electronics Letters*, vol. 43, no. 19, pp. 1013–1015, 2007.

[118] R. Dickie, R. Cahill, H. Gamble, V. Fusco, P. Huggard, B. Moyna, M. Oldfield, N. Grant, and P. De Maagt, "Polarisation independent submillimetre wave annular slot frequency selective surface," 2007.

[119] N. Pohl, "A dielectric lens antenna with enhanced aperture efficiency for industrial radar applications," in *Antennas and Propagation (MECAP), 2010 IEEE Middle East Conference on*, pp. 1–5, IEEE, 2010.

[120] M. Troscher, "3 d emc/emi simulation of automotive multimedia systems," *Microwave Journal*, vol. 54, no. 7, pp. 34–38, 2011.

[121] "3D EM Simulation in the Design Flow of High-Speed Multi-Pin Connectors." `https://www.cst.com/solutions/article/3d-em-simulation-in-the-design-flow-of-high-speed-multi-pin-connectors`, 2017. [Online; Accessed: 31/10/2017].

[122] "3D Full Wave Cross-Talk Simulation of Multilayer PCB." `https://www.cst.com/solutions/article/3d-full-wave-cross-talk-simulation-of-multilayer-pcb`, 2017. [Online; Accessed: 31/10/2017].

[123] "A Dual-Mode Conical Horn Antenna for Rotationally Symmetric Beam." `https://www.cst.com/solutions/article/a-dual-mode-conical-horn-antenna-for-rotationally-symmetric-beam`, 2017. [Online; Accessed: 31/10/2017].

[124] "A Unit Cell Model of a Single Periodic Waveguide Phased-Array Antenna." `https://www.cst.com/solutions/article/a-unit-cell-model-of-a-single-periodic-waveguide-phased-array-antenna`, 2017. [Online; Accessed: 31/10/2017].

[125] "Airbus Defence and Space Analyzes EMC Test Chambers Using CST STUDIO SUITE." `https://www.cst.com/solutions/article/airbus-defence-and-space-analyzes-emc-test-chambers-using-cst-studio-suite`, 2017. [Online; Accessed: 31/10/2017].

[126] "CST MICROWAVE STUDIO Technical Specification." `https://www.cst.com/products/cstmws/technicalspecification`, 2017. [Online; Accessed: 31/10/2017].

[127] T. Weiland, "A discretization method for the solution of maxwells equations for six-component fields, electronics and communication (aeu), vol. 31 (1977)," *Google Scholar*, p. 116.

[128] S. Y. Elnaggar, R. J. Tervo, and S. M. Mattar, "General expressions and physical origin of the coupling coefficient of arbitrary tuned coupled electromagnetic resonators," *Journal of Applied Physics*, vol. 118, no. 19, p. 194901, 2015.

[129] J.-S. G. Hong and M. J. Lancaster, *Microstrip filters for RF/microwave applications*, vol. 167. John Wiley & Sons, 2004.

[130] S. Y. Elnaggar, R. J. Tervo, and S. M. Mattar, "Energy coupled mode theory for electromagnetic resonators," *IEEE Transactions on Microwave Theory and Techniques*, vol. 63, no. 7, pp. 2115–2123, 2015.

[131] R. Fitzpatrick, *Maxwells Equations and the Principles of Electromagnetism*. Jones & Bartlett Publishers, 2008.

[132] D. I. P. Birkner, "Optimization of the shape of a toroid with a non-idealized distribution of the magnetic field," *Archiv für Elektrotechnik*, vol. 75, no. 3, pp. 179–188, 1992.

[133] J. C. Whitaker, *The electronics handbook, second edition.* Crc Press, 2005.

[134] C. A. Balanis, *Modern antenna handbook.* John Wiley & Sons, 2011.

[135] "SteppIR 2-element Yagi Antenna Specifications." `http://www.steppir.com/wp-content/uploads/2011/11/2E-Drwg-Large1.jpg`, 2011. [Online; Accessed: 06/02/2017].

[136] "JK402 Antenna Specifications." `https://jkantennas.com/jk402.html`, 2015. [Online; Accessed: 06/02/2017].

[137] H. G. Schantz, "The flow of electromagnetic energy in the decay of an electric dipole," *American Journal of Physics*, vol. 63, no. 6, pp. 513–520, 1995.

[138] H. G. Schantz, "Electromagnetic energy around hertzian dipoles," *IEEE antennas and propagation magazine*, vol. 43, no. 2, pp. 50–62, 2001.